Author:
Gordon-Moys, Harry

Title:
Photoconductivity in Strontium Titanate

Photoconductivity in Strontium Titanate

Harry Gordon-Moys

University of Bristol
September 2018

A thesis submitted to the University of Bristol in accordance with the requirements for award of the degree of Doctor of Philosophy in the Faculty of Science,
School of Physics.

39,255 Words

Abstract

This thesis presents low temperature measurements of photoconductivity in strontium titanate. Results for nominally stoichiometric strontium titanate offer further evidence of a large increase in photocarrier lifetime below ≈ 35 K. Linear photoconductivity is observed suggesting monomolecular recombination is dominant. At still lower temperatures of < 1 K persistent photoconductivity is found to emerge. The non-equilibrium photoconductivity of thin films of oxygen deficient strontium titanate, fabricated by argon irradiation, shows not only persistent photoconductivity, as previously observed in bulk samples but also transient negative photoconductivity. Furthermore large doses of UV exposure are found to induced persistent photoconductivity in stoichiometric strontium titanate. The photocarrier lifetime can be dramatically enhanced by prolonged UV exposure, leading to photoconductivity which persisted on the timescale of hours. Finally results are presented for optically tunable superconducting-semiconducting devices, with the aim of creating Josephson junctions. Although no devices become fully superconducting a potential future route to realising optically tunable Josephson junctions is discussed.

Acknowledgements

Firstly thanks go to my supervisor, Christopher Bell, for his support, encouragement, and incredible patience over the course of this PhD. I would also like to thank Sven Friedemann, Antony Carrington, Ashraf Alam, Stephen Hayden, and Krishna Coimbatore Balram for useful advice and discussions. Special thanks must also go to Carsten Putzke for a seeming endless knowledge of low temperature physics and willingness to help. I would also like to thank all of the technical staff who have contributed to this work. In particular Bob Wiltshire, Simon Toms, and James Kelly, both for there help in building much of the equipment and suppling the liquid helium used in this work, as well as Andrew Murray for his assistance with the work performed in the cleanroom. Outside of Bristol I would like to acknowledge the contribution of Angelo Di Bernardo and Jason Robinson from the department of Materials Science and Metallurgy, University of Cambridge, who grew the majority of the superconducting films used in this work.

My time in the Correlated Electron Systems group has been made all the more enjoyable by the other members, past and present. In particular special thanks must go to Matt Bird for help me with every aspect of my PhD, as well as being a wonderful friend. A special mention should also be made to my fellow CES climbers Alice Tirbooman, Sara Karbassi, Emma Gilroy, and Maud Barthélemy for making my time both in and out of work more enjoyable. Also to Dan Chaney for an endless supply of ideas and enthusiasm, which made several long nighs and weekends in the lab much more enjoyable. Finally to Tom Croft, Joe Wilcox, Richard Waite, Jake Ayres, Tom Millichamp, Lauren Cane, Mara Bruma, Owen Moulding, and Paolo Abrami, it has been a pleasure to work alongside you and I would like to thank you all.

Lastly would like to thank my family for there support and encouragement over the last four years. Most importantly to Lauren, without your support, encouragement, and patience I wouldn't have been able to do this, thank you.

Authors's declaration

I declare that the work in this thesis was carried out in accordance with the requirements of the University's Regulations and Code of Practice for Research Degree Programmes and that it has not been submitted for any other academic award. Except where indicated by specific reference in the text, the work is the candidate's own work. Work done in collaboration with, or with the assistance of, others, is indicated as such. Any views expressed in the thesis are those of the author.

SIGNED: ..... DATE:.....

Contents

Chapter 1

Introduction

Strontium titanate, $SrTiO_3$ (STO) is a semiconductor with a wide 3.2 eV gap separating the oxygen 2p valence band from the titanium t_{2g} conduction band [1, 2]. The valence band maximum is located at Γ and, whilst the conduction band minimum has been report to be either at Γ [3] or X [4], the smallest gap is most often considered indirect [5]. At room temperature the crystal structure is cubic, undergoing a phase transition to tetragonal when cooled below 105 K [6–8]. A metallic state can be created by substituting La^{3+} for Sr^{2+} or Nb^{5+} for Ti^{4+}, or by the addition of oxygen vacancies and at a carrier density as low as 5×10^{17} cm^{-3} superconductivity emerges [9, 10], the second lowest carrier density of any superconductor, surpassed only by single crystal bismuth [11]. The first example of a superconducting semiconductor to be identified [12, 13], the critical temperature of STO has a dome like evolution in doping [14, 15] with a maximum critical temperature of $T_c \sim 300$ mK. The low carrier density region of the dome has attracted significant attention due to the fact that typical phonon energies are larger than the Fermi energy $\frac{\hbar\omega}{E_F} > 1$ and consequently cannot be described by conventional BCS theory [16, 17]. At low densities pairing without superconductivity has been predicted to occur [18], and possibly experimentally verified [19], with superconductivity only emerging when these pairs undergo Bose-Einstein condensation. This places STO alongside other unconventional superconductors such as FeSe [20] which may host a BCS-BEC crossover.

Amongst STOs many remarkable properties is the extraordinarily large photoconductivity observed when illuminated with ultraviolet (UV) light. At low temperatures the carrier density has previously been shown to increase by more than a factor of 10^{10} [21] under UV illumination. Photogenerated electrons have high mobilities $\sim 10^4$ $cm^2V^{-1}s^{-1}$ [22,23], on par with the largest observed in chemically doped samples [24]. Holes on the other hand are found to be localised [25]. Consequently UV light can be used to add electrons directly into the conduction band, effectively allowing continuous, real-time and reversible tuning of the carrier density. Furthermore the absorption of UV light is strongly dependent on the wavelength, higher energy photons being absorbed closer to the surface. The wavelength of incident light can therefore be used to tune the depth into the sample that photocarriers are generated. Photoconductivity can, therefore, be used as a tool to control both the density and thickness of a sheet of induced electrons, making it an attractive alternative to chemical doping. However despite these extraordinary properties, as yet, only a small number of works on the photoconductivity of STO have been reported.

The primary aim of this thesis is to further the understanding of photoconductivity in STO, both in terms of its fundamental properties and its use as a tool for creating highly

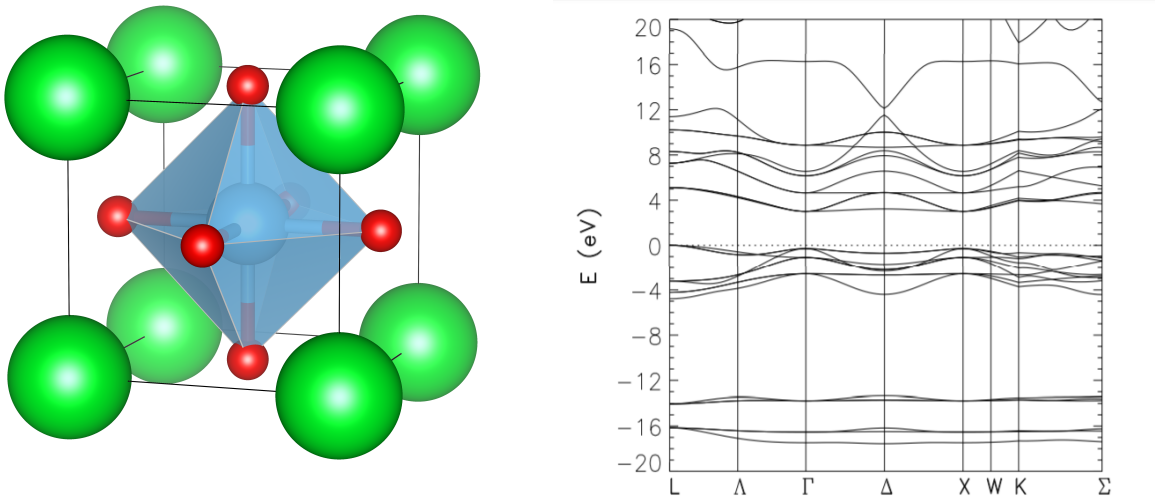

Figure 1.1: (left) A representation of the ideal cubic perovskite structure. The Sr, Ti and O ions are coloured green, blue and red respectively. (right) A recent calculated band structure of strontium titanate, by Ekuma *et al.* [26].

tunable devices. Specifically measurements of photoconductivity in stoichiometric STO, $SrTiO_{3-\delta}$, UV irradiated STO, and niobium/STO superconducting devices are presented in this thesis.

Firstly in chapter 4 results of a systematic study of the equilibrium and transient photoconductivity of stoichiometric $SrTiO_3$ and $SrTiO_{3-\delta}$ are presented. Measurements of the photoconductivity of nominally stoichiometric STO between 4 and 55 K offer further evidence that hole trapping is responsible for the large photoconductivity observed in STO. When cooled still further, to < 1 K the onset of long lived persistent photoconductivity is also found to occur. Measurements of thin films of $SrTiO_{3-\delta}$ produced by Ar^+ irradiation, also show persistent photoconductivity, consistent with previous measurements. Alongside this transient negative photoconductivity is also observed, the possible origin of this effect is discussed.

In chapter 5 results are presented for persistent photoconductivity in STO samples following surface modification by high doses of UV light. Motivated by previous work indicating that oxygen vacancies can be created by exposure to high intensity UV light, samples of stoichiometric STO were exposed to large doses of UV radiation. This was found to dramatically increase the photocarrier lifetime, leading to photoconductivity which persists on the timescale of hours. A systematic study of this photoinduced state is presented,

and its possible origins discussed.

Finally in chapter 6 the use of photoconductivity as a tool for tuning semiconducting/superconducting devices is explored, in an attempt to create optically tunable Josephson junctions. Results for several types of STO based junctions are presented. Although the ultimate aim of creating optically tunable Josephson junctions was not realised, a potential future route to achieving this is proposed.

Chapter 2

Theoretical background

In this chapter the theoretical background of the experimental work presented in this thesis is outlined. In the first section photoconductivity will be discussed. Firstly the basic theory of photoconductivity of semiconductors will be presented, then the effect of impurities will be outlined, before finally addressing non-equilibrium photoconductivity. The second section covers superconductivity and the Josephson effect. Firstly outlining the basic properties of the superconducting state and two of the most ubiquitous theories Ginzburg-Landau and BCS. Finally the superconductor normal metal interface and the Josephson effect will be discussed.

2.1 Photoconductivity

2.1.1 Semiconductors and photoconductivity

Photoconductivity is the change in electrical conductivity of a material caused by the absorption of light. This typically, but not always, leads to an increase in the conductivity. Since its discovery in the late 19^{th} century [27] photoconductivity has been observed in a myriad of semiconductors and heterostructures, and can vary in magnitude from changes of a few percent to increases in conductivity by more than a factor of 10^{10} [28, 29].

The measured change in conductivity can have two main origins. Firstly electrons and holes can be optically excited into the conduction and valence bands, leading to an increase density of free carriers. Secondly carriers which are already free can be excited to an unoccupied state within the same band, where the mobility is different [30]. Accounting for both of these effects the change in conductivity can be expressed as

$$\Delta\sigma = q\mu_0\Delta n + q\Delta\mu(n_0 + \Delta n), \tag{2.1}$$

where $\Delta\mu$ and Δn are the increase in mobility and carrier density under illumination and μ_0 and n_0 are the dark mobility and carrier density [31]. Typically the change in carrier density is the dominate effect, particularly in the case of wide bandgap semiconductors where there is not a significant density of thermally excited carriers ($\Delta n \gg n_0$).

The change in carrier density induced by light Δn is determined by the rate at which carriers are generated G and the average time before recombination occurs τ, known as the lifetime. In equilibrium, when the rate of generation and recombination are balanced, the density of photoinduced carriers can be describe by

$$\Delta n = G\tau. \tag{2.2}$$

An additional complexity to equation 2.2, however, is that lifetime τ can also be dependent of the generation rate, G. Setting $\tau \propto G^{\gamma-1}$, three situations can be described. When the lifetime is independent of the generation rate $\gamma = 1$ (known as linear photoconductivity), when the lifetime decreases as the generation rate increases $\gamma < 1$ (sublinear photoconductivity), and finally when the lifetime increases as the generation rate increases $\gamma > 1$ (supra-linear photoconductivity) [32]. The physical mechanisms which cause each of these to arise will be discussed in section 2.1.3.

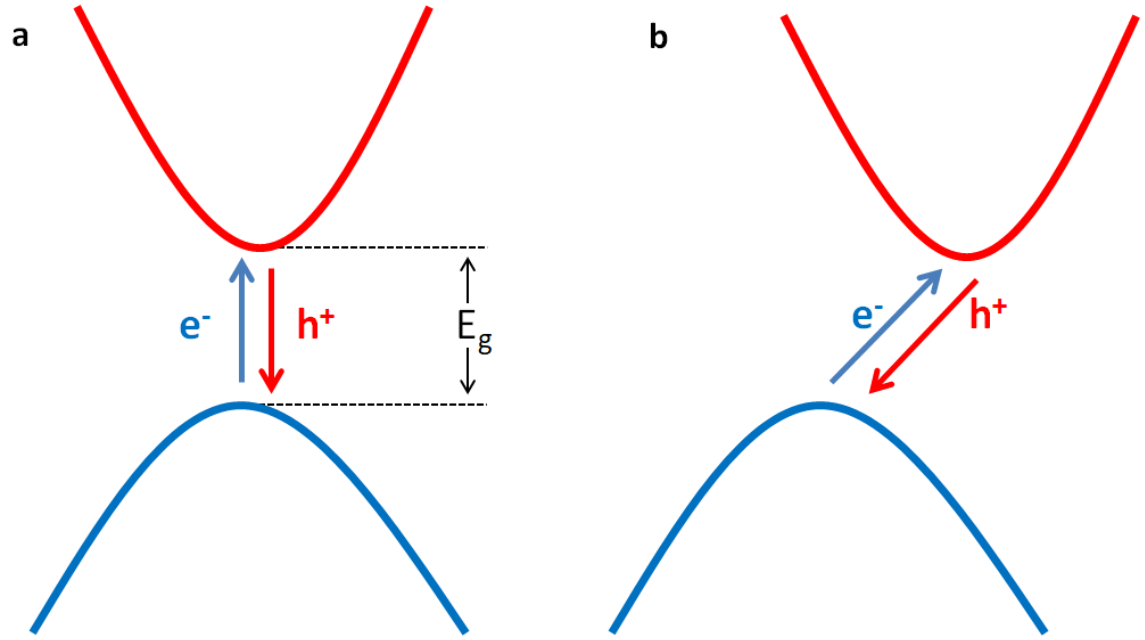

Figure 2.1: Intrinsic optical absorption for (**a**) a direct bandgap semiconductor and (**b**) an indirect bandgap semiconductor, with a gap size of E_g. Electrons (blue arrow) are promoted from the valence band (blue line) to the conduction band (red line).

The absorption of light by a semiconductor can be quantified by a coefficient of absorption α. Using this the intensity of transmitted light as a function of depth, z, into a semiconductor can be described by Beer's law,

$$I = I_0 \exp(-\alpha z), \tag{2.3}$$

where I_0 is the initial incident intensity. Therefore at a depth $z = \alpha^{-1}$ into the semiconductor $1/e$ photons will have been absorbed. This distance can be defined as the optical penetration depth $d = \alpha^{-1}$. In the simple case of a defectless semiconductor absorption is intrinsic, an electron from the valence band is promoted into the conduction band. The light must have an energy of at least that of the bandgap E_g to be absorbed, consequently the material is transparent to photons where $\hbar\omega < E_g$.

Optical absorption can be either direct (no exchange in momentum) or indirect (change in the wavevector k), dependent on the band structure of the semiconductor in question. Direct transition involve only a photon, whereas indirect transitions also require the

simultaneous exchange (either absorption or emission) of a phonon, as the momentum of a photon is effectively negligible. These two types of absorption are shown in figure 2.1. In the case of direct transitions the coefficient of absorption varies as

$$\alpha = \sqrt{E_{photon} - E_g}, \tag{2.4}$$

consequently as the incident photon energy E_{photon} is increased the absorption occurs in a progressively thinner sheet near to the surface (see ref. [32] for a full derivation). This allows the wavelength of incident light to be used to tune the depth of photocarrier generation, the penetration depth varying as $d = (E_{photon} - E_g)^{-\frac{1}{2}}$.

Equations 2.2 and 2.4 form the fundamental basis for tuneability in a photoconductor. Firstly the carrier density can be controlled by the intensity of illumination. Secondly the depth of photoinduced carriers can be controlled by the wavelength of illumination.

2.1.2 Recombination and the effect of in-gap states

The addition of defects or impurities into a semiconductor can create localised electronic states within the band-gap which introduce a myriad of new phenomena associated with photoconductivity, such as persistent and negative photoconductivity. These in-gap levels allow for a greater range of optical and thermal transitions, making both intrinsic and extrinsic absorption possible and broadening the spectral response to photon energies lower than the band-gap. Similarly in-gap states also change the possible transitions mediating recombination. Consequently the addition of in-gap states can lead to both significantly shorter or longer photocarrier lifetimes, which dramatically alters both the equilibrium and non-equilibrium photoconductivity.

2.1.2.1 Traps and recombination centers

The addition of in-gap states introduces new optical transitions, shown schematically in figures 2.2 and 2.3. Carriers can be excited into the conduction band directly from the valence band or via an in-gap level. Excited carrier can also be captured by in-gap states. In general the rate of capture R of free carriers with density n by a species of density N can be expressed as

$$R_c = \beta n N, \tag{2.5}$$

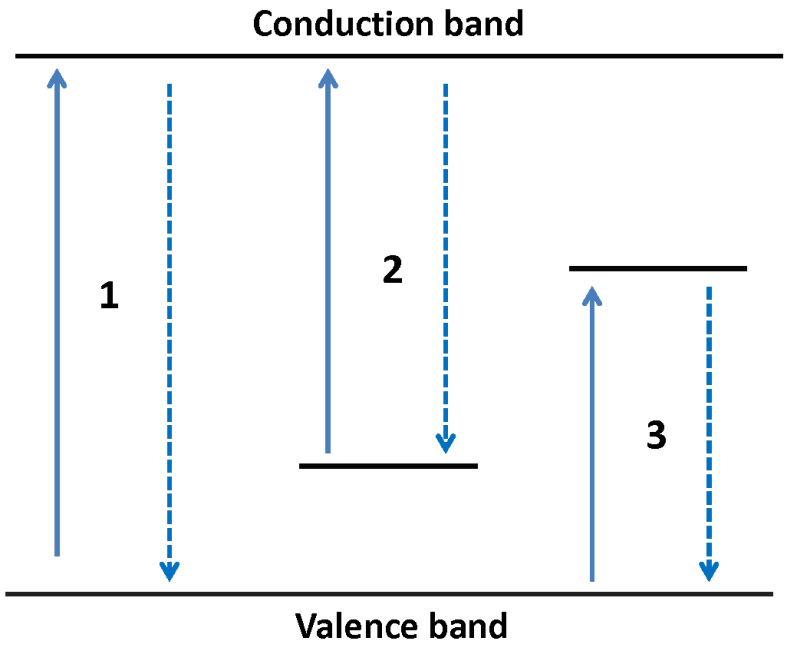

Figure 2.2: Possible electronic transitions when imperfections are present; optical absorption/excitations (solid) and recombination (dashed). (1) intrinsic absorption and recombination from the valance band to the conduction band or vice-versa, (2) and (3) extrinsic absorption and recombination from an imperfection to the conduction band and valance band to an unoccupied imperfection respectively.

where β is the capture coefficient and can be expressed as the product of the capture cross section S and the average thermal velocity v of the free carrier

$$\beta = Sv. \tag{2.6}$$

If the capture leads to recombination then in equilibrium the rate of capture is equal to the generation rate, $R_c = G = n/\tau$. Therefore the capture coefficient and density of capture centers can be used to calculate the average time a carrier is free before capture,

$$\tau = 1/\beta N. \tag{2.7}$$

Once a carrier is captured by an in-gap state there are two possible processes which can subsequently occur;

1. The captured carrier can undergo recombination with a carrier of the opposite type via the in-gap state.

2. The captured carrier can be thermally reexcited back into the conduction band, after which it can *then* undergo recombination, or retrapping.

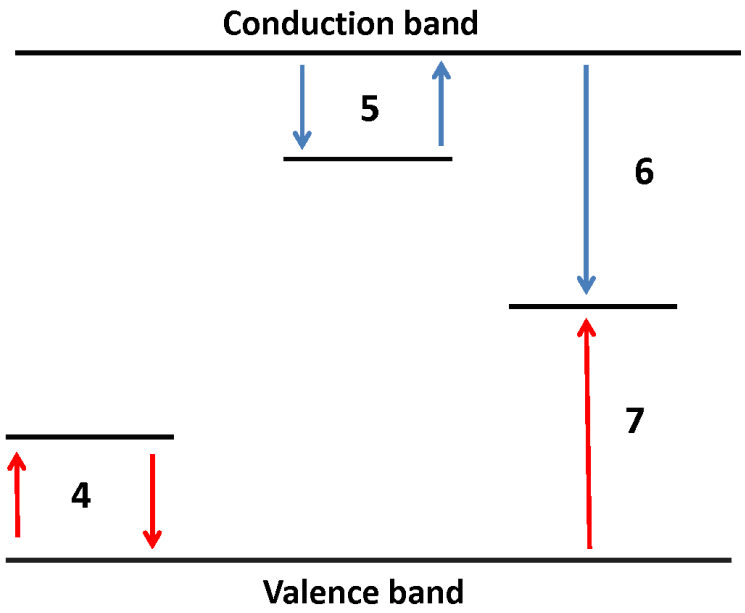

Figure 2.3: Possible electronic transitions when imperfections are present; (4) and (5) capture and thermal reexcitation of holes and electrons respectively in trap states, (6) and (7) capture of electrons and holes respectively at a recombination center.

When the second process dominates the in-gap states are referred to as traps. These trapping centers capture and release carriers temporarily localising them, but don't directly mediate recombination. Whereas when the first is dominant the states are known as recombination centers. This can quantified as follows; the rate of capture of free carriers by the in-gap state is $R_c = \beta_c n N$, and a rate of thermally activated detrapping can be expressed as,

$$R_d = n_t \nu \exp(-E_a/k_b T) \tag{2.8}$$

where n_t is the density of trapped carriers, ν is the attempt to escape frequency, and ΔE is the activation energy of detrapping. If $R_c > R_d$ then the state acts as a recombination center, and if $R_c < R_d$ then it acts as a trap.

Typically the cross section is higher for recombination centers that for direct band to band recombination. Consequently recombination centers are often the dominant channel through which electrons and holes recombine.

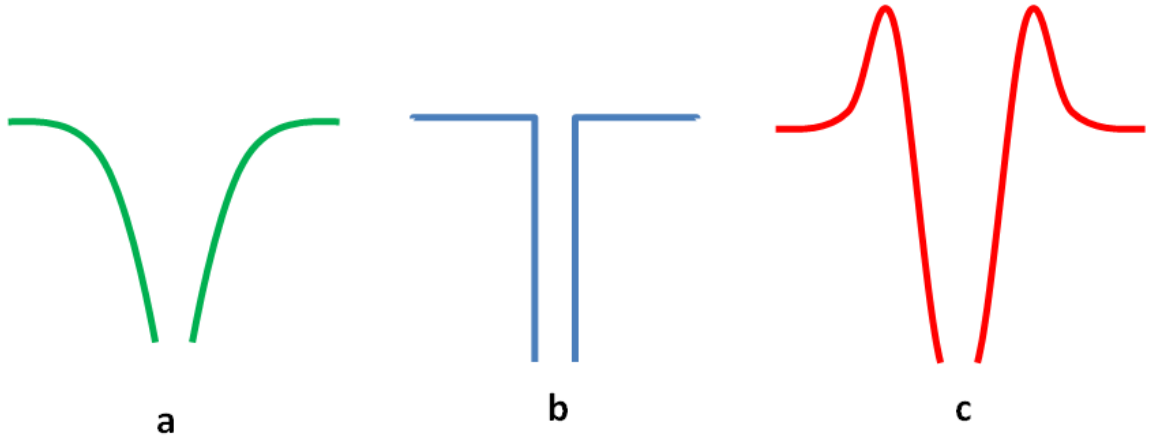

Figure 2.4: A schematic of the three possible potentials of a defect (**a**) an attractive imperfection, (**b**) a neutral imperfection, and (**c**) a repulsive imperfection. Adapted from Bube [31]

2.1.2.2 Charged defects

A key factor which determines the capture cross section β, and therefore the lifetime of carriers, is the charge of a defect. Schematics of the three possible potentials of a defect, attractive, neutral, and repulsive are shown in figure 2.4.

The capture cross section of an attractive defect can be estimated by assuming there is a capture radius r_c around an defect for which the probability of capture is 1 when $r < r_c$ and 0 when $r > r_c$ for a free carrier of distance r away from the defect. r_c can be defined as the distance at which the coulomb potential is equal to the average thermal energy k_bT, this can be expressed as

$$r_c = \frac{q^2}{4\pi\epsilon_r\epsilon_0 k_b T}. \tag{2.9}$$

The capture cross section is therefore equal to

$$S = \pi r_c^2 = \frac{q^4}{16\pi\epsilon_r^2\epsilon_0^2 k_b^2 T^2}. \tag{2.10}$$

A slightly more complex approach is to define r_c as the point the probability of an electron drifting into the center is equal to the probability of an electron diffusing away, i.e. when $v_{drift} = v_{thermal}$, however this only changes the result of 2.10 by a factor of $\frac{9}{16}$ [32].

For the opposite case of a coulomb repulsive defect there is an energy barrier ΔE which must be overcome before a carrier can be captured, the thermally activated cross section can be expressed as

$$S \propto exp(-\Delta E/k_b T), \tag{2.11}$$

2.1.2.3 Types of lifetime

In the absence of any in-gap states a single lifetime τ can be unambiguously defined. This describes the characteristic time between generation and recombination of an electron hole pair. If there are no in-gap states electrons and holes can only exist in either the conduction or valence band and are therefore delocalised and contribute to conductivity, until recombination takes place.

However once in-gap states are introduced electrons and holes can be independently captured and consequently localised, without recombining. Two lifetimes can be defined to describe these processes. Firstly the amount of time electrons or holes are in the conduction or valance band, before being localised either by recombination or capture by an in-gap state, known as the *free carrier lifetime*. Secondly the total time between generation and recombination including the time carriers spend localised in in-gap states the *excited lifetime*.

The free carrier lifetime of electrons and holes need not be equal, as the probability of capture at an in-gap state can be different for electrons and holes. For example positively charged in-gap states have a higher rate of capture for electrons. Consequently the free carrier lifetime can be further divided into the individual free lifetimes of electrons and holes. For generality these are typically referred to as the majority and minority carrier lifetimes. Small minority carrier lifetimes can in fact dramatically *increase* the majority carrier lifetime, by reducing the density of free minority carrier to recombine with majority carriers.

When measuring equilibrium photoconductivity it is the free lifetime of the majority carrier that is measured.

2.1.3 Models of recombination

To predict the behaviour of photoconductors models of recombination with different in-gap states can be constructed. In this section three commonly used models will be outlined. Firstly a model of a semiconductor with no recombination centers, secondly with one recombination center and thirdly a model with two types of recombination center. The last of these is particularly relevant to experimental results presented in this thesis.

2.1.3.1 No recombination centers

Firstly the simplest model of recombination, where no in-gap states are present, is considered. In this system two transitions are possible, electrons can be optically excited into the conduction band, and recombine with a hole in the valence band. It is assumed that no thermally excited carriers are present. Combining equations 2.2 and 2.7 the density of photogenerated carriers can be expressed as

$$G = n\beta p. \tag{2.12}$$

Since electrons and holes can only exist in either the valence or conduction band $p = n$, therefore

$$G = n\beta p \propto n^2, \tag{2.13}$$

this is often referred to as *bimolecular* recombination. Since $n = G\tau$ this physically corresponds to the average lifetime decreasing as the generation rate increases, $\tau \propto 1/\sqrt{G}$ ($\gamma = 0.5$) a case of sublinear photoconductivity.

2.1.3.2 One center recombination

The next most complex model is to consider one recombination center, which is the dominant recombination process. This leaves three possible transitions, optical generation of electron hole pairs, capture of electrons at a recombination center and capture of holes at a recombination center. The density of free electrons, free holes, and electron occupied recombination centers can be expressed by three rate equations

$$dn/dt = G - n\beta_n(N_{rc} - n_{rc}), \tag{2.14}$$

$$dn_{rc}/dt = n\beta_n(N_{rc} - n_{rc}) - n_{rc}p\beta_p, \tag{2.15}$$

$$dp/dt = G - n_{rc}p\beta_p. \tag{2.16}$$

Where β_n and β_p are the capture coefficient of electrons and holes at the recombination center, N_{rc} is the total density of recombination centers and n_{rc} is the density of electron occupied recombination centers. Using these equations and the additional condition that the number of free electrons is equal to the number of free holes and the number of hole occupied recombination centers. $n = p + (N_{rc} - n_{rc})$, the number of free electrons as a function of the generation rate can be expressed as

$$G = (N_{rc} - G/n\beta_n)(n - G/n\beta_n)\beta_p. \tag{2.17}$$

For a full derivation see Bube chapter 3 [32]. Assuming the capture of holes is favored $\beta_n < \beta_p$, and that there is a sufficiently high excitation rate, then most recombination centers are hole occupied, $(N_{rc} - n_{rc} \approx N_{rc})$. In this case the rate of recombination is determined entirely by the rate of electron capture and equation 2.17 reduces to $G \propto n$ producing linear photoconductivity in generation rate ($\gamma = 1$). This is typically known as *monomolecular* recombination and corresponds physically to a lifetime τ that is independent of the density of free carriers.

2.1.3.3 Two center recombination

A more complex model of recombination is one that considers two different types of recombination centers. One with a similar rate of capture for electrons and holes $\beta_p \approx \beta_n$, which will act as an efficient channel for recombination. The second, however, having a much larger rate of capture for one type of carrier for example $\beta_n \ll \beta_p$. This this often known as a sensitizing level. This difference in cross section can be achieved by the sensitizing level being doubly negatively charged, making it attractive for holes and repulsive for electrons, even after a hole has been captured. Sensitizing levels may behave either as recombination centers or like traps dependent on the temperature.

A wide range of behaviours can be predicted within this model. For example if the sensitizing level has a larger capture rate for the minority carrier this can lead to so called imperfection sensitization, where an imperfection captures the minority carrier

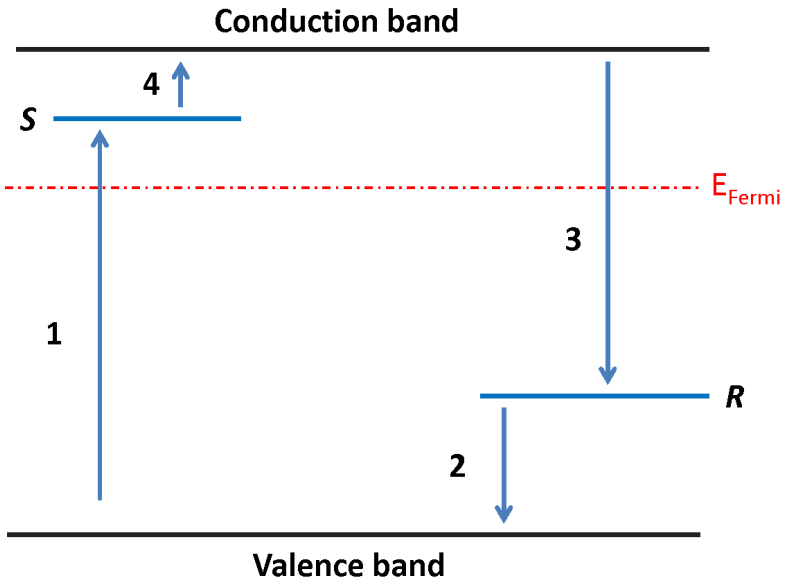

Figure 2.5: A possible mechanism of negative photoconductivity using a two center model with a sensitizing level (S) above the Fermi level (dashed red line) and a recombination level (R) below. The movement of electrons is represented by a blue arrow. 1) an electron is excited into the unoccupied sensitizing level, 2) the corresponding hole is captured by the recombination center, 3) a free electron from the conduction band is captured by the recombination center, 4) the electron in the sensitizing level is thermally excited back into the conduction band.

thereby suppressing recombination and increasing the majority carrier lifetime, resulting in a larger photoconductivity [33]. Another behaviour which can be explained with a two center model is negative photoconductivity, a *reduction* in conductivity when illuminated.

Negative photoconductivity has been observed in several materials, such as GaAs [34–36], Ge nanocrystals in Al_2O_3 [37], and graphene [38], although it is relatively uncommon. It may seam that a reduction in conductivity could only originate from a suppression of the mobility, however using a two center model it is possible to explain this by a reduction in the free carrier density.

A photoinduced reduction in the carrier density can be described by a two center recombination model, with an unoccupied sensitizing level and an occupied recombination center, this is shown schematically in figure 2.5. When illuminated, an electron can be optically excited into the sensitizing level, leaving a hole behind in the valence band (transition 1). The hole can then be captured by an efficient recombination center (transition 2) and subsequently recombine with an electron captured from the conduction band

(transition 3). Finally the electron trapped in the sensitizing level can be thermally excited into the conduction band restoring the dark state (transition 4). A reduction in carrier density occurs provided that the rate of thermal excitation of an electron from the sensitizing level to the conduction band is smaller than the rate of capture of electrons by the recombination center, i.e the rate of transition 4 is slower than transition 3. A further condition is that the rate of hole capture is larger for the recombination center than the sensitizing level $\beta_{p,S} < \beta_{p,R}$, so that the sensitizing level remains occupied with an electron until it is thermal excited into the conduction band.

2.1.4 Non-equilibrium photoconductivity

The models of recombination described in section 2.1.3 assume an equilibrium between generation and recombination has been reached, however this is often not the case, particularly if traps are present. There are two additional processes involved when traps are introduced, filling the traps during the build up of photoconductivity and emptying the traps during decay, both of which increase the time for equilibrium to be reached.

When minority carrier traps are present a slower build-up and decay of photoconductivity will be observed, as these traps are filled and the photosensitivity increases. When illumination has ceased these carriers must be detrapped before undergoing recombination. If the activation energy of this process is small compared with the temperature the rate of detrapping is low, this can lead to photoconductivity hours or even days [**?**] after the light is switched off. When the lifetime of the majority carrier has been extended to these timescale it is often known as persistent photoconductivity.

2.1.4.1 Persistent photoconductivity

Persistent photoconductivity is observed in a wide range of semiconductors, such as GaAs [39], MoS_2 [40], $KTaO_3$ [41], and ZnO [42], particularly when a large density of defect are present. Persistent photoconductivity occurs when the recombination of photogenerated electrons and holes is suppressed, typically this can be explained in terms of two processes. Firstly, as described above, the minority carrier can become trapped by an in-gap state, required thermal excitation out of the trap before recombination to occur. Secondly electron and holes can become spatially separated by an electric field within a material, since they can only recombine in regions which they overlap both the majority and minority carrier lifetimes can be increased. Charge separation if often the cause of

persistent photoconductivity at interfaces and heterostructures [43–48]. However these two origins are not necessary mutually exclusive, in some case both charge separation and trapping are involved [49].

The simplest model of the decay of photoconductivity is one of single exponential decay

$$n(t) = n_0 \exp(-t/\tau_0), \tag{2.18}$$

where n_0 is the initial free carrier density and τ_0 is the time constant which is assumed not to be a function of time itself. The lifetime can be related to the rate of detrapping of holes from a single trap state as follows

$$1/\tau_0 = N_v \beta_p exp(-\Delta E/k_b T), \tag{2.19}$$

where N_v is the density of states in the valence band, β_p the capture coefficient of the trap for holes, and ΔE is the depth of the trap with respect to the valence band. An Arrhenius plot of $\ln(\tau_0)$ vs $1/T$, has a gradient of $\Delta E/k_b$ allowing the depth of the trap to be determined.

The simple model of exponential decay is, however, rarely applicable in practice and the decay is typically more complex. This could be due to strong re-trapping of carriers, i.e. re-trapping at a comparable rate to recombination or to multiple trap levels with different capture coefficient and rates of de-trapping. The most commonly used function to describe these more complex decays of photoconductivity, is a stretched exponential.

2.1.4.2 Stretched exponential decay

The stretched exponential function can be expressed as

$$n(t) = n_0 \exp\left(\left(-\frac{t}{\tau}\right)^{\beta}\right) \tag{2.20}$$

Where $n(t)$ is the number of free electrons at time t and n_0 is the number of free electrons at the point illumination is ceased. For consistency with the literature β will be used to denote the stretching parameter in this thesis. This is not, however, the same as the capture coefficient which is also commonly called β, to avoid confusion the capture coefficient will always carry a subscript to denote the type or level of capture.

There are generally two interpretations of when stretching of an exponential decay would

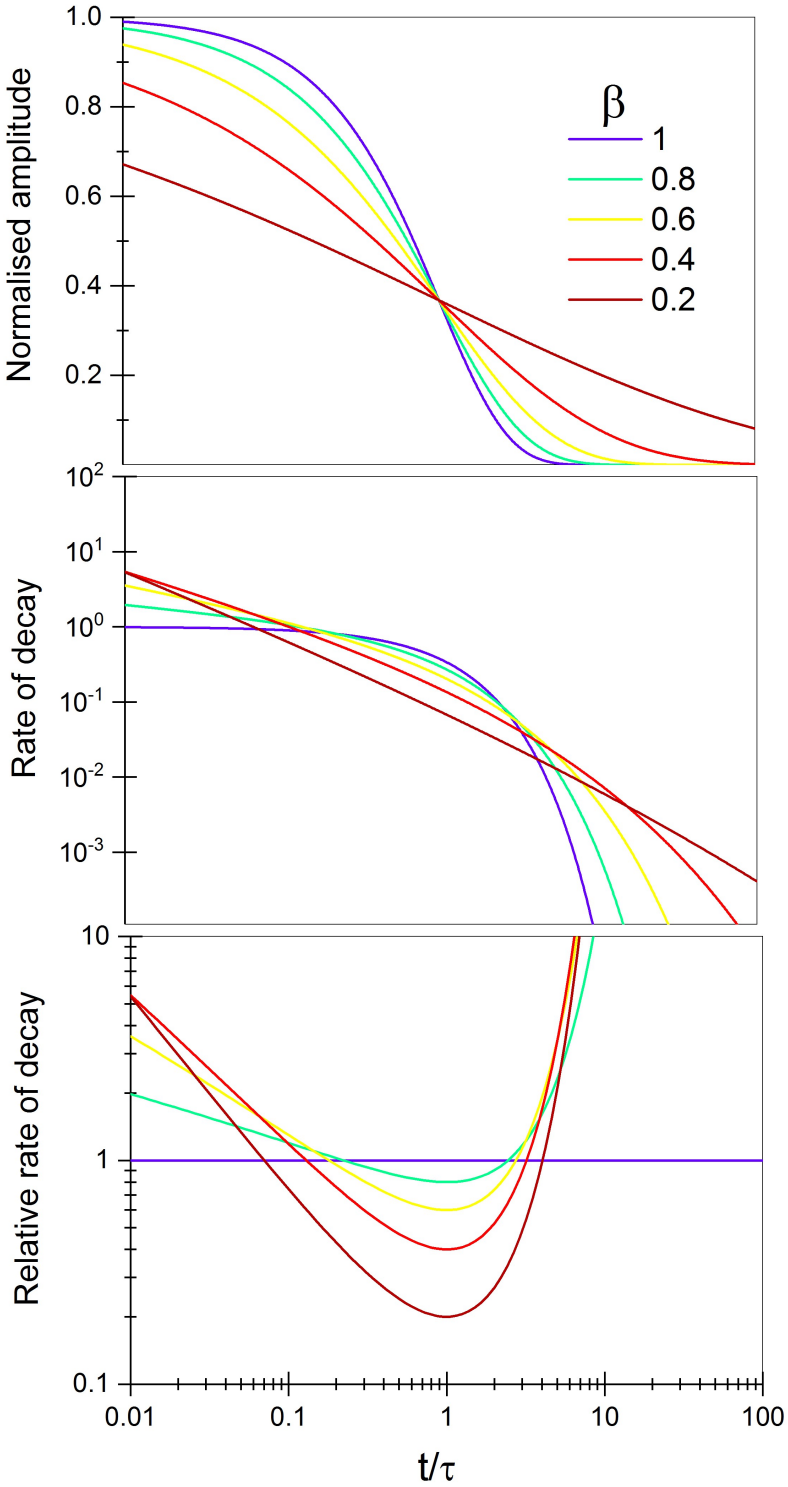

Figure 2.6: Stretched exponential decay for varying stretching parameter $\beta = 1$ to 0.2 (top), rate of decay (middle) and the rate relative to single exponential decay (bottom).

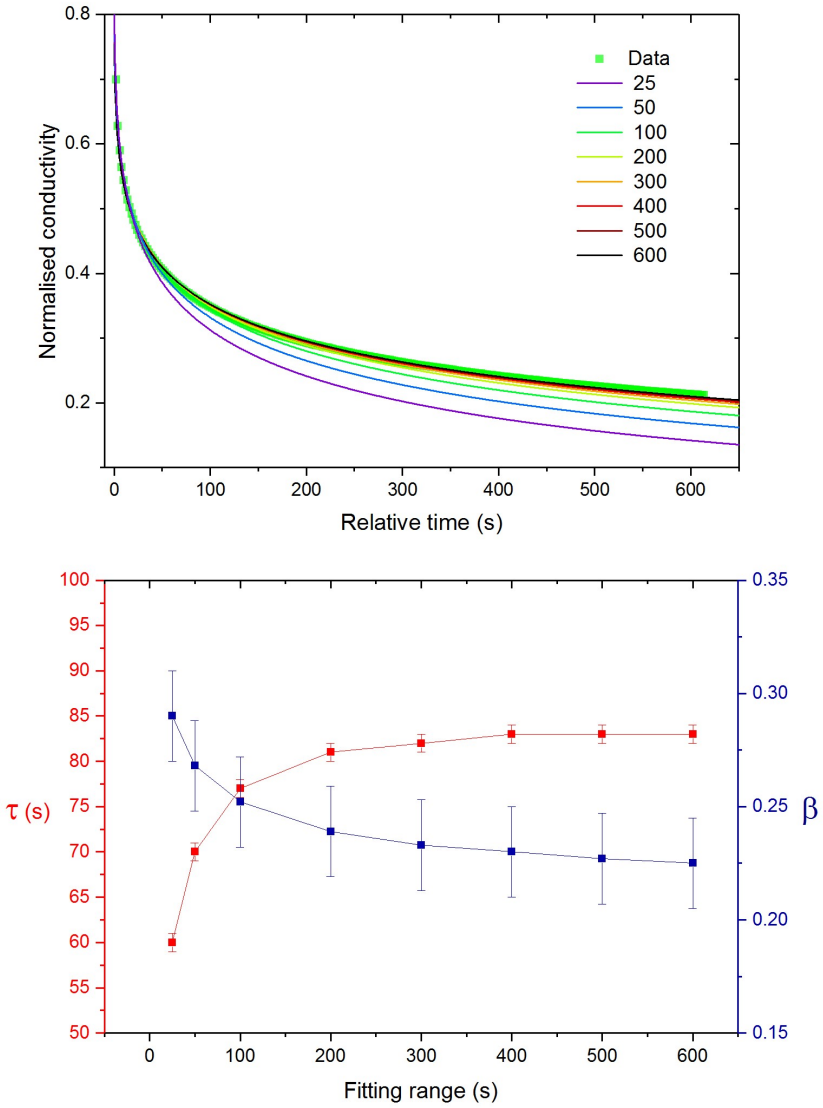

Figure 2.7: An example of stretched exponential fits over time ranges varying from 25 to 600 seconds (top) and the extracted fitting parameters (bottom).

arise, a serial process of sequential relaxations [50] or a parallel process of multiple decays [51]. Another interpretation of this is a time dependent lifetime, defined as

$$\tau_0(t) = \tau^{\beta} \cdot t^{1-\beta}, \tag{2.21}$$

Examples of a stretched exponential function for five stretching parameters $\beta = 0.2$, 0.4, 0.6, 0.8, and 1 (a normal exponential) are shown in figure 2.6, as well as the absolute rate of decay and that with respect to a normal exponential decay. The stretched exponential is characterized by an initially fast decay followed by a long tail of slower decay, the smaller the value of the stretching parameter the more exaggerated this effect becomes.

Stretched exponential decays are found to make good fits to the data for persistent photoconductivity presented in this thesis, examples of fitting are shown in each of the relevant sections. However one common theme found in this work, is that the fitting parameters are dependent on the range over which the function is fitted. An example of data describing the decay in normalised conductivity from chapter 5 is shown in figure 2.7, with fit ranges from 25 seconds to 10 minutes. Short fit ranges consistently over predict the rate decay resulting in smaller values of τ and larger values of β, however after 300 second of fitting these parameters do not change significantly.

2.1.4.3 Logarithmic decay and the charge separation model

Whilst the decay of photocarriers is most often fitted by a stretched exponential, it has been suggested that this may be neither the best fit nor have an intuitive physical interpretation, however an alternative model of logarithmic decay has been proposed by Queisser *et al.* [49, 52, 53].

This model was originally proposed for a thin (approximately 3μm) layer of n-type GaAs on a highly resistive substrate of chromium doped GaAs. When illuminated electron hole pairs are created in the top, n-type layer. The interfacial potential subsequently spatially separates the photogenerated electrons and holes. Electrons remain near to the surface in the layer where they were generated, delocalised and therefore contributing to photoconductivity. In contrast holes diffuse into the substrate where they are captured by traps and become localised. As traps in the substrate near to the n-type photoactive layer are filled by holes, subsequently photogenerated holes must travel deeper into the substrate before becoming trapped. This increase in current upon illumination is found

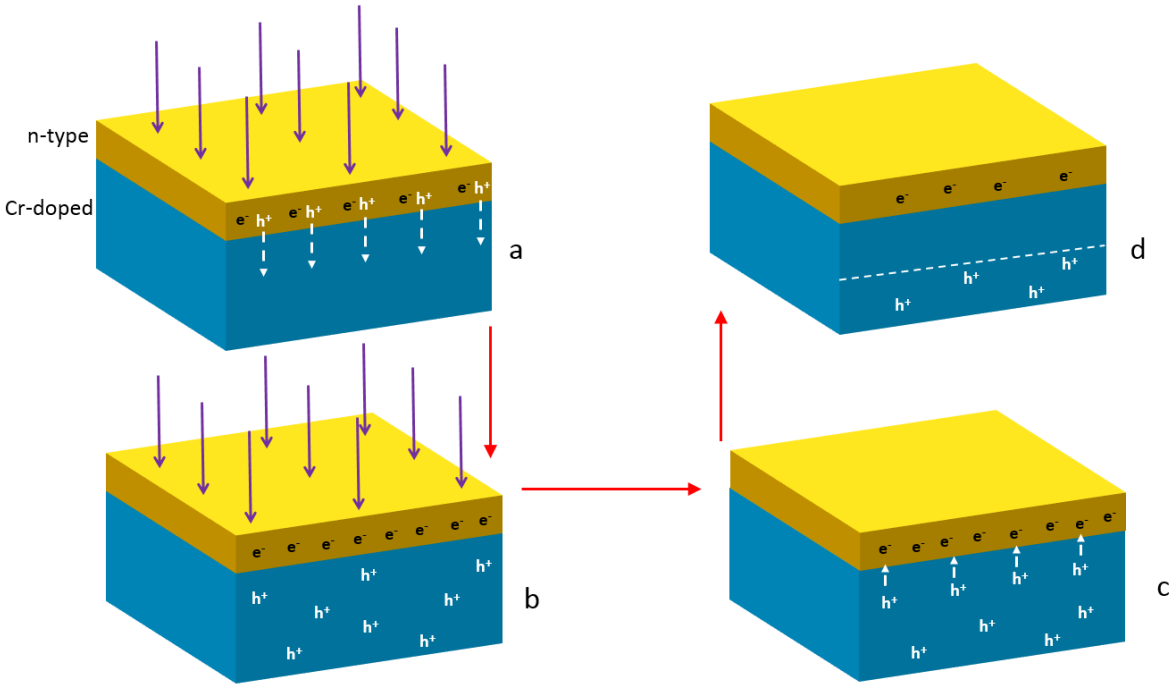

Figure 2.8: Schematic of the Queisser model for photoconductivity in GaAs.**a)** Electron hole pairs are created in the n-type layer at the surface, **b)** photogenerated hole diffuse into the bulk Cr-doped GaAs and become trapped, **c)** holes near to the surface rapidly recombine with electrons in the n-type layer, **d)** deeper (spatially) trapped holes remain in the substrate taking much longer to recombine.

to be proportion to the logarithm of the dose of photons [54].

When illumination is ceased the reverse process occurs, recombination is initially rapid as electrons and holes near to the surface recombine, however after the traps near to the surface are emptied holes have to travel further, from deeper in the substrate before they encounter an electron. This leads to an initially rapid decay of photoconductivity which becomes continuously slower as time goes on. This is shown schematically in figure 2.8.

For a rectangular distribution of trapped holes the decay of photocurrent can be described by

$$\frac{\sigma(t)}{\sigma(t=0)} \propto 1 - \alpha \ln\left(\frac{t}{\tau_0} + 1\right) \tag{2.22}$$

Where the constant α is proportion to the density of traps and the mobility of electrons. The logarithmic decay described by equation 2.22 is also found to fit the data for persistent photoconductivity in this thesis.

2.2 Superconductivity and the Josephson effect

2.2.1 Superconductivity

Superconductivity was first observed by Kamerlingh Onnes in 1911, when he measured the electrical resistance of mercury drop to $< 10^{-5}\Omega$s at 4.1 K [55], subsequently many other metals such as lead and tin were also shown to exhibit perfect conductivity when cooled below some critical temperature T_c. Once established, for example in a ring of superconductor with a flux through it, a supercurrent can persistent almost indefinitely without loss [56]. The complete absence of any D.C electrical resistance is not, however, the only feature the superconducting state. Meissner and Ochsenfeld [57] later showed that perfect conductivity was also accompanied by perfect diamangetism. They found not only that an applied magnetic field would be excluded from a superconductor, as would also be the case for a perfect conductor, but that a preexisting field would be expelled from the superconductor as it is cooled through its critical temperature. In contrast when field cooled a perfect conductor would do the opposite and trap the preexisting field. Since expelling a magnetic field requires energy this implied that there will be some critical field H_c, which exceeds the difference in free energy between the superconducting and normal states and destroys superconductivity [58].

Superconductivity occurs in around half of all metallic elements, of which niobium has the highest T_c at ≈ 9.2 K, as well as more complex materials such as the iron pnictides, and cuprate families of superconductors with T_c's as high as 130 K [59] (or 164 K under pressure [60]). The maximum value of T_c was recently increased dramatically when superconductivity was observed at temperatures as high as 203 K in hydrogen sulfide, although with the not inconsiderable caveat of being under a pressure of ≈ 200 GPa [61].

2.2.1.1 Ginzburg-Landau theory

A phenomenological theory of superconductivity was developed by Ginzburg and Landau in 1950 [62], based on Landau's earlier work on second-order phase transitions [63]. Landau's general approach to second order phase transitions had been to express the free energy of a system with respect to some order parameter, which was zero above a transition temperature and but non-zero below it, consequently breaking a symmetry of the system. For example in the case of ferromagnetism the order parameter is the magnetisation. This is zero above the Curie temperature where the spins are randomly orientated, but has a non-zero value below the Curie temperature where the rotational

symmetry of the system is spontaneously broken.

In the case of superconductivity the order parameter used by Ginzburg and Landau was a complex, position dependent wavefuction $\psi(\mathbf{r}) = |\psi(\mathbf{r})|e^{i\theta}$, where $|\psi(\mathbf{r})|^2$ represents the local density of superconducting electrons. The free energy of a superconductor can be described, assuming that there are no magnetic fields, as

$$f_s(T) = f_n(T) + \alpha(T)|\psi(\mathbf{r})|^2 + \frac{\beta(T)}{2}|\psi(\mathbf{r})|^4 + \frac{\hbar}{2m^*}|\nabla\psi(\mathbf{r})|^2. \tag{2.23}$$

Where f_s and f_n are the free energies of the superconducting and normal state respectively and, α and β are phenomenological parameters. By minimising the free energy over all space

$$-\frac{\hbar^2}{2m^*}\nabla^2\psi(\mathbf{r}) + (\alpha + \beta|\psi(\mathbf{r})|^2)\psi(\mathbf{r}) = 0, \tag{2.24}$$

is obtained, a full derivation of this result can be found in [64]. Equation 2.24 is particularly useful for determining the behaviour of $\psi(\mathbf{r})$ near to the surface of a superconductor. Considering the case of a superconductor-metal interface located at $x = 0$ with the superconductor at values of $x > 0$ and setting the boundary condition of $\psi(0) = 0$, equation 2.24 yields,

$$\psi(x) = \psi_0 \tanh[x/\sqrt{2}\xi_{GL}(T)]. \tag{2.25}$$

Where ψ_0 is the values of the order parameter in the bulk and $\xi_{GL}(T)$ is defined as

$$\xi_{GL}(T) = \sqrt{\hbar^2/2m^*|\alpha(T)|}. \tag{2.26}$$

This is known as the Ginzburg and Landau coherence length and describes the length scale over which the order parameter returns to its bulk value at an interface, defect, or some other suppression of superconductivity. Since the order parameter is defined as $\psi = |\psi|e^{i\theta}$ then in the ground state the phase of the wavefuction θ must be the same everywhere in a superconductor, and a particular phase must be chosen. This appears to break global electromagnetic gauge invariance, which is consequently often regard as the symmetry broken in the transition to superconductivity. It has recently been argued however, that it is merely the removal of the freedom for the relative phase between two (or more) superconductors to vary arbitrarily, rather than global gauge symmetry breaking. For a more detailed argument see [65, 66].

2.2.1.2 BCS theory

In 1957, shortly after the Ginzburg-Landau theory, a microscopic description of superconductivity was given by Bardeen, Cooper, and Schrieffer [67]. This followed on from work by Cooper in which he considered a pair of electrons added just outside the Fermi level [68]. He was able to show that *any* finite attraction between a pair of electrons, regardless of how weak, would cause them to form stable pairs (now known as Cooper pairs). The bare interaction between electrons will, of course, be *repulsive* rather than attractive, however if the interaction of electrons and phonons is included then an attractive potential is possible, this was suggested as a mechanism of superconductivity by Fröhlich [69, 70]. In a simplified picture of this an electron locally distorts the lattice around it, but moves away far quicker than the lattice relaxes leaving a region of excess positive charge which is attractive to a second electron. This electron-phonon coupling explained the so called isotope effect [71, 72], where it was found that the critical temperature of superconductors were typically inversely proportional to the atomic mass of the isotopes used.

BCS realized that the whole Fermi surface would be unstable to the formation of Cooper pairs and that they would form a condensate, similar to that of superfluid helium-3 (although not identical, for example see [64]). Schrieffer introduced a many particle wavefuction for the condensate, with the BCS ground state having the form

$$|\psi_{BCS}\rangle = \prod_k (u_k^* + v_k^* \hat{P}_k^\dagger)\,|0\rangle\,, \tag{2.27}$$

where $|u_k|^2 + |v_k|^2 = 1$ with $|u_k|^2$ and $|v_k|^2$ giving the probability of a state being empty or occupied respectively, and the operator $\hat{P}_k^\dagger = c_{k\uparrow}^\dagger c_{-k\downarrow}^\dagger$ creates a Cooper pair with both a crystal momentum and a net spin of zero. By minimizing the total energy $E = \langle\psi_{BCS}|\,\hat{H}\,|\psi_{BCS}\rangle$, the spectrum of excitations energies from the BCS groundstate can be expressed as

$$E_k^2 = \xi_k^2 + \Delta_k^2, \tag{2.28}$$

where $\xi_k = \epsilon_k - \mu$, ϵ_k is the energy of an electron relative to the Fermi level with momentum k and μ is the chemical potential, an example of this spectrum is shown in figure 2.9. These quasi-particle excitations, often known as *Bogoliubons*, have a superposition of electron and hole character.

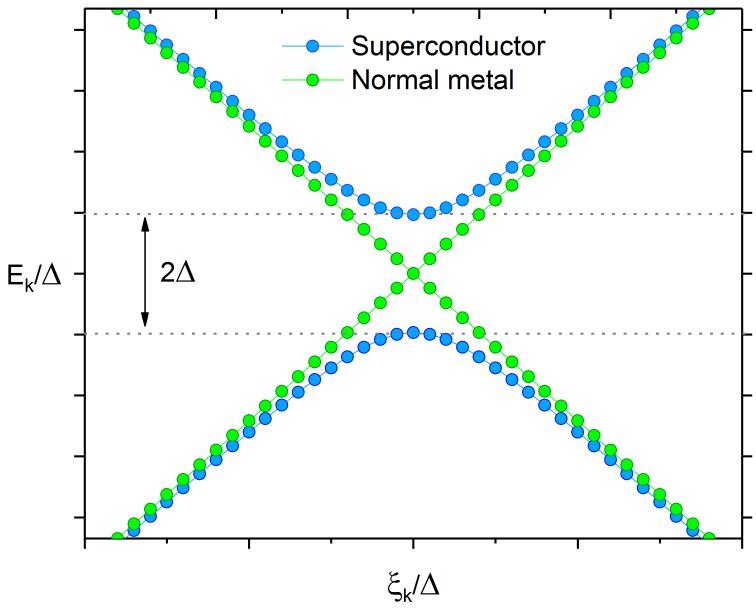

Figure 2.9: The energy spectrum of excitation in the the normal state (green) and superconducting state (blue), as described by $E_k^2 = \xi_k^2 + \Delta_k^2$.

The parameter Δ is the BCS gap, the gap in the density of single particle states on either side of the superconducting condensate at the Fermi level. Since the gap is measured from the Fermi level to the first single particle state an energy of 2Δ is required to excite the two electrons in a Cooper pair. BCS found that, at absolute zero, the size of the gap is $\Delta(0) = 1.76 k_b T_c$, this so called BCS gap ratio holds true for many superconductors. Shortly after this Gor'kov used BCS theory to derive the Ginzburg-Landau equations and showed that the order parameter ψ_{GL} could be interpreted as the condensate wavefunction and is proportional to the gap parameter Δ [73]. The existence of a gap in the density of states was confirmed experimentally by single electron tunneling experiments [74, 75].

2.2.2 Andreev reflection and the proximity effect

The proximity effect describes the diffusion of Cooper pairs from a superconductor into an adjacent normal metal [58], resulting in the suppression of the order parameter near to the interface on the superconducting side, and the emergence of an induced superconducting gap near to the interface on the normal metal side (shown schematically in figure 2.10).

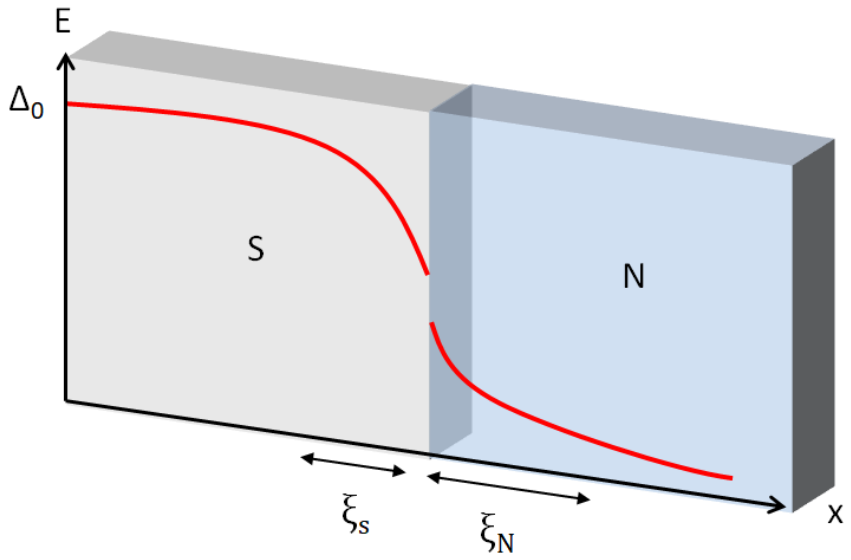

Figure 2.10: The deviation of the order parameter Δ (red line) from its bulk value Δ_0 at a superconductor-normal metal interface. ξ_s and ξ_N refer to the superconducting and normal coherence lengths respectively

The proximity effect is intimately linked to the process of Andreev reflection [76, 77], which describes a mechanism for converting single electrons into Cooper pairs. This can been illustrated by considering the the transport of charge across the S-N interface. If an electron has an energy (relative to the Fermi level) greater than the gap then it can enter the superconductor as a single particle state, but if the electron has less energy than the gap then it cannot enter as a single particle as there are no available states. One might imagine that this would simply lead to the (specular) reflection of the electron back into the normal metal, however Andreev [78] showed that the electron could enter the superconductor as a Cooper pair if a hole was simultaneously *retro*-reflected (shown schematically in figure 2.11) [79]. This results in a transfer of 2e charge across the interface. The retro-reflected hole carriers information about the phase of the condensate back into the normal metal, the length scale over which it can maintain this phase coherence is the normal state coherence length ξ_N which is equal to

$$\xi_N = \frac{\hbar v_F}{k_b T}, \tag{2.29}$$

$$\xi_N = \sqrt{\frac{\hbar D_N}{k_b T}}, \tag{2.30}$$

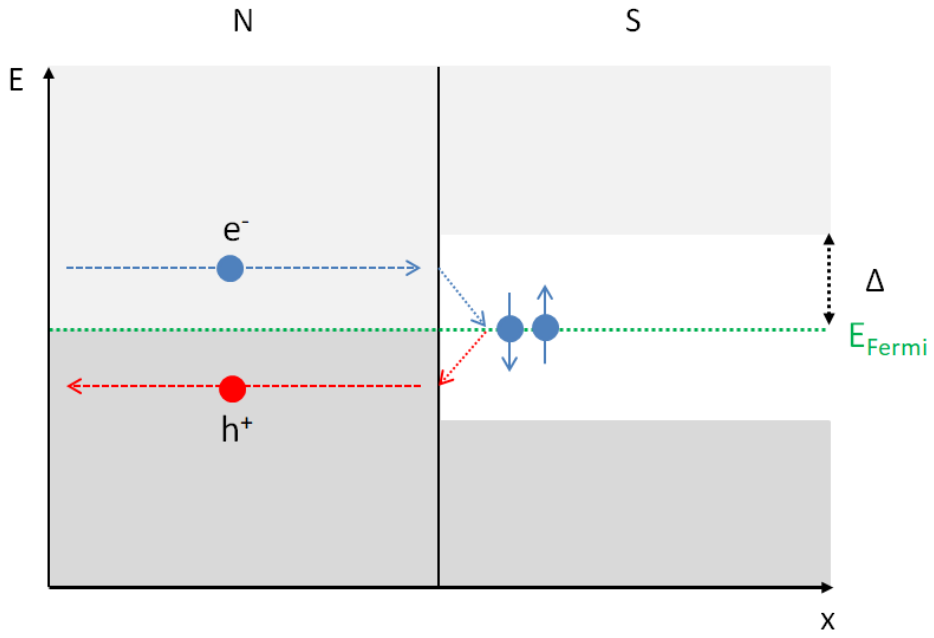

Figure 2.11: A schematic of the Andreev reflection of a hole and creation of a Cooper pair at a S-N interface. Electron occupied states are in dark grey and unoccupied states in light grey.

in the clean and dirty limits respectively. Where v_f is the Fermi velocity and D_N is the diffusion length in the normal metal. This also describes (since Andreev reflection is the mechanism) the length over which Cooper pairs can diffuse into a normal metal.

Blonder, Tinkham, and Klapwijk formulated a model for the transport across the interface between a normal metal and superconductor with a barrier at the interface [80–82]. They showed probability of Andreev and normal reflection are highly dependent on the interface barrier size, if no barrier is present all electrons undergo Andreev reflection but as the barrier hight is increased the probability of normal reflection becomes much larger. A high transparency at the S-N interface is therefore critical for the proximity effect.

2.2.3 The Josephson effect

In 1962 Josephson predicted that a supercurrent would flow between two superconductors separated by a thin insulating barrier even in the absence of an applied voltage [83, 84]. This was observed shortly afterwards by Rowell [85]. A simple derivation of the two Josephson equations given by Feynman [86], (which is applicable regardless of material or mechanism of coupling) is presented below.

Suppose there are two superconductors separated by an insulating barrier thin enough to allow some transport across it, as was the case in the original paper by Josephson. The groundstate wavefuction of the superconducting condensate on either side of the barrier are labeled as ψ_1 and ψ_2, and related to one-another by

$$i\hbar\frac{d\psi_1}{dt} = U_1\psi_1 + K\psi_2, \tag{2.31}$$

$$i\hbar\frac{d\psi_2}{dt} = U_2\psi_2 + K\psi_1. \tag{2.32}$$

Which is simply a time dependent Schrödinger equation for each superconductor, with the energy of each of the condensates described by $U_{1,2}$ and the coupling between them by a constant K, a non-zero value of which allows the exchange of Cooper pairs between the two superconductors. In the case of the energy on either side of the barrier being equal $U_1 = U_2$ the Cooper pairs will be exchanged in both directions at an equal rate, i.e. the net current would be zero. However supposing there is some bias voltage V across the barrier then $U_1 - U_2 = qV$. By fixing the zero of energy to half way between the two superconductors then equations 2.31 and 2.32 become,

$$i\hbar\frac{d\psi_1}{dt} = \frac{qV}{2}\psi_1 + K\psi_2, \tag{2.33}$$

$$i\hbar\frac{d\psi_2}{dt} = -\frac{qV}{2}\psi_2 + K\psi_1. \tag{2.34}$$

The wavefunctions ψ_1 and ψ_2 can be written in terms of the density of electrons on either side of the barrier and the phase of each of the condensates, $\psi_{1,2} = \sqrt{\rho_{1,2}}e^{i\theta_{1,2}}$, where ρ is the density of electrons. This can be substituted into equations 2.33 and 2.34 and solved for the real and imaginary parts to obtain

$$\dot{\rho_1} = \frac{2}{\hbar}K\sqrt{\rho_1\rho_2}\sin\delta, \tag{2.35}$$

$$\dot{\rho_2} = -\frac{2}{\hbar}K\sqrt{\rho_1\rho_2}\sin\delta, \tag{2.36}$$

$$\dot{\theta_1} = -\frac{K}{\hbar}\sqrt{\frac{\rho_2}{\rho_1}}\cos\delta - \frac{qV}{2\hbar}, \tag{2.37}$$

$$\dot{\theta_2} = -\frac{K}{\hbar}\sqrt{\frac{\rho_1}{\rho_2}}\cos\delta - \frac{qV}{2\hbar}. \tag{2.38}$$

With the phase difference set to equal $(\theta_2 - \theta_1) = \delta$ for convenience. Assuming the two superconductors are connected in a loop, such that neither side becomes charged and the potential is kept constant, then the current across the barrier form side 1 to side 2 $\dot{\rho_1}$ (or $-\dot{\rho_2}$), can be written as

$$I = I_c \sin\delta. \tag{2.39}$$

Where $I_c = \frac{2K}{\hbar}\sqrt{\rho_1\rho_2}$ is the maximum supercurrent that can be supported by the junction. This if often referred to as the D.C. Josephson equation. The second pair of equations (2.37 and 2.38) can be combined to obtain

$$\dot{\delta} = \dot{\theta_2} - \dot{\theta_1} = \frac{qV}{\hbar}, \tag{2.40}$$

known as the A.C. Josephson equation. Equations 2.39 and 2.40 describe the general behaviour of Josephson junctions. Firstly when there is no applied D.C. voltage a supercurrent can flow across the junction which is dependent on the phase difference across it. Secondly if a voltage is applied across the junction then the supercurrent will oscillate at a frequency of

$$\omega = \frac{2eV}{h}, \tag{2.41}$$

since $q = 2e$ for a Cooper pair. By applying radiation (typically microwave) this frequency can be locked into, producing a series of steps in the I-V characteristics of the junction, known as Shapiro steps [87]. Due to the fact the step size $\frac{h\omega}{e}$ depends purely on the ratio of two constants, and the frequency of radiation, Shapiro steps are used as the standard for a volt [88, 89].

An important fact that is made clear by this derivation is that the coupling constant K is purely phenomenological, and the nature of the coupling is not important. Provided that some process by which Cooper pairs, and therefore information about the phase of the condensates $\theta_{1,2}$, can be exchanged is present the two Josephson equations will apply.

When Josephson originally considered two superconductors separated by an insulating barrier (known as an S/I/S junction), the coupling mechanism was Cooper pair tunneling, however the barrier need not be insulating. If the superconductors are separated by

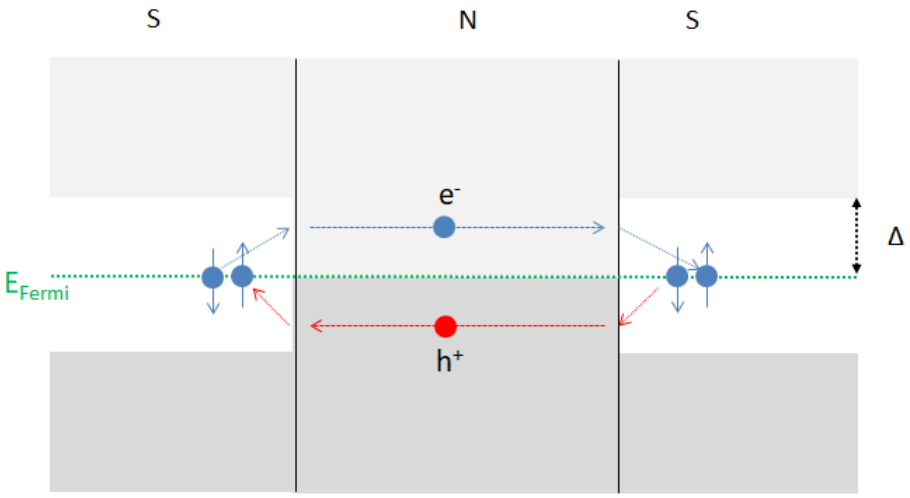

Figure 2.12: A schematic the Andreev reflection of electrons and holes in a normal metal sandwiched between two superconductors. Electron occupied states are in dark grey and unoccupied states in light grey.

a metallic barrier (known as an S/N/S junction) then the coupling can be due to the proximity effect and Andreev reflection.

Consider a situation similar to that discussed in section 2.2.2 but now with an additional superconductor, such that there are two S-N interfaces back to back (shown schematically in figure 2.12). An electron moving left to right joins the second superconductor as a Cooper pair, reflecting a hole. This hole now moves right to left entering the first superconductor and reflecting an electron, this continues cyclically. If the distance between the two superconductors L is comparable to the normal state coherence length ξ_N then the phase information will be preserved and can be shared between the two superconductors creating a Josephson junction. This is equivalent to there being a large overlap in the proximity effects on the two S-N interfaces, allowing a supercurrent to pass through the normal metal. The critical current will vary as

$$I_c = I_{c0} \exp(-L/\xi_N). \tag{2.42}$$

Since ξ_N can be much larger than ξ_s these S/N/S junctions can have a much thicker barrier, than the S/I/S case.

Josephson junctions with non-tunnel-type conductivity (as opposed to tunnel junctions in the S/I/S case) are often referred to as weak links [90]. As well as metallic S/N/S junctions weak links can also be composed of a semiconducting barrier layer S/Sc/S (discussed in more detail in chapter 6) or from superconducting material with a lower T_c. This is often achieved by patterning a small bridge of superconductor to a size of the order of the coherence length ξ_s with two large superconducting banks on either side.

Chapter 3

Experimental Methods

This chapter outlines the experimental methods used in this thesis. In the first section the nanofabrication of superconducting devices using electron beam lithography, optical lithography, and focused ion beam etching is discussed. In the second section details of the low temperature photoconductivity measurements are given.

3.1 Nanofabrication

In this section the techniques and nanofabrication processes used to produce the devices measured in chapter 6 are outlined. The devices are composed of two narrow wires (typically between 500 nm and 2 μm wide) of superconducting niobium (Nb) separated from each other so that the current has to pass through the STO substrate, essentially a Nb wire with a gap somewhere along its length, connected to contact pads so that a pseudo four point measurement can be made. Figure 3.1 (left) shows an optical image of a device, there are four 250 by 250 μm contact pads connected to two 1 μm wide wires separated by a small gap, which is not visible at this magnification. A higher magnification scanning electron microscope (SEM) image of an $\approx$ 400 nm gap is shown in figure 3.1 (right).

The first stage of fabrication is the growth of 50-75 nm thick films of Nb on mixed termination (100) STO substrates, by sputtering. This deposition was carried out by Angelo di Bernardo at the department of material science and metallurgy, Cambridge university and Daniel Chaney in the physics department, Bristol university.

Following the growth of the Nb films three routes were used to pattern devices. Firstly a single stage of electron beam lithography (EBL) and reactive ion etching (RIE) in a sulphur hexafluoride (SF_6) plasma. Secondly one stage of EBL and RIE to define the smallest features followed by optical lithography (OL) and RIE to make wires and contact pads. Thirdly OL and RIE to create large features followed by focused ion beam (FIB) etching to create the smallest features. In this section these techniques will be described in more detail.

Finally once the fabrication of devices is complete samples are attached to a chip holder and contacts made by aluminum wire (1% silicon) wedge bonding, these were then measured in a pumped ^{4}He probe (both are outlined in section 3.2).

3.1.1 Electron beam lithography

The ability to create arbitrary patterns with sub-10 nm feature sizes makes EBL an important and widely used tool in nanofabrication. Patterns are created by coating a sample with a polymer which is sensitive to electron beam irradiation, known as a photoresist. The electron beam produced by an SEM can be used to create a pattern of exposure in this photoresist, which can subsequently be developed in a solvent and used as a protective mask for etching.

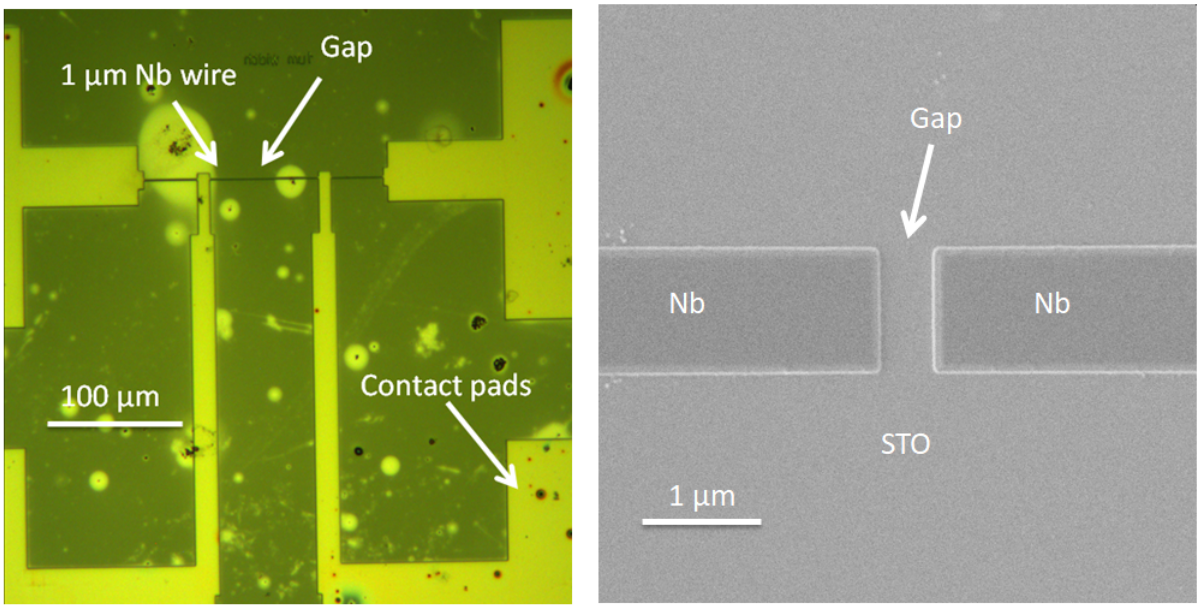

Figure 3.1: (left) An image from an optical microscope of a device, the yellow/green colour is due to a filter on the microscope used in order not to develop resist. (right) An SEM image of the gap in the center of a device with a nominal gap of ≈ 400 nm.

Broadly speaking two types of photoresist exist; *positive* photoresists which become more soluble in the developer solution when exposed and *negative* photoresists which become less soluble. This change is solubility is brought about by breaking (for positive) or cross-linking (for negative) the polymers of photoresist. Both positive and negative photoresists are used in this work.

A basic outline of the fabrication process using a negative photoresist from start to finish is shown schematically in figures 3.2 and 3.3. The steps are;

1. Niobium is deposited on STO by sputtering.
2. Photoresist is spin-coated on the surface.
3. The photoresist is pattered by EBL, and unexposed resist removed by the developer.
4. The sample is etched in a SF_6 plasma.
5. The remaining resist is removed.

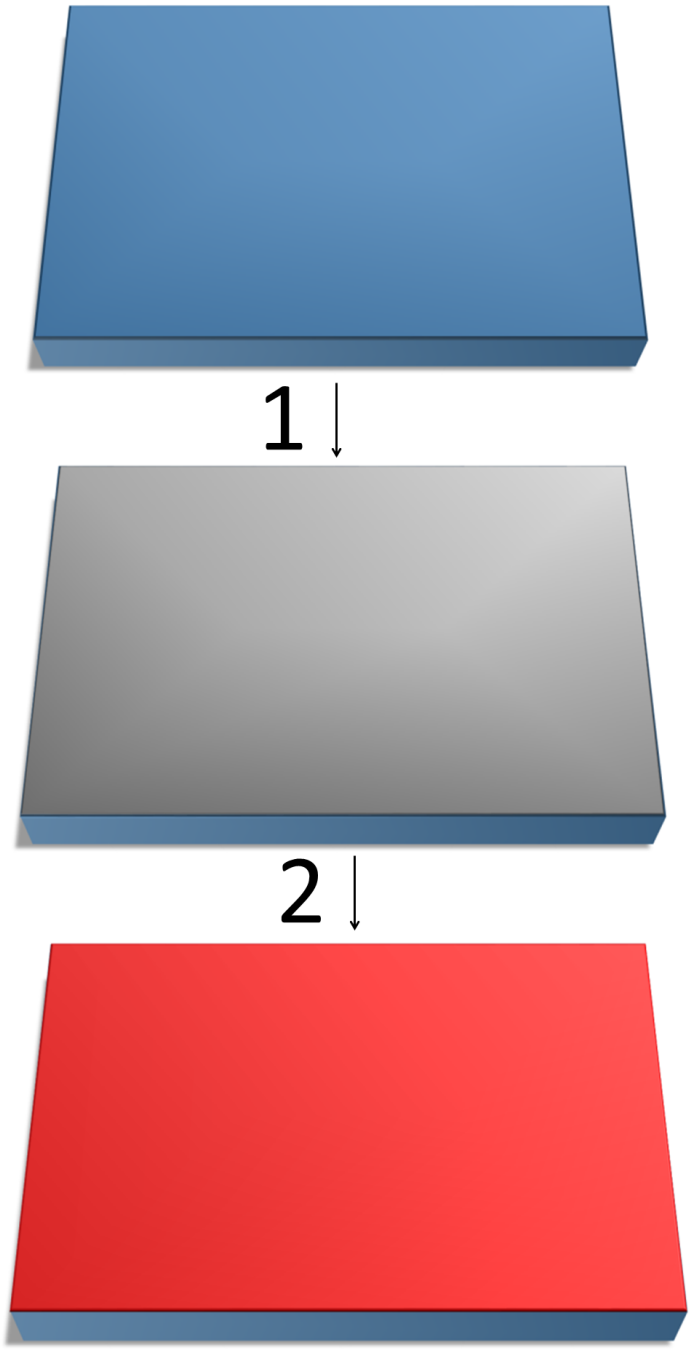

Figure 3.2: A schematic outline of the fabrication process used to make devices, with STO in blue, Nb in silver, and photoresist in red. Steps 1 and 2 represent sputtering of niobium and spinning photoresist respectively. Not to scale.

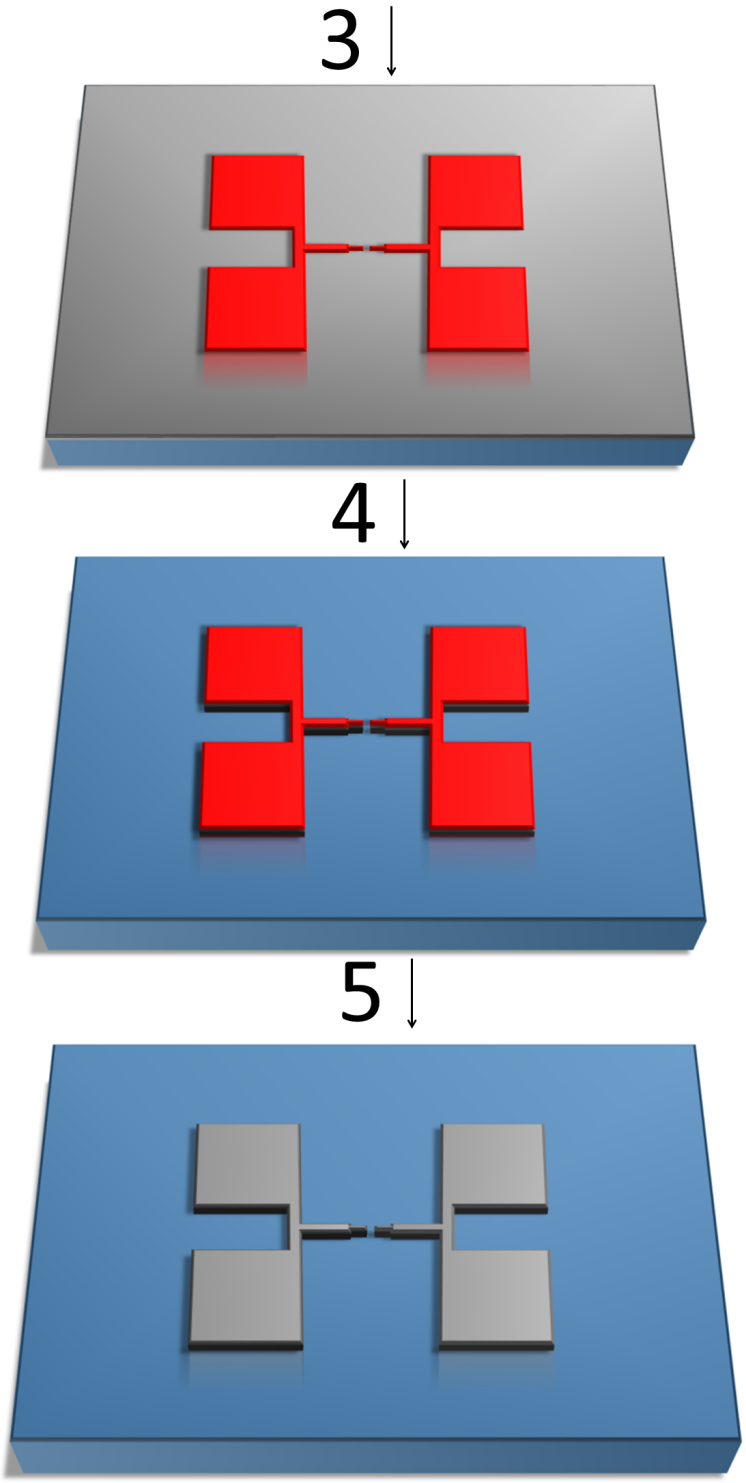

Figure 3.3: A schematic outline of the fabrication process used to make devices, with STO in blue, Nb in silver, and photoresist in red. Steps 3, 4 and 5 represent patterning with EBL, etching and resist removal respectively. Not to scale.

The majority of devices fabricated during the course of this work were made using Zeiss EVO SEM with a Raith ELPHY Quantum Plus interface to allow EBL writing. However later in this work a Raith Voyager dedicated EBL system became available, allowing smaller features to be produced. Consequently two EBL procedures were developed to make devices. Firstly the two step EBL-OL process using the ELPHY quantum system is outlined, followed by the one step process using the Voyager system which was used in the later stages of this work.

3.1.1.1 Two step process-ELPHY Quantum system

Initially devices were fabricated in a single step of EBL using the negative photoresist Ma-N 2400, as shown in figures 3.2 and 3.3. This single stage process had the advantage of being simple however the smallest device size was around 250 nm and results were inconsistent, possibly due to fluctuations in the beam current. Consequently a two step process of EBL and OL was developed. In the first step thin trenches (nominally $\sim$ 100 nm) were made in the positive photoresist poly(methlymethacralate) (PMMA) and etched into the Nb film, then a second step of optical lithography (see section 3.1.2) defined contact pads and a wire which ran over the trench, resulting resulting in a wire with a small gap.

Because the first step of this process could be targeted entirely towards high precision, without the compromise require when also making wires and contact pads, higher resolution structure to be created. For example, because the area of the trenches is small the write time is very short (approximately 1 second compared to 10 minutes for a full device) meaning that drift in the beam current is negligible and the dose more accurate. Furthermore as only a small trench had to be defined in the PMMA rather than the whole device a 50 by 50 μm instead of a 1 by 1 mm write-field could be used, which resulted, for the same exposure dose, in trenches which were about 50 % smaller. A dose test for nominally 100 and 50 nm trenches is shown in figure 3.4, the smallest measured trench width was 100 ± 10 nm, significantly smaller than could be achieved for a single step process.

A critical aspect of this process for achieving 100 nm features is the use of cold development [91, 92]. High resolution structures in PMMA are typically developed in a 1:3 mixture of methyl-iso-butyl-ketone (MIBK) and IPA, at room temperature. Recently, however, Cord *et al.* [93] showed that the optimum temperature for developing was -15

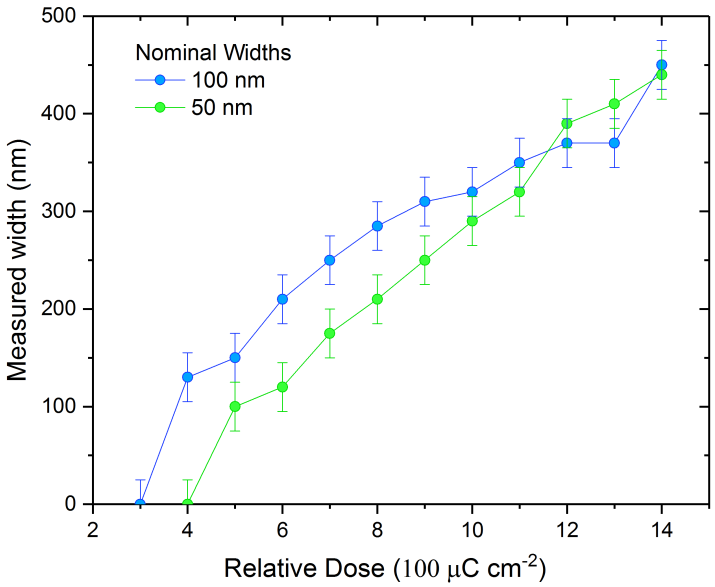

Figure 3.4: A dose test for trenches of nominal width 50 and 100 nm, written in PMMA at 30 kV. This was etched into 50 nm Nb on STO

°C, observing minimum features sizes approximately twice as small as when developed at 15 °C. During exposure PMMA undergoes many chain scissions making the polymers gradually smaller and more soluble as the dose is increased, but at low temperatures the development of all but the smallest fragments is frozen out. This means that partially exposed areas of resist, such as at the edge of the pattern are not removed by the developer, resulting in smaller and higher contrast features. This is particularly useful at low accelerator voltages (such as the 30 kV used here) where the spot size of the beam is typically broader.

The optimised recipe used to create devices is given below;

1. **Clean**: Soak in acetone overnight followed by rinses in isopropyl (IPA) and deionized (DI) water.
2. **Spin**: 950KDa PMMA A4, spun at 4000 rpm for 45 seconds to produce a thickness of 200 nm.
3. **Bake**: 180 °C on a hotplate for 60 seconds.
4. **Exposure**: Exposure dose of 400-500 μCcm^{-2} with a 30 kV beam, 50 pA current.

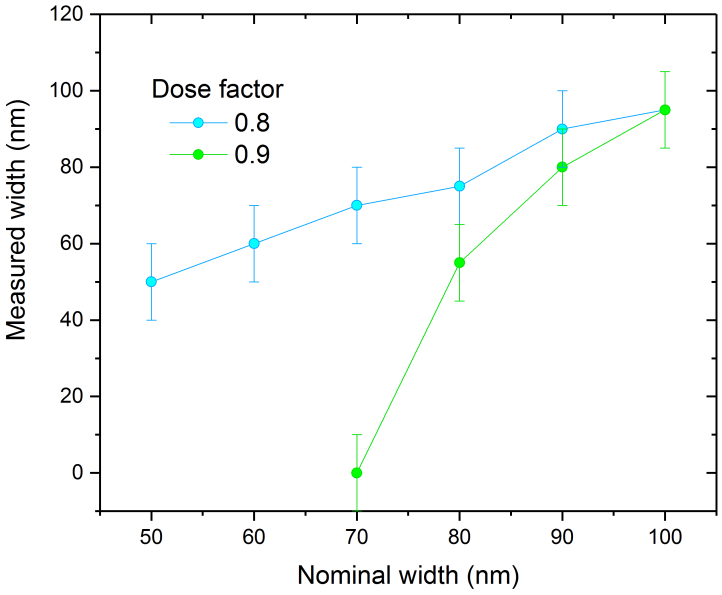

Figure 3.5: Measured vs nominal gap widths for a dose of 160 and 180 μCcm^{-2}. This was etched into 50 nm Nb on STO.

5. **Development**: MIBK:IPA 1:3 at -15 °C for 8 minutes, rinse in -15 °C IPA then room temperature DI water.

To account for the slower rate of development at lower temperature both a longer development time and a higher exposure dose were used. This was found to produce smaller features than just increasing the dose or development time individually.

3.1.1.2 One step process-Voyager system

Later on in this work a Raith Voyager dedicated EBL system became available, and a new fabrication procedure was developed. There were a number of advantages to this dedicated EBL tool over an SEM retrofitted with an EBL interface. For example the 50 kV beam had a smaller spot size and the beam current could both be measured more accurately and was found to be more stable over the write time ($\approx$ 3 hours). Write-fields could be stitched together with an error of only a few nanometers, meaning the whole device could be written over multiple smaller write-fields. As well this, high resolution features could be written at a larger beam current increasing the throughput, meaning than more devices can be made on a single sample (typical 12, as opposed to 4) increasing

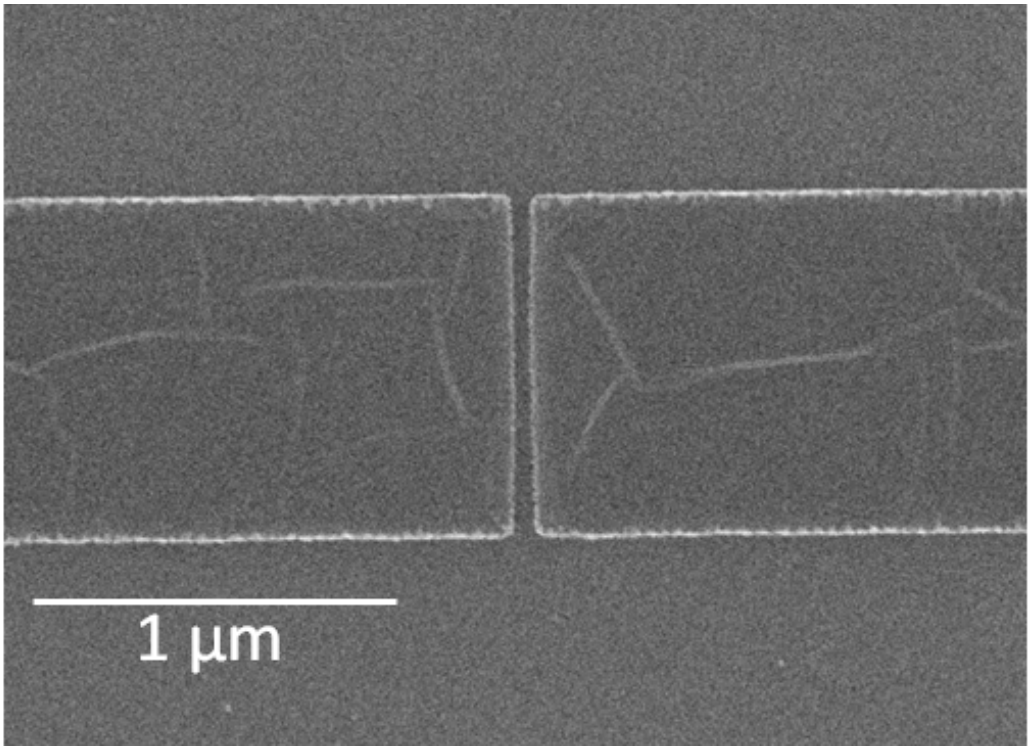

Figure 3.6: An SEM image of a $\approx$ 60 nm device fabricated using the Raith Voyager.

the chance of successful fabrication. These advantages meant that is was possible to make significantly smaller devices with minimum feature sizes of $\sim$ 50 nm.

A one step process using the negative photoresist ma-N 2403 was used to make the devices. In this process two rectangles with a small spacing had to be exposed to create a wire with a gap in it, because they are close together electrons backscattered from the substrate lead to some undesired exposure in the gap. The Raith NanoPECs software was used to perform a proximity effect correction, which adjusted the dose factor along the wire to account for this additional dose allowing more homogeneous gaps to be created. Gaps as small as 50 nm in 1 μm wide wires and 50 nm thick Nb films were fabricated using this method. An example of nominal vs measured widths for dose factors of 0.8 and 0.9 (base dose of 200 μCcm^{-2}) is shown in figure 3.5. The recipe used to create devices is given below;

1. **Clean**: Soak in acetone overnight followed by rinses in isopropyl (IPA) and deionized (DI) water.

2. **Spin**: ma-N 2403 (micro resist technology), spun at 5000 rpm for 45 seconds to produce a thickness of 200 nm (for the highest resolution) or 3000 rpm for 45 seconds

to produce a 300 nm thickness (for higher etch resistance).

3. **Bake**: 90 °C on a hotplate for 60 seconds.

4. **Exposure**: Exposure dose of 160 μCcm^{-2} with a 50 kV beam. A current of 200 pA was used for small features and 2 nA for large features.

5. **Development**: MF-319 60 seconds at room temperature, rinse DI water.

3.1.2 Optical lithography

Optical Lithography uses the same basic principle as EBL; a photoresist is coated on the sample, and a pattern is exposed and developed, which can then be used as a mask for etching or lift off deposition. Rather than using an electron beam to draw out a pattern the sample is exposed to UV light through a mask which blanks out the desired regions. Although the smallest features that can be defined (around 1μm) are much larger than in EBL the process of exposing a sample is much quicker. This makes OL particularly useful for large area exposures (such as contact pads) because the whole sample is flooded with light simultaneously (expect for the parts covered by the mask), so the time taken for exposure is not proportional to the area being exposed. Consequently contact pads can be exposed in a few minutes compared to hours in EBL.

In this work optical lithography was used in two processes. Firstly it was used to create contact pads and wires for devices which had a trenched etched in them (see section 3.1.1.1). Secondly for devices which subsequently had a gap etched in the wire with FIB milling (see section 3.1.3), the mask used for this is shown in figure 3.7. The design consists of a central 2 μm bar with current and voltage contacts connected to it, this allowed 14 devices to be patterned on a single sample.

Optical lithography was performed using a Karl Seuss mask aligner and microposit S1805 a positive photoresist. An additional process which is not required in EBL is the removal of the edge bead, a thicker rim of photoresist which accumulates at the edge of the sample when the resist is spun. This is important as a good contact has to be made between the photoresist and the Cr layer on the glass mask for smaller features to be resolved, and the edge bead causes the mask to sit several microns above the rest of the resist. This is done in two stages, firstly the thickest part of the edge bead is manually removed with a foam swabs suitable for use in a cleanroom. Secondly an exposure is performed with square mask is to leave a 4 mm by 4 mm square of flat photoresist. The optimized recipe

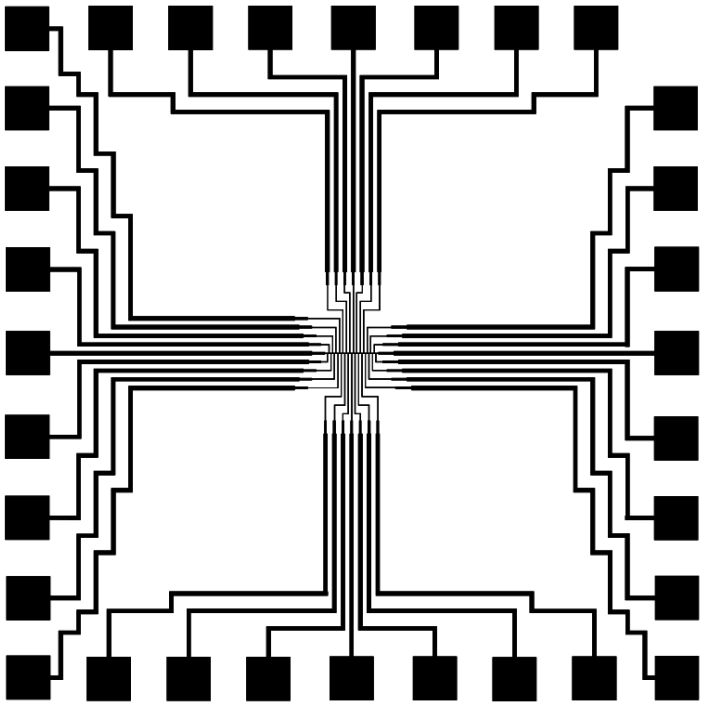

Figure 3.7: The mask design used for patterning the FIB-OL devices, the central features are ~ 2 μm. The total size of the mask is 4 mm by 4 mm.

used to pattern samples is given below;

1. **Clean**: Acetone overnight followed by rinses in isopropyl (IPA) and deionized (DI) water.
2. **Spin**: S1805 (microposit) spun at 4000 rpm for 45 seconds to create a 500 nm thick layer.
3. **Bake**: 115 °C for 60 on a hotplate.
4. **Manual edge bead removal**: the thickest resist at the corners of the sample is removed with acetone and a foam bud.
5. **Exposure 1**: 300 seconds, 4 mm by 4 mm square to remove the remaining edge bead.
6. **Development 1**: MF-31 for 30 seconds at room temperature, rinse in DI water.
7. **Exposure 2**: 120 seconds, contact pads and wires.

8. **Development 2**: MF-31 for 45 seconds at room temperature, rinse in DI water.

3.1.3 Etching

After photoresist masks have been patterned onto the samples either by OL or EBL the final stage of fabrication is etching. Two techniques were used to achieve this, reactive ion etching (dry etching) was used in the vast majority of cases, however for samples with a niobium/aluminum bilayer (see section 6.3.1) an additional step of chemical (wet) etching was required. The same apparatus (an Oxford Instruments plasmalab 100) was used to created thin layers of oxygen vacancies at the surface of STO by Ar^+ irradiation, used in section 4.3, so is also outlined here.

3.1.3.1 Dry Etching

Reactive ion etching combines both chemical and physical etching processes by accelerating a reactive plasma towards a sample, removing material both by sputtering and chemical reaction. In this work a sulphur hexafluoride (SF_6) plasma was used, with a low pressure to create an anisotropic etch profile and avoid undercutting the edges of the pattern. The recipe used is given below;

- **Gas** : SF_6 (100 %)
- **Flow rate**: 5 sccm
- **pressure**: 10 mTorr
- **temperature**: 40 °C
- **Power**: 50 W
- **Time**: 2-3 minutes (dependent on thickness)

3.1.3.2 Wet etching

Whilst Nb and Ti films can be efficiently etched in an SF_6 plasma, Al cannot and in fact is often used as a hard mask for etching silicon with SF_6 [94, 95]. In a small number of samples a thin (5 nm) layer of Al need to be etched, so instead of a plasma of SF_6 a 1:1 DI water:tetramethylammonium hydroxide (TMAH) wet etch was used, after the Nb had been removed by RIE. Samples were submerged for $\approx$ 30 seconds, then rinsed in DI water.

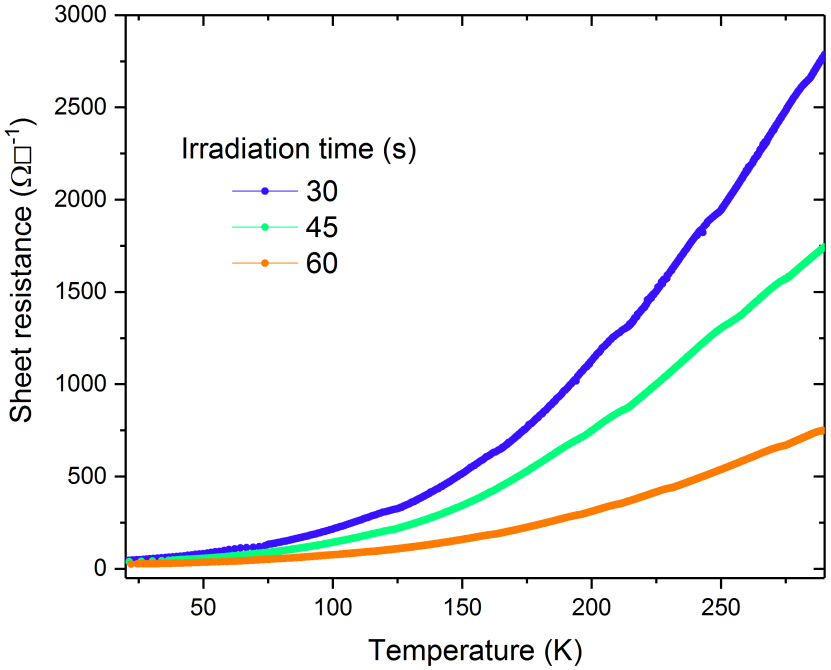

Figure 3.8: $R(T)$s of Ar^+ irradiated STO for three irradiation times.

3.1.3.3 Argon milling of STO

In addition to the etching of devices the Oxford Instruments plasmalab 100 was used to mill the surface of STO with Ar^+ ions in order to create a thin ($\approx$ 20 nm has previously been reported [96]) layer of oxygen vacancies, which act as shallow donors and make the surface conducing. The density defects can be controlled by the time of irradiation, $R(T)$s for 30, 45, and 60 seconds are shown in figure 3.8. The recipe used to create these samples is as follows;

- **Gas** : Ar (100 %)
- **Flow rate**: 25 sccm
- **pressure**: 50 mTorr
- **temperature**: 25 °C
- **Power**: 300 W
- **Time**: 30, 45, 60 seconds ($R(T)$s are shown in figure 3.8)

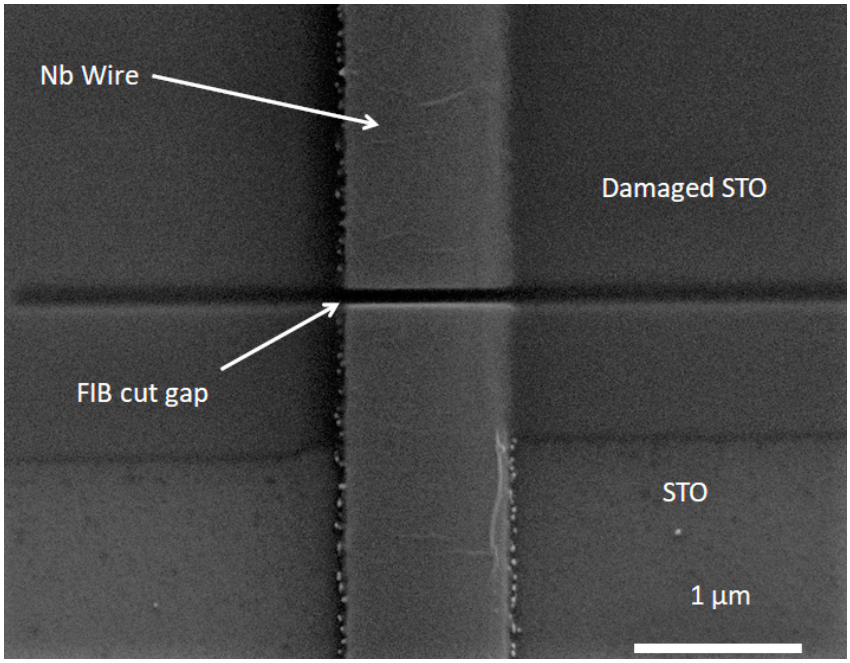

Figure 3.9: An example of a gap, milled by FIB. Damaged STO can be seen around the gap where the edges of the wire have been milled.

3.1.4 Focused ion beam etching

Focused ion beam etching, allows mask-less etching of nano-scale features. An FIB works on a similar principle to an SEM, however rather than an electron source a liquid gallium source is used to emit a beam of positively charged Ga^+ ions, which are accelerated towards the sample [97]. These ions are either implanted or sputter material away from the surface, allowing small features to be milled.

Samples were first patterned by optical lithography using the mask shown in figure 3.7 and etched in an SF_6 plasma, leaving a central 2 μm Nb wire with 31 contacts. A series of cuts with progressively longer times were made across this central bar with a FIB, this was performed by Dr James Darnbrough in the Interface Analysis Center, university of Bristol on a dual beam FIB/SEM. An SEM image of a test cut is shown in figure 3.9. On either side of the wire in the top half of the image the substrate looks visibly different, this region around the gap has also been milled to prevent redeposited "ears" of Nb shorting the devices. A potential downside to this, however, is the implantation of Ga^+ ions, contaminating the surface. Gaps as small as 60 nm were created using this method.

3.2 Low temperature measurements

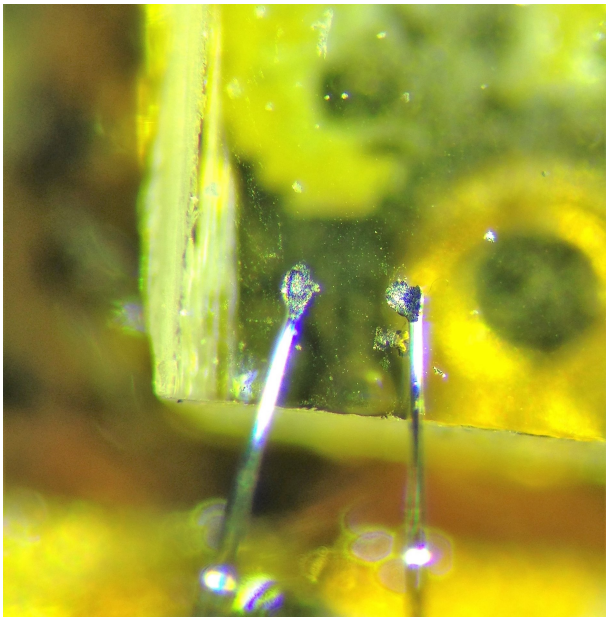

Figure 3.10: An image of an aluminum wedge bond contact on an STO sample, typically more than one contact was made for redundancy. 25 μm 1% silicon aluminum wire was used.

Samples were attached to a chip holder using electrically insulating General Electric (GE) varnish and electrical contacts made so that four-point, current biased, resistance measurements could be performed. A number of methods of making electrical contacts to STO samples were tried including indium, silver paint as well as deposited contact pads such as sputtered chrome/gold, titanium deposited by pulsed laser deposition and direct laser ablation. However aluminum ultrasonic wedge bonds were used in this thesis as they were found to reliably produced low resistance ohmic contacts, an example is shown in figure 3.10

3.2.1 Asahi spectrum LAX-C100

Illumination was provided by a xenon lamp (Asahi spectrum LAX-C100), and custom made fiber-optic cable with a vacuum feed-through. The xenon lamp produces a broad spectrum of light from UVB to infrared (IR), which is passed through a mirror module to cut the spectrum of light and reduce heating. The spectra produced by the IR and UVA modules used in this work are shown in figure 3.4 (top and middle).

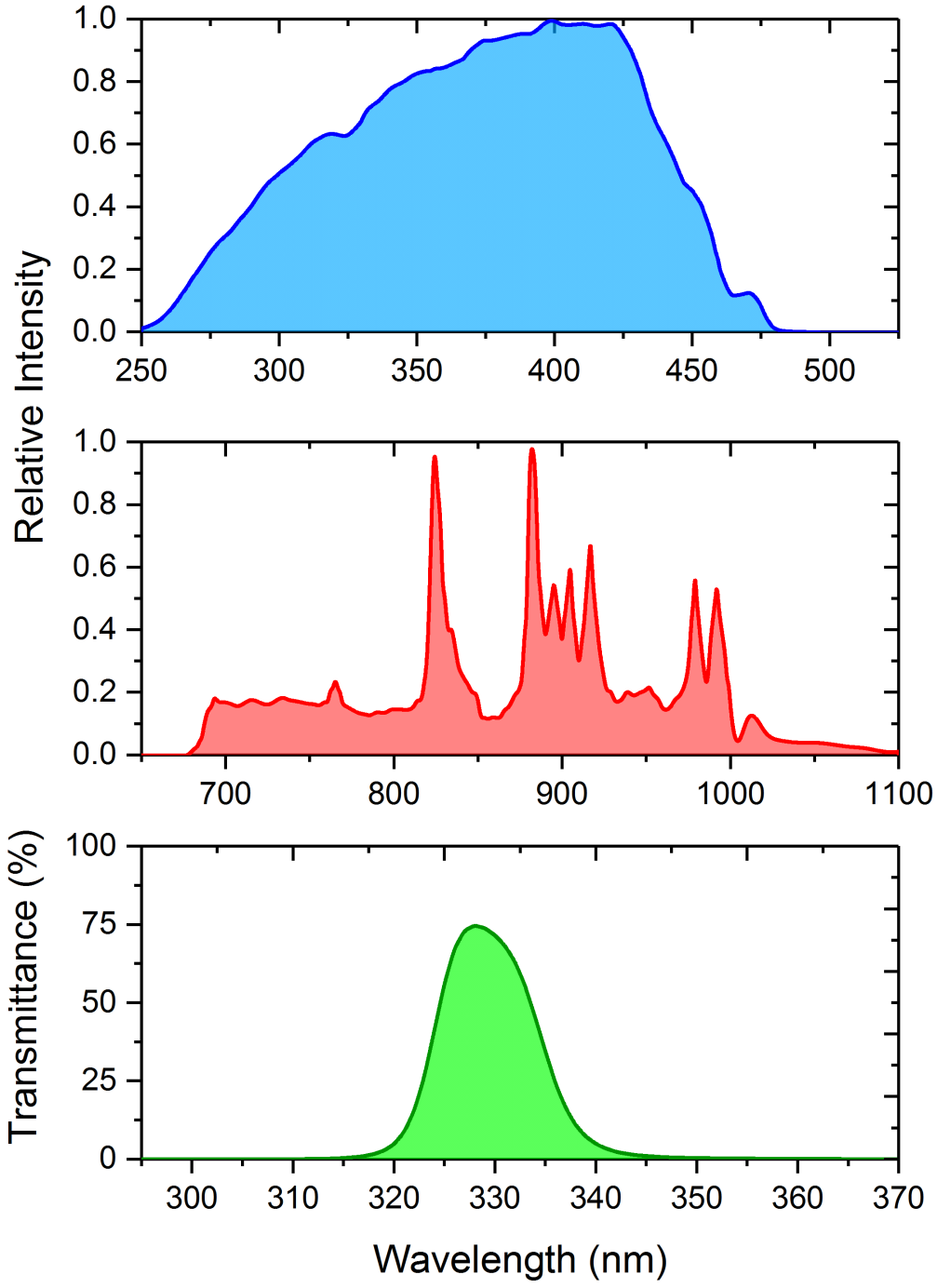

Figure 3.11: The relative intensity of the spectra produced by the UVA mirror module (top) and the IR mirror module (middle), and the transmittance of a 330 nm BPF (bottom). These data were supplied by Asahi Spectrum.

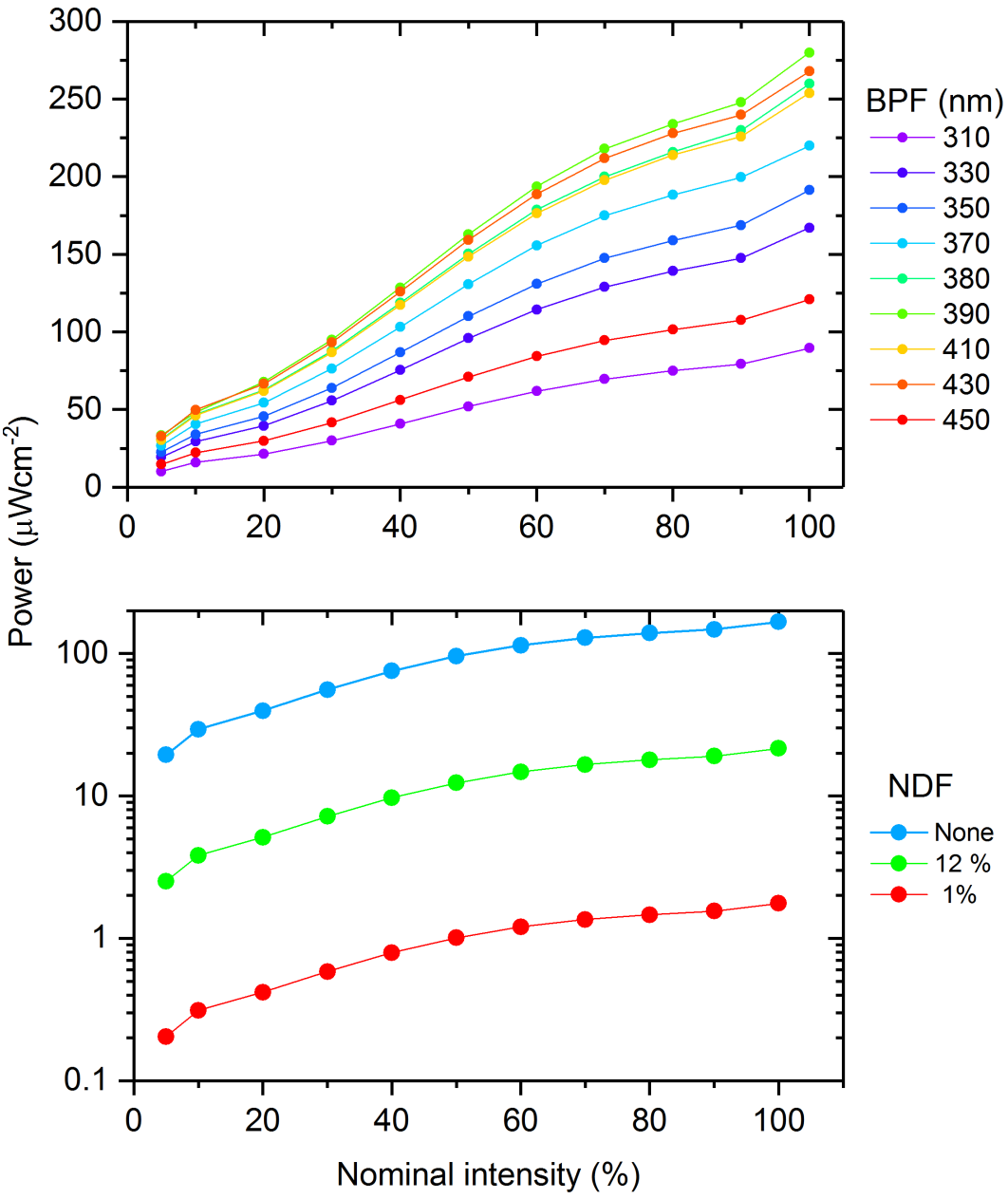

Figure 3.12: An example of a lamp calibration carried out using a Thorlabs S120VC sensor and power meter.

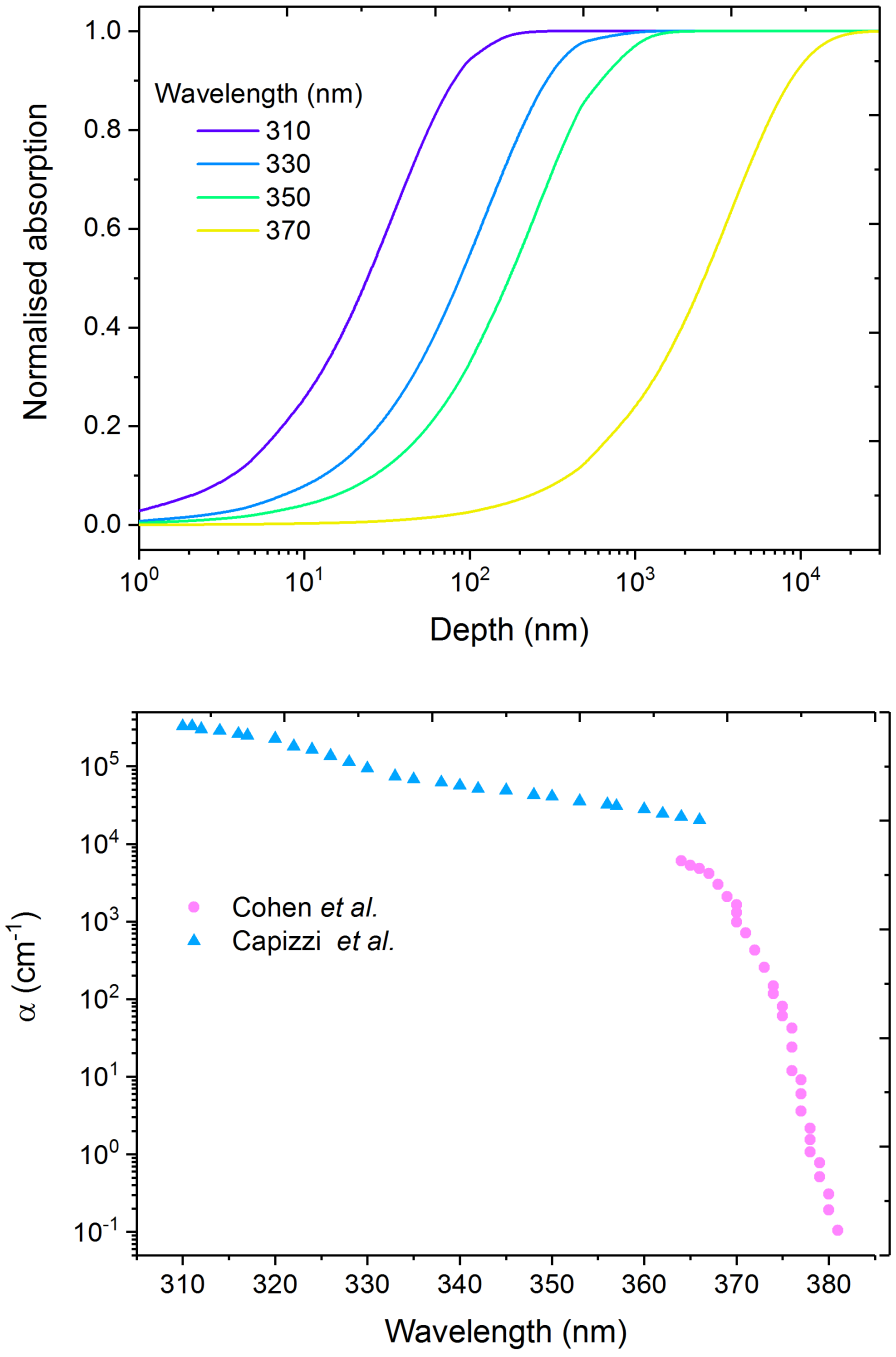

Figure 3.13: (top) Calculated normalised cumulative absorption as a function of depth into the sample and (bottom) data for the absorption coefficient replotted from references [98, 99]

The wavelength of the light was controlled by the use of band pass filters (BPF), which have a FWHM of $\approx$ 10 nm. An example of the transmittance of a 330 nm BPF as a function of wavelength is shown in figure 3.4 (bottom). 310, 330, 350, 370, 380, 390, 410, 430, and 450 nm BPFs were used in this work. The intensity of the light was attenuated by an internal filter, nominally between 5 % and 100 %. In addition to this 1 % and 12 % neutral density filters (NDFs) could be added to reduce the intensity further. By combing two 1 % NDFs power densities as low as $\approx$ 0.1 nWcm^{-2} could be achieved, wheres with no NDFs or BPFs the power density can be as high as 3 mWcm^{-2}. An example of a calibration of the lamp over the range of BPFs and NDFs as a function of nominal lamp intensity is shown in figure 3.5. Intensities were measured using a Thorlabs S120VC silicon photodiode sensor.

Since the absorption in STO is dominated by direct transitions the penetration depth of the light is strongly dependent on the wavelength. Using data for the absorption coefficient α below 100 K from Cohen *et al.* [98] and Capizzi *et al.* [99] in nominally pure STO the profile of absorption can be calculated. The absorption coefficient and normalised cumulative absorption of the light is shown in figure 4.6. Using the range of wavelengths described above it is therefore possible to tune between creating carriers within the first few 10s nm at the surface to almost homogeneously in the bulk 0.5mm thick sample.

3.2.2 The pumped ^{4}He system

The majority of transport measurements presented in this thesis were performed using a custom built pumped ^{4}He probe, with the exception of the data presented in section 4.2.2. Details of this probe are given below.

The chip carrier holding the sample was mounted onto a gold plated oxygen free copper experimental stage situated within a vacuum can, facing upward so that it could be illuminated. A silicon diode thermometer and constantan wire heater were situated close to the sample allowing the temperature to be monitored and controlled by a lakeshore 336. A fiber-optic bundle runs through the central axis of the probe and stops around 100 mm above the sample. Before cooling the pressure inside the probe was reduced to around 10^{-5} mbar with a turbo pump. The probe was then lowered into a bath of liquid helium at 4.2 K. Temperatures below this are achieved by use of a 1 K pot, a small reservoir of helium inside the probe which when pumped on reduces the temperature to as

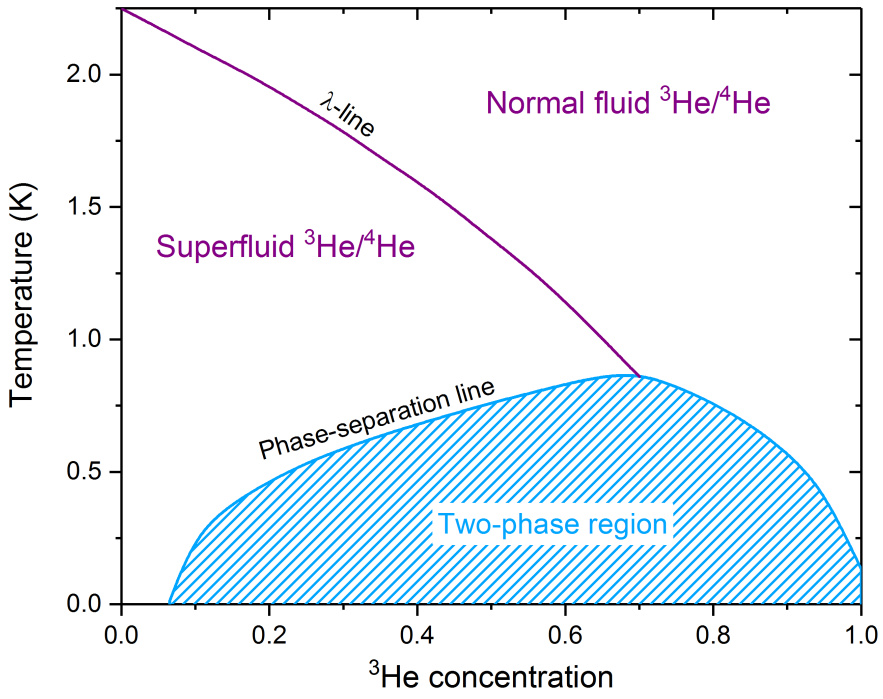

Figure 3.14: ^{3}He-^{4}He mixture phase diagram, based on a similar figure in Pobell [100].

low as 1 K. The helium pumped away is replenished via a small capillary connected to the main bath, the impedance of which results in a trade off between base temperature and cooling power. Due to the need for as much cooling power as possible when the sample is illuminated with high intensity light a low impedance capillary was used, consequently the lowest base temperature achieved was around 3 K. To allow for the fiber-optic bundle to run through the middle the 1 K pot is toroidal in shape. To reduced the magnetic field inside the probe a μ-metal shield is used when superconducting devices were measured.

3.2.3 The dilution fridge

To access still lower temperatures an Oxford instruments Kelvinox ^{3}He-^{4}He dilution refrigerator was used. The phase diagram of ^{3}He-^{4}He mixtures is shown in figure 3.14. Below 0.87 K certain concentrations are immiscible (blue shaded region of figure 3.14) and the ^{3}He-^{4}He mixture undergoes phase separation into a ^{3}He rich phase and a ^{4}He rich phase. The ^{3}He rich liquid is lighter so floats on top of the ^{4}He rich phase. As the temperature is reduced to absolute zero the ^{3}He rich phase becomes pure ^{3}He, however

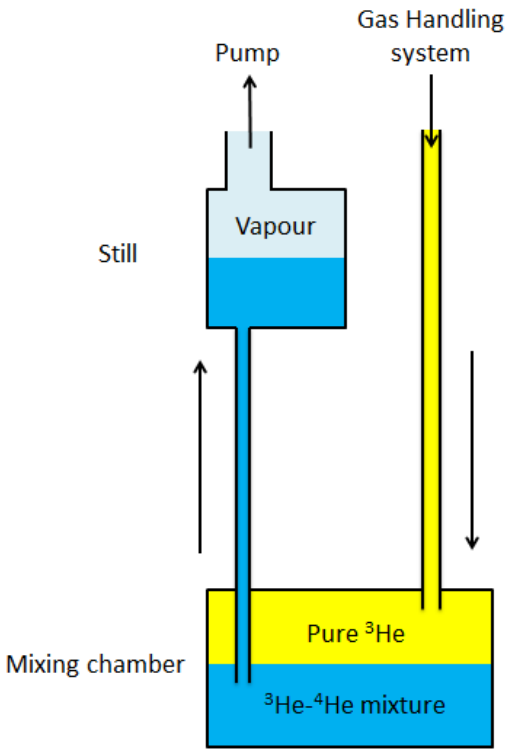

Figure 3.15: A schematic of the flow of mixture in a ^{3}He-^{4}He dilution refrigerator. Adapted from Pobell [100].

a non-zero ^{3}He concentration remains in the ^{4}He rich phase. If ^{3}He is removed from the dilute phase, ^{3}He from the rich phase will replenish it, and cooling is provided by the difference in enthalpy between the rich and dilute phase. This process take place in the mixing chamber of a dilution fridge, shown schematically in figure 3.15. The mixing chamber is connected to a still which is heated to around 0.7 K to distill the ^{3}He from the mixture, which is then recirculated.

To maximize the cooling power and allow optical access the sample stage was mounted directly on the mixing chamber. Using this set up a temperature of ≈ 150 mK could be achieved and when illuminated with a power < 10 μWcm^{-2} a temperature of ≈ 200 mK could be maintained. The same fiber-bundle and xenon lamp as described in the previous section was used to illuminate the sample.

Chapter 4

Photoconductivity in Strontium Titanate

In this chapter results are presented for the equilibrium and transient photoconductivity in stoichiometric $SrTiO_3$ and $SrTiO_{3-\delta}$. Firstly low temperature (4-55 K) measurements of photoconductivity in nominally stoichiometric STO are presented and the possible mechanism behind the large photoconductivity is discussed. Next low temperature measurements (200 mK - 5 K) are presented, reveling the emergence of persistent photoconductivity below 1 K. Lastly the non-equilibrium photoconductivity of $SrTiO_{3-\delta}$ fabricated by argon irradiation is outlined, showing not only the persistent photoconductivity previously observed in bulk $SrTiO_{3-\delta}$ but also transient negative photoconductivity.

4.1 Background and motivation

Undoped, STO is an insulator with a wide band-gap of ≈3.2 eV [1, 2]. By doping with niobium, lanthanum, or oxygen vacancies a metallic state can be achieved [24] and at a carrier density as low as 5×10^{17} cm^{-3} superconductivity emerges [9,10]. An alternative to creating carriers by chemical doping is photoconductivity. When illuminated with above band-gap light electron hole pairs are generated, the electrons are found to be itinerant with mobilitys as high as 10^4 cm^{2}V^{-1}s^{-1} [22, 23], comparable to the highest mobility observed in chemically doped STO [24]. In contrast the holes are found to be localised, and not contribute to conductivity [25, 101]. Photocarrier doping can therefore be used as a tool to add electrons directly into the conduction band. The carrier density can be tuned continuously to $> 10^{18}$ cm^{-3} [102], furthermore by changing the wavelength the depth of photogenerated carriers can also be adjusted, from inducing carriers throughout the bulk of the sample to a thin sheet at the surface.

The key property that makes photocarrier doping a viable alternative to chemical doping in STO is the sheer size of the increase in conductivity which can be induced with light, typically more than 10 orders of magnitude at ≈ 20 K [21]. Changes this large are possible due to the long lifetimes, and consequently large carrier densities for a given generation rate, of photogenerated electrons. The lifetime has been found to increase rapidly, typically by several orders of magnitude, at low temperatures ubiquitously in previous measurements of photoconductivity [22, 25, 28, 101, 103–105]. However the temperature at which this is observed ranges from 35 to 105 K and the origin of the long lifetime of photogenerated electrons at low temperatures is debated. One mechanism which has been suggested is holes becoming trapped by in-gap states created by impurities such as chromium [101] or strontium vacancies [105]. However the increase in lifetime has coincided with cubic-tetragonal phase transition in some works [21, 103], leading the authors to argue this may also contribute to suppressing recombination.

Along with extrinsic states such as defects and impurities, the role of intrinsic self-trapped polaron states is also thought to be important in the recombination of photocarriers in STO. These self-trapped polaron states are quasi-particles composed of an electron or hole and a localised deformation of the lattice (for a recent review see [106]). In nominally pure STO a green luminescence band emerges below 50 K [96, 107] with a lifetime of ≈ 10 ms, which has been attributed to the recombination of electrons and holes in the form of a localised self trapped exciton (STE) [108]. More recently there have been several ob-

servations of photoexcited electrons and holes relaxing into localised self trapped polaron states before recombining [109–114]. Okamura *et al.* [115] and Mizokawa *et al.* [116] both found a high density of in-gap states appearing only after photocarrier generation and found that the majority of the photocarriers were trapped in these states. The influence of this self trapping on the photoconductivity in STO has yet to be established.

Recently several studies have shown that persistent photoconductivity is found in $SrTiO_{3-\delta}$. This was first observed in room temperature measurements of photoconductivity by Tarun *et al.* [117] in 2013. The authors annealed nominally stoichiometric STO at 1200 °C in vacuum with an excess of strontium oxide power, resulting in a metallic sample with a carrier density of 5×10^{15} cm^{-3}. This was found to broaden the spectral response of the STO, with a threshold for absorption shifting from 3.2 eV (the band-gap) to 2.9 eV (430 nm photon energy), and was unaffected by mechanically polished the sample indicating the defects responsible were in the bulk rather than surface. When illuminated with 405 nm light the carrier density was increased to 8×10^{18} cm^{-3}, and when the light was switched off the photoconductivity was found to persist with a lifetime in excess of five days, an example of extremely long lived persistent photoconductivity. Even heating to 426 K was not sufficient to return the sample to its dark conductivity. From positron lifetime measurements the authors attributed the long lived persistence to titanium oxygen vacancy pairs or (in a later work by the same authors) titanium vacancies possibly forming a complex with hydrogen impurities [118]. Subsequently, in a work by the same group, Poole *et al.* [119] found persistent photoconductivity in STO annealed in water vapor at 1200 °C and proposed that oxygen vacancies and hydrogen impurities were responsible.

Bridoux *et al.* [120] also observed persistent photoconductivity in thermally annealed $SrTiO_{3-\delta}$, again attributing it to titanium oxygen vacancy pairs. More recently Snijders *et al.* [121] systematically annealed STO in various environments. The longest lived persistent photoconductivity was observed when silicon impurities, derived from the quartz ampoule, were present in the sample (confirmed by X-ray photoelectron spectroscopy measurements), but the lifetime was also found to be dependent on the density of oxygen and titanium vacancies. The origin of persistent photoconductivity in $SrTiO_{3-\delta}$ is still, therefore, not fully understood.

In this chapter results are presented of a systematic study of the low temperature photoconductivity of both nominally stoichiometric STO and $SrTiO_{3-\delta}$.

4.2 Nominally stoichiometric STO

In this section results are presented for the photoconductivity of nominally stoichiometric STO, studied systematically using the illumination intensity to tune the carrier density and wavelength to tune the depth over which carriers are created. Firstly in section 4.2.1 measurements of photoconductivity between 4 and 55 K are outlined, secondly in section 4.2.2 results are presented for measurements at temperatures as low as 200 mK, an as yet unexplored temperature range.

Using data for the optical absorption coefficient form Cohen *et al.* [98] and Capizzi *et al.* [99] the penetration depth of the light at the central wavelength of the five bandpass filters used in this section was calculated, this is shown in table 4.1. The penetration depth can be used as a guide to the thickness of the induced sheet of electrons and to tune between bulk like behaviour at 370 nm to surface sensitive behaviour at 310 nm. The results presented in each subsection were taken using a single sample of mixed termination (100) STO, however qualitatively similar results were also found in other samples.

Table 4.1: Optical penetration depth (at the central wavelength) for the five wavelengths of light used. The data for the absorption coefficient α, is taken from Cohen *et al.* [98] and Capizzi *et al.* [99].

λ (nm)	E_{photon} (eV)	α (cm^{-1})	penetration depth
310	4.00	2.77×10^{-1}	31 nm
330	3.76	1.34×10^{3}	110 nm
350	3.54	3.94×10^{4}	250 nm
370	3.35	9.35×10^{4}	7.5 μm
380	3.26	3.28×10^{5}	36 mm

4.2.1 The photoconductivity of STO

The spectral response of photoconductivity as a function of temperature for two powers (0.5 μWCm^{-2} and 50 μWCm^{-2}), is shown in figure 4.1. A sharp cut off of photoconductivity is observed at the band-gap with no measurable photoconductivity found when illuminated with 390 nm light, in agreement with previous measurements [25]. The photoconductivity is largest at 370 nm and becomes progressively smaller as the wavelength decreases. One possible cause of this is a lower mobility in thiner sheets of photocarriers due to enhanced surface scattering. Kozuka [23] found the mobility to be around twice

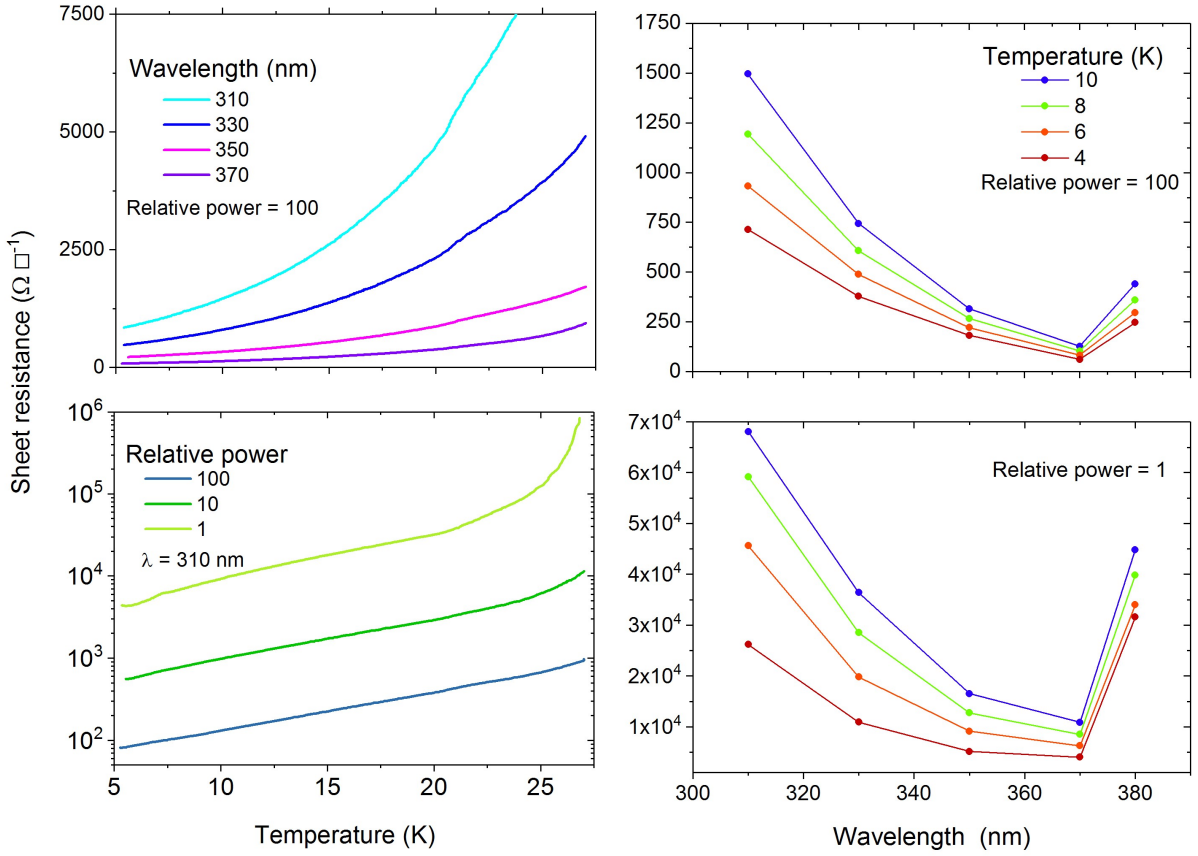

Figure 4.1: $R(T)$s as a function of wavelength (top left) and power (top right). The spectral response of photoconductivity as a function of temperature (bottom left) and power (bottom right) at $T = 10$ K. A relative power of 100 corresponds to 50 μWCm^{-2}.

as large at 370 nm compared with 310 nm, which would be insufficient to explain the difference between photoconductivity at 310 nm and 370 nm observed here. More rapid recombination at the surface due to the presence of fast recombination centers is typical for photoconductors [122], which could also explain the lower photoconductivity for shorter wavelength illumination. Transient measurements of photoconductivity, shown in figure 4.3 (bottom left), do indeed show a faster decay in photoconductivity when 310 nm light is used to illuminate the sample compared with 370 nm, indicating the presence of fast recombination centers which decrease the lifetime at the surface. It is possible that a combination of both lower mobility and lifetime contribute to the smaller photoconductivity observed at shorter wavelengths.

The photoconductivity induced by 380 nm light does not, however, follow this trend showing a lower photoconductivity than 370 nm illumination. The penetration depth

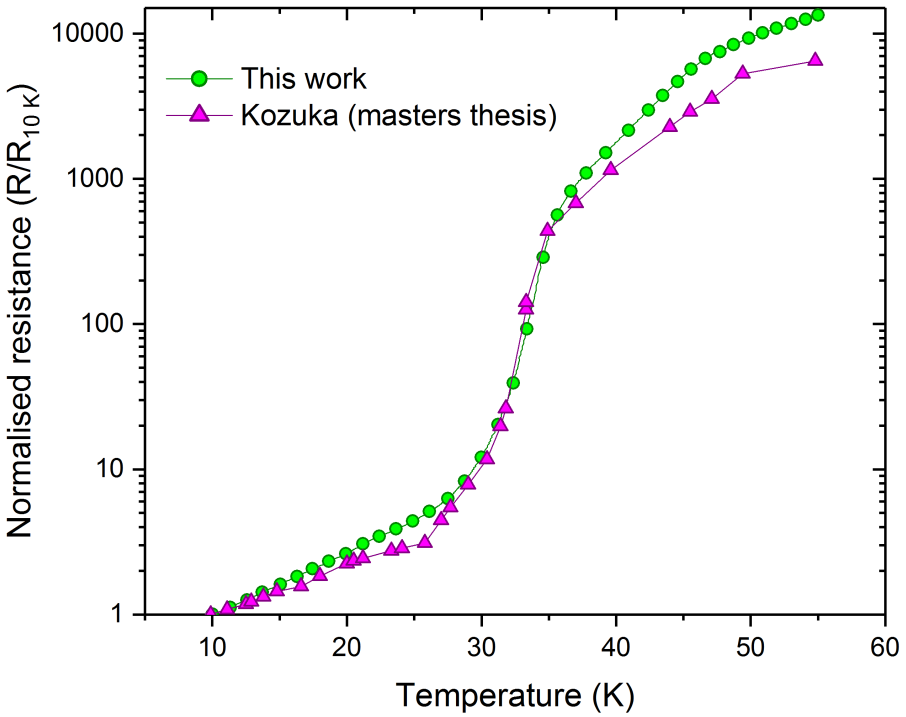

Figure 4.2: Photoconductivity normalised to $T = 10$ K, as a function of temperature (green circles) using a lamp power of 100 μWCm^{-2} and wavelength of 370 nm, and data taking using the same conditions by Kozuka [22](purple triangles).

of 380 nm light is larger than the thickness of the sample meaning that a significant proportion of light will simply pass through, therefore for the same flux of photons fewer carriers will be generated.

$R(T)$s were also measured, shown in figures 4.1 and 4.2. Between 5 and 25 K the resistance was found to increase by approximately one order of magnitude irrespective of the wavelength or intensity of the light used to illuminate the sample. This is consistent with measurements made by Kozuka [22] who previously showed that this change was caused by a decrease in mobility from $\approx 10^4$ cm^{2}V^{-1}s^{-1} to 10^3 cm^{2}V^{-1}s^{-1} over this temperature range. A direct comparison of the photoconductivity normalised to 10 K, when illuminated with 370 nm, 100 μWCm^{-2} light is shown in figure 4.2. The data obtained in this work is in good agreement with that of Kozuka [22], and shows a large increase in resistance centered at ≈ 35 K, which Kozuka showed was due to a reduction in the carrier density by approximately two orders of magnitude.

A large decrease in resistance at low temperatures of between two and four orders of magnitude has been ubiquitously observed in measurements of photoconductivity in STO [25, 28, 101, 103–105], although both the mechanism and temperature at which this occurs are debated. Katsu *et al.* [103] found that the photoconductivity increased by approximately three orders of magnitude between 100 and 30 K. The onset of large photoconductivity coincided with cubic tetragonal phase transition, suggesting that this may be important. Later Ishikawa *et al.* [104] observed an isotope effect, comparing the photoconductivity of $SrTi^{16}O_3$ and $SrTi^{18}O_3$. They found that $SrTi^{18}O_3$ did not show large photoconductivity at low temperature and argued that this was due to its ferroelectricity increasing the rate of recombination [25].

On the other hand several authors have suggested that the origin of the long lived photogenerated electrons is the trapping of holes in sensitizing levels, where the cross section for hole capture is much larger than the cross section of electron capture, $\beta_p \gg \beta_n$. Consequently for recombination to take place, either the holes would have to be thermally reexcited into the valance band or recombine directly with electrons in the sensitizing level. At low temperature both of these processes have a low probability and therefore recombination is suppressed. Strong evidence for this hole trapping scenario has been provided by both Feng [101] and Osawa *et al.* [105], both having shown that the increase in photoconductivity at low temperatures could be completely removed when the samples are illuminated simultaneously with UV and IR light. These authors have argued that the IR light causes optical quenching, optically reexciting holes back into the valence band leading to recombination with electrons. At higher temperatures the photoconductivity is not suppressed by the IR light, which indicates the transition to large photoconductivity at low temperature is due to the onset of hole trapping.

Feng [101] found that the increase in photoconductivity occurred between 60-80 K, increasing with higher illumination powers and suggested that this was due to the presence of a sensitising level thought to be due to chromium impurities in the sample. More recently, however, both Kozuka [22] and Osawa *et al.* [105] have observed the sharp increase in conductivity at around 35 K, consistent with the data presented here. Furthermore in contrast to Feng, Kozuka showed that the temperature at which this occurred did not have a significant dependence on the wavelength or intensity of light used to illuminate the sample. Together these results imply the 35 K transition to large photoconductivity may an intrinsic property STO.

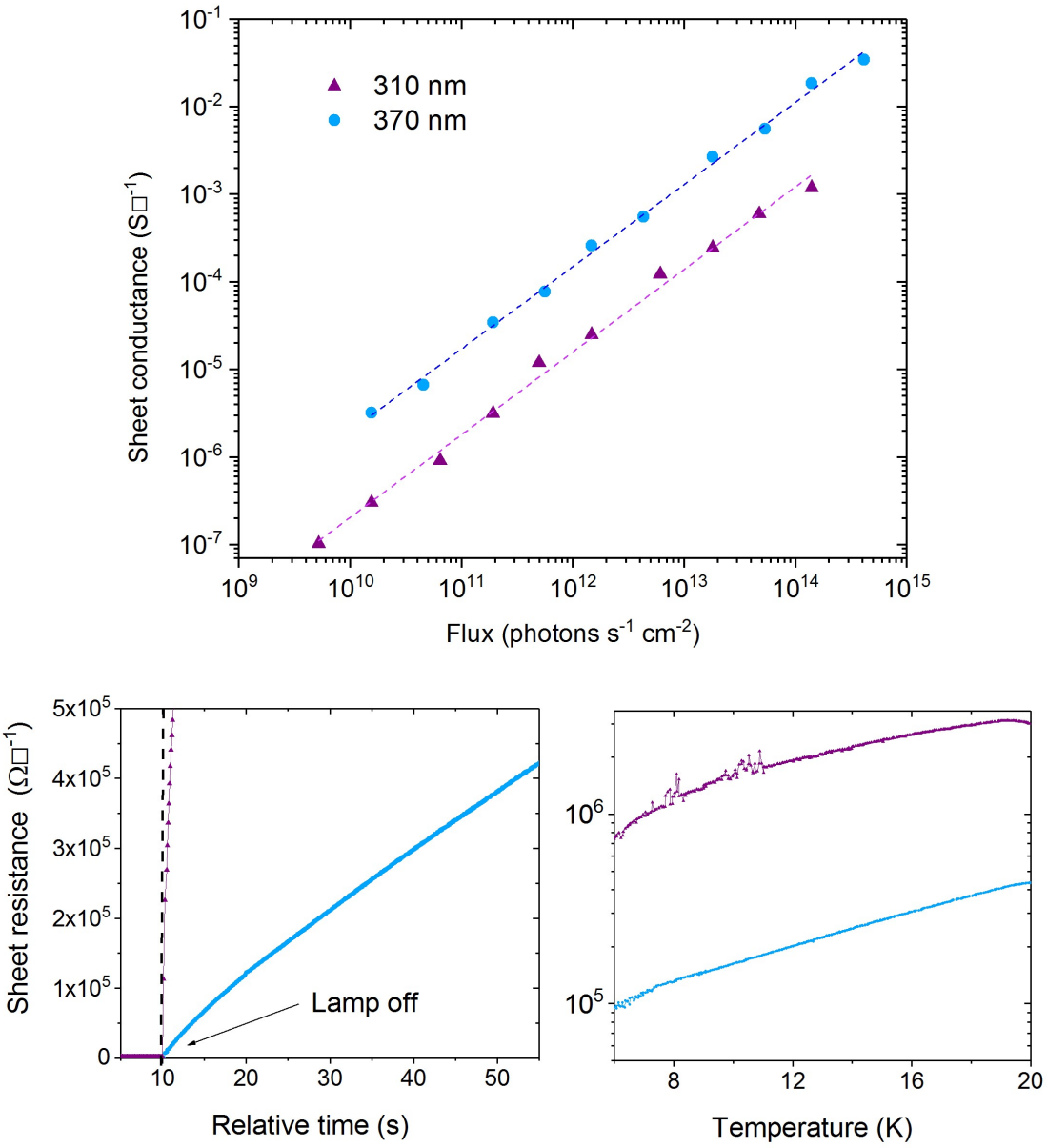

Figure 4.3: Sheet conductance as a function of photon flux for 310 nm and 370 nm light at $T = 10$ K (top). Linear fits are shown (dashed lines), which yield $\gamma = 0.94$. The decay in photoconductivity after the shutter was closed at a relative time of 10 s at $T = 10$ K using a lamp power of 50 μWCm^{-2} (bottom left), and $R(T)$s for 310 nm and 370 nm light using a lamp power of 0.05 μWCm^{-2} (bottom right).

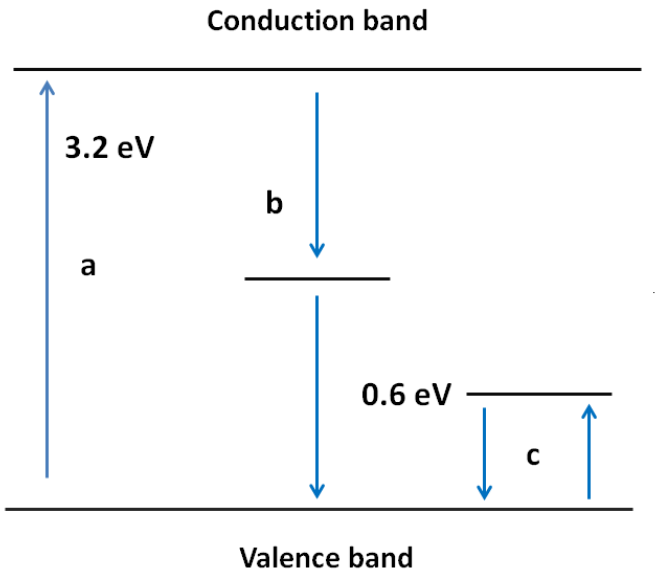

Figure 4.4: A schematic representation of the possible defect levels and transitions involved in the two center recombination model proposed by Osawa *et al.*; a) direct absorption and creation of an electron hole pair, b) recombination of an electron and hole via an efficient recombination center, and c) trapping and detrapping of a hole at a sensitizing level located 60 meV above the valence band.

Building on the model of a sensitizing level leading to hole trapping at low temperature Osawa *et al.* performed numerical simulations of the temperature dependence of the onset of large photoconductivity, for a system with a sensitizing level and an efficient recombination center, a schematic representation of this is shown in figure 4.4. From this the activation energy required for hole detrapping was calculated to be ≈ 60 meV, and was attributed to strontium vacancies. Since these are doubly negatively charged the capture cross section is much larger for holes than electrons, even when occupied with a hole.

To investigate the hole trapping scenario further photoconductivity was measured as a function of incident photon flux over the full range accessible to the xenon lamp and neutral density filters used in this work, this is shown in figure 4.3. Measurements were made for 310 nm and 370 nm light in order to distinguish between surface and bulk behaviour respectively, as well as to access the highest and lowest three dimensional carrier densities possible. This data can be used as a proxy to study the relationship between generation rate and number of carriers ($n \propto G^{\gamma}$), if it is assumed the mobility is constant ($\sigma \propto n$) and the efficiency of absorption is not dependent on flux ($G \propto$ flux).

Both sets of data were found to be well fitted to a straight line on a log-log plot with a gradient of $\gamma = 0.94$, close to linear photoconductivity (see section 2.1.1).

$$\sigma \propto n \propto G^{0.94}. \tag{4.1}$$

This indicates that monomolecular recombination dominates, rather than direct band to band bimolecular recombination which would produce a value of $\gamma = 0.5$, and is consistent of the two center model proposed by Osawa *et al.*. Physically a value of $\gamma \approx 1$ corresponds to the lifetime of photocarriers not depending on the density. Assuming a mobility of between 10^3 $\mathrm{cm^2V^{-1}s^{-1}}$ and 10^4 $\mathrm{cm^2V^{-1}s^{-1}}$, and approximating the carrier profile to that of a homogeneous 30 nm thick sheet, a maximum carrier density of between 10^{18} $\mathrm{cm^{-3}}$ and 10^{19} $\mathrm{cm^{-3}}$ can be estimated. Since the lifetime does not change over the full range of carrier densities, this indicates that the sensitizing levels have not become saturated with holes. A simple estimate of the lower limit of the density of sensitising levels is therefore $\approx 10^{18}$ $\mathrm{cm^{-3}}$ [32]. Measurements of the defect density in undoped STO have found densities between 10^{18} $\mathrm{cm^{-3}}$ and 10^{19} $\mathrm{cm^{-3}}$ for strontium vacancies [123]. The data presented here is therefore supportive of the model of hole trapping by strontium vacancy defects proposed by Osawa *et al.* [105].

Finally, the role of self trapping of both electrons and holes on photoconductivity should also be considered. Recent density functional theory (DFT) calculations by Hao *et al.* [124] have shown that electron polarons only form in stoichiometric STO when the carrier density is in excess of 10^{20} $\mathrm{cm^{-3}}$, with electrons remaining delocalised below this threshold. Since this is around two orders of magnitude higher that the maximum carrier density estimated here, the formation of electron polarons is not expected to occur. In contrast DFT calculation made by Janotti *et al.* [125] have shown that the formation of hole polarons is energetically favorable in stoichiometric STO at any carrier density. The binding energy of these self trapped holes is ≈ 50 meV, similar to that of strontium vacancies making the two difficult to distinguish. One the other hand hole polarons do not necessarily have a strongly asymmetric capture cross section for electrons and holes like strontium vacancies, meaning that captured holes would be more likely to undergo recombination in a self trapped polaron state than a strontium vacancy. Given that several photoluminescence studies have shown that photocarriers are localised before recombination it seem more likely that hole polarons are the recombination center described in the model above.

Previously Kozuka *et al.* [23] reported a metal insulator transition in photodoped STO when illuminated with low density (corresponding to a flux of $\approx 10^{12}$ photons $s^{-1}cm^{-2}$) 310 nm light. This was shown to be caused by a reduction in the mobility and attributed to the onset of weak localisation. However in the data presented here photoconductivity is linear over the full range of carrier densities measured (around two orders of magnitude lower than by Kozuka *et al.*) and does not show any evidence for weak localisation. Furthermore $R(T)$'s at a normalised power of 0.01 retain a metallic temperature dependence, shown in figure 4.3. There are a number of potential explanations of this discrepancy. Firstly measurements presented here were taken at 10 K in contrast to at 2 K by Kozuka *et al.*, possibly reducing the effect of weak localisation. Although Kozuka *et al.* did observed that the onset in a reduction in mobility occurred at 10 K. Alternatively it is possible that the reduction in mobility observed by Kozuka *et al.* is in fact due to a low density of electron traps at the surface, which localised the majority of electrons at low generation rates, but only a small fraction at high generation rates, thus yielding a density dependent mobility.

4.2.2 Photoconductivity below one Kelvin

Previously photoconductivity measurements of STO have not been made at temperatures lower that 2 K [23], however there are potential interesting phenomena which may occur at these temperatures. In particular STO becomes superconducting below $T = 300$ mK when optimally doped. Photocarrier doping is a potentially attractive alternative to chemical doping, both because the carrier density can be tuned *in situ*, potentially allowing the phase diagram to be mapped out with a single sample and because photocarriers can be introduced homogeneously unlike chemical dopants which have been shown to form clusters [126, 127]. Previous measurements suggest a maximum carrier density of 10^{18} cm^{-3} is achievable by photocarrier doping using a power of ≈ 50 μWcm^{-2}, at which the superconducting critical temperature is ≈ 200 mK. Motivated by this, measurements of photoconductivity in STO were made at temperatures as low as 200 mK.

Figure 4.5 shows the wavelength and power dependence of photoconductivity for 370, 350, 330, and 310 nm light, at 200 mK. A similar spectral response to at higher temperatures is observed, but with a slightly larger relative conductivity at 370 nm. The resistance of the sample as a function of power using 310 nm light at temperatures of 250, 500, and 750 mK was also measured, shown in figure 4.5. Due to heating caused by illuminating the sample, a maximum power of ≈ 20 μWcm^{-2} could be achieved at 250

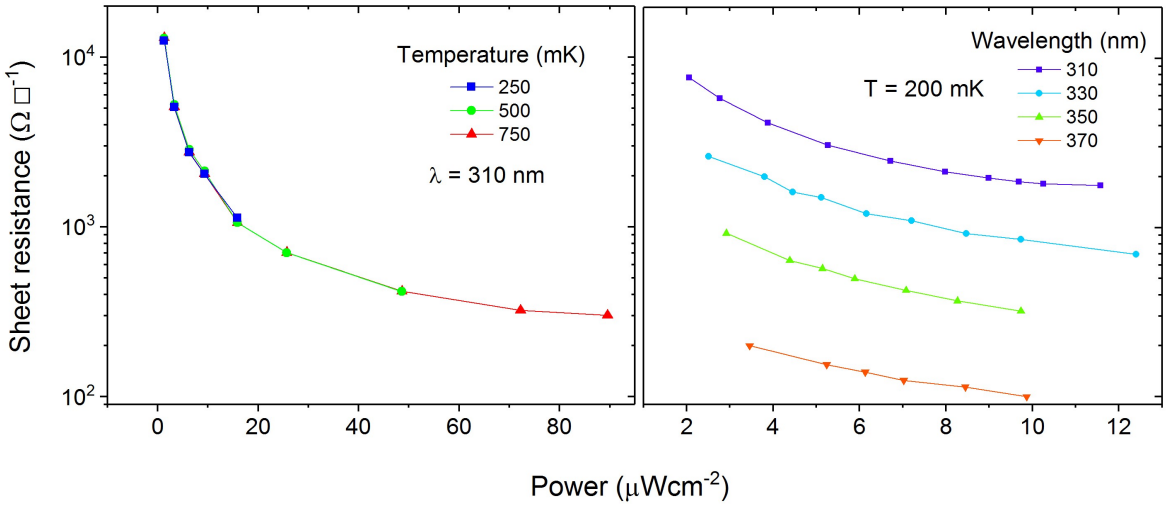

Figure 4.5: Photoconductivity as a function of power at 250, 500, and 750 mK, using 310 nm light (left), and as a function of power for 370, 350, 330, and 310 nm light at T = 200 mK (right).

mK, corresponding to a photoinduced carrier density of just under 10^{18} cm^{-3}. This is substantially lower than the optimal carrier density of around 10^{20} cm^{-3} and the critical temperature is expected to be less than 100 mK [10], explaining why superconductivity is not observed. This was confirmed by IV measurements, all of which were linear, showing no critical current $I_c > 10$ nA. Whilst it may be possible to tune the critical temperature of a chemically doped sample, the existing (dark) carrier density would have to be much larger than the maximum achievable by photoconductivity in order for the critical temperature to be ≈250 mK and therefore measurable using this setup. This would drastically reduced the level of tunability which could be achieved by photocarrier doping, for example the carrier density of an optimally (chemically) doped sample could be enhanced by less than 1 % with illumination. Pursuing lower temperatures is therefore a more promising route to realising optically tunable superconductivity. Despite this, one striking behaviour which was observed at low temperatures is the emergence of long lived persistent photoconductivity below 1 K.

Measurements of non-equilibrium photoconductivity were made by illuminating the sample with 5 μWcm^{-2}, 370 nm light of 300 seconds, before the shutter was closed and the photoconductivity allowed to decay. Results are shown in figure 4.6 over two temperature ranges, 200-1000 mK (top) and 1.5-5.5 K (bottom).

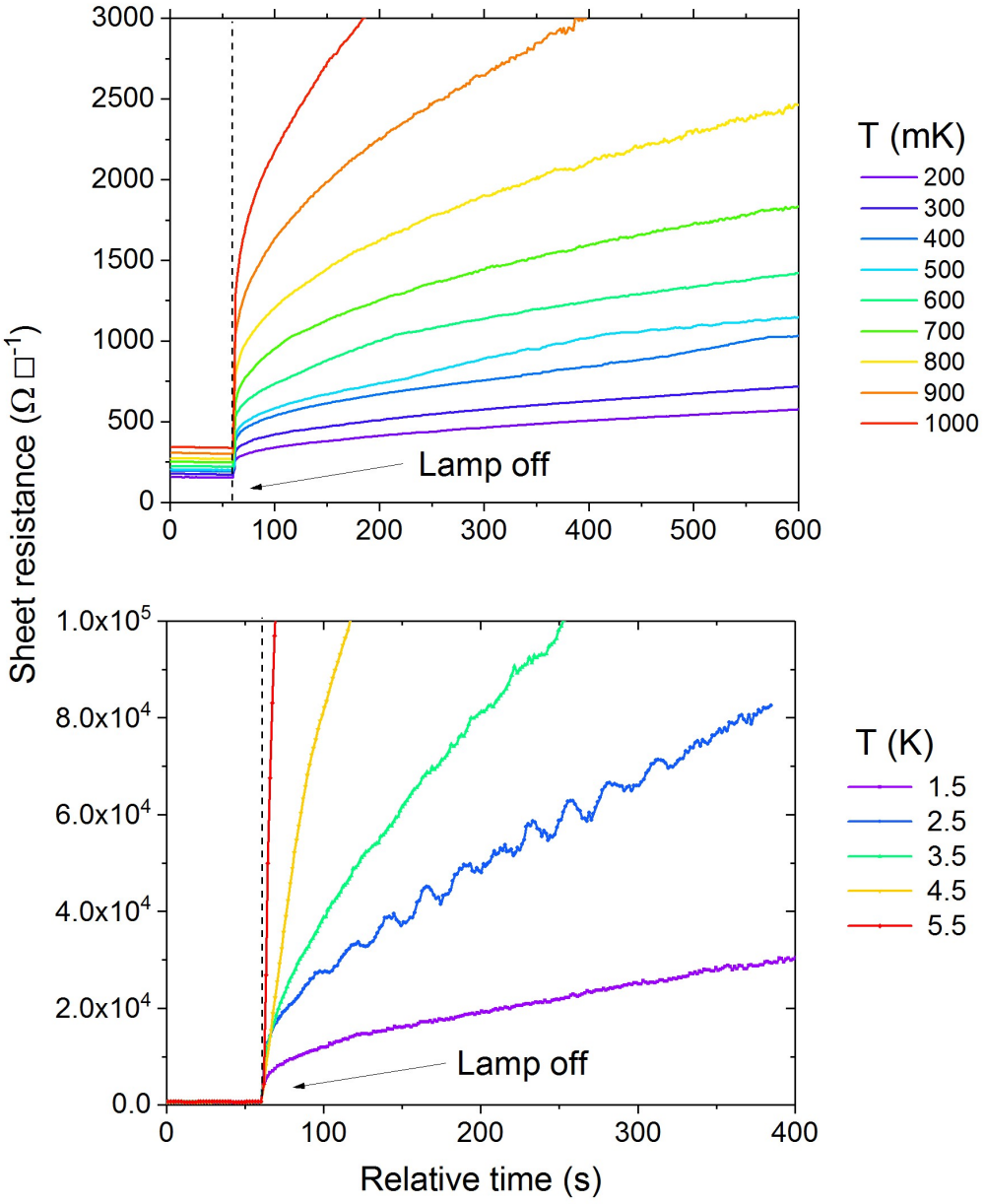

Figure 4.6: The decay in photoconductivity between 200 and 1000 mK (top) and 1.5 and 5.5 K (bottom). 370 nm, 5 μWCm^{-2} light was used to illuminate the sample. An oscillation in the decay was observed at 2.5 K, this was attributed to a PID driven oscillation in temperature.

The decay in conductivity was fitted with a stretched exponential function (an example is shown in figure 4.8.),

$$\frac{\sigma(t)}{\sigma(t=0)} = \exp\left(\left(-\frac{t}{\tau}\right)^{\beta}\right), \tag{4.2}$$

however good fits could not be obtained by either single or double exponentials decays. The parameters from this fit are shown in figure 4.7. Below 1 K significant persistent photoconductivity emerges, the lifetime increasing as the temperature is lowered from 0.9 s at 1 K to 135 s 200 mK. At higher temperatures the persistent photoconductivity is quickly removed, for example at 200 mK the resistance of the sample remains below 500 $\Omega\square^{-1}$ almost 10 minutes after illumination has ceased, compared with more than 70 $k\Omega\square^{-1}$ at 2.5 K. Once the temperature is increased to 5.5 K the rate of decay of photoconductivity is similar to that shown in figure 4.3, which was measured at 10 K.

In section 4.2.1 the long lifetime of photogenerated electrons was attributed to the suppression of recombination by the trapping of holes at a sensitizing level. In a simple model of thermally activated detrapping of holes from a single level the lifetime is expect to vary as $\frac{1}{\tau} \propto \exp\left(-\frac{E_a}{k_b T}\right)$, where E_a is the activation energy. Therefore the gradient of an Arrhenius plot of $\ln(\tau)$ against $\frac{1}{T}$ is equal to $\frac{E_a}{k_b}$, this is shown in figure 4.6. Two distinct regions of linear behaviour centered around 500 mK, are observed and can be assigned activation energies of $\approx$ 40 and 300 meV below and above 500 mK respectively. Whilst the 40 meV activation energy is relatively close to that of a strontium vacancy sensitizing level (60 meV), the increase in activation energy at 500 mK is difficult to justify physically. Furthermore the stretching parameter was found remain at a constant value of $\beta \approx 0.16$ from 200 mK to 1 K, suggesting that the mechanism of the decay doesn't change dramatically at 500 mK. Alternatively this may indicate that the lifetime does not follow typical Arrhenius-type thermal detrapping, and some other temperature dependent process is contributing to changing the lifetime. At low temperature the rate direct recombination via the sensitizing level may become comparable to the rate of detrapping, this would lead to a smaller temperature dependence of lifetime, potentially explaining the sub-Arrhenius behaviour shown here.

A distinctive wavelength dependence is also found, with persistent photoconductivity only observed when 370 nm or 380 nm light was used to illuminate the sample. A comparison between decays of 370 nm and 330 nm light at 400 mK is show in figure 4.8 (bottom right). This indicates that low temperature persistent photoconductivity is a

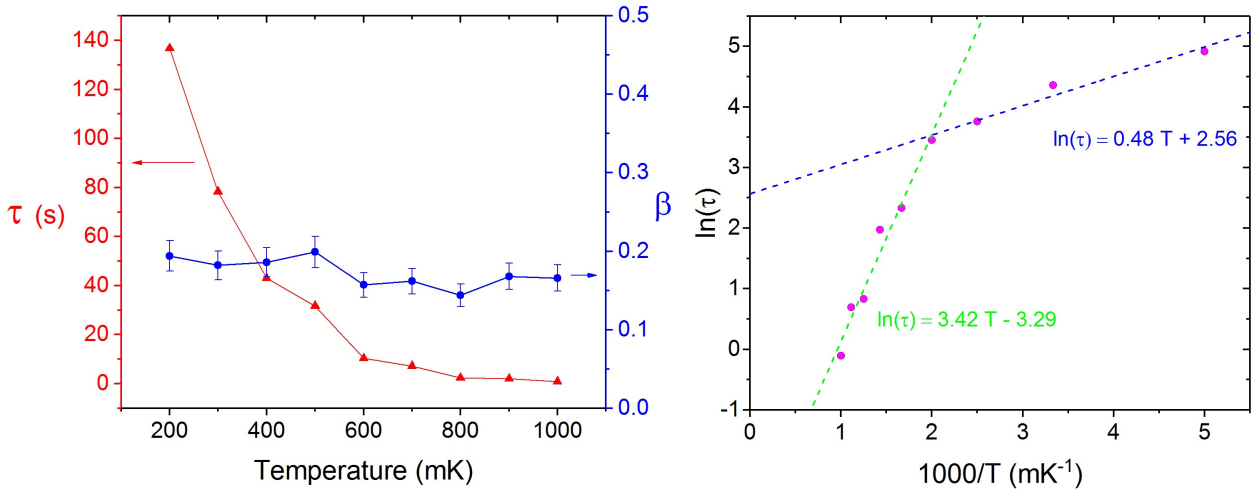

Figure 4.7: The fitting parameters from a stretched exponential fit (left) and an Arrhenius plot for the extracted lifetime between 1000 and 200 mK (right).

bulk phenomena and does not occur at the surface, perhaps due to the presence fast recombination centers quenching the traps, or suppressing retrapping. Furthermore the bulk nature of the persistent photoconductivity observed here implies that the origin is hole trapping rather than spatial separation, which typically occurs when one of the carrier is localised at the surface or an interface. When the sample is illuminated with 390 nm light there is no measurable photoconductivity, as was the case in section 4.2.1. This implies that the defect which is responsible for persistent photoconductivity is within $\approx$ 100 meV of the valence band.

Previously Feng [101] and Osawa *et al.* showed that hole trapping could be quenched by illuminating samples simultaneously with UV and IR light. Similar optically quenching can be seen here in figure 4.8 (top right). This was achieved by illuminated the sample first with UV light, closing the shutter and allowing photoconductivity to relax for around five minutes, then illuminate the sample with broadband IR light ($\approx 20\ \mu\mathrm{Wcm}^{-2}$). The second illumination, using IR light, is found to increase the rate of recombination indicative of optically detrapping holes. Furthermore the photoconductivity is found to decay faster when lower powers were used to illuminate the sample, implying the hole traps have not been saturated, this is shown in figure 4.8 (top left).

Collectively these data are indicative of a large density of hole traps leading to long

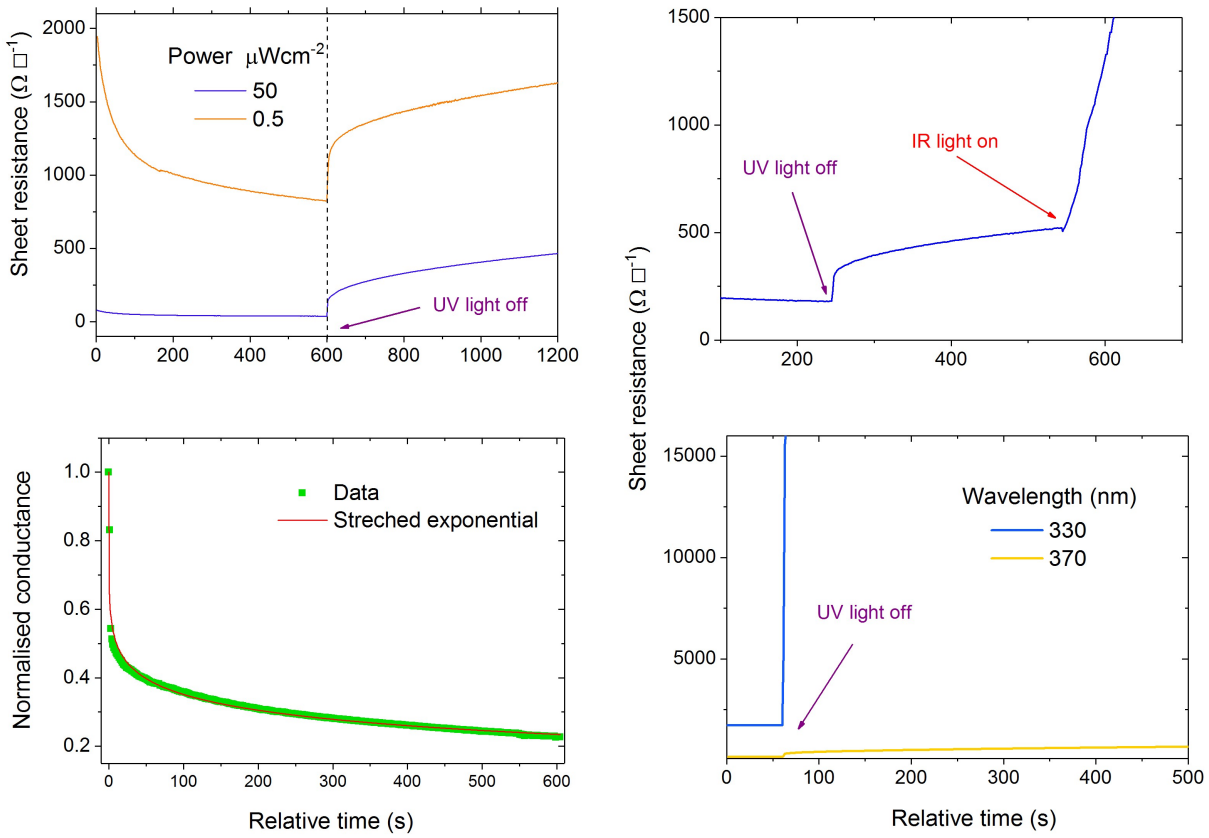

Figure 4.8: The build up and decay of photoconductivity of 0.5 and 50 μWcm^{-2} 370 nm light at $T = 400$ mK (top left), an example of a stretched exponential fit to the decay at $T = 200$ mK (bottom right), low power (20 μWcm^{-2}) IR quenching at $T = 400$ mK (top left) and a comparison of decay of 330 and 370 nm light at $T = 400$ mK.

lived bulk persistent photoconductivity. Whilst a stretched exponential decay is often attributed to either a multi-step serial relaxation [50] or to several parallel channels of relaxation [50], it can also arise from the decay of a single level if there is strong retrapping [32]. Using data for the dielectric constant in STO from muller *et al.* [128] and equation 2.10, the variation in the capture cross section of an attractive defect with temperature can be estimated. Between room temperature and 5 K the cross section becomes around 3 times smaller, however lowering the temperature further to 300 mK the cross section is increased by a factor of ≈ 250. Therefore a negatively charge defect would have a much larger rate of hole trapping at 300 mK compared with 5 K, coinciding with the onset of persistence observed here. Therefore it seems likely that the strontium vacancy sensitizing level, which was earlier used to explain the long photogenerated electron lifetimes at higher temperatures, is also the origin of the persistent photoconductivity shown here.

4.3 Photoconductivity in $SrTiO_{3-\delta}$

Previous measurements of bulk thermally annealed $SrTiO_{3-\delta}$ have shown long lived persistent photoconductivity [119–121], sometimes on the timescale of days [117]. As an alternative to thermal annealing oxygen vacancies can be produced by irradiating STO with a beam of argon ions [129–131]. This has previously been shown to produce a layer of oxygen vacancy rich $SrTiO_{3-\delta}$ with a thickness of $\approx$ 20 nm, and an amorphous top layer of $\approx$ 3 nm [96, 132]. Due to the potential applications of Ar^+ irradiated STO as a transparent oxide conductor much attention has been given to studying it, particularly as samples can also be patterned allowing the fabrication of doped nano-structures [133].

In this section measurements of the build up and decay of photoconductivity in Ar^+ irradiated STO, as a function of wavelength, temperature, and lamp power, are presented. The addition of a large density of oxygen vacancies dramatically increases the time scale over which these processes occur, and leads to long lived persistent photoconductivity. Whilst persistent photoconductivity has previously been measured in bulk $SrTiO_{3-\delta}$, results presented here suggest that transient negative photoconductivity also occurs, which has not previously been observed in any STO based nano-structures or bulk samples.

A series of 5 mm $\times$ 5 mm, nominal stoichiometric STO samples with progressively larger doses of Ar^+ irradiation were fabricated (see section 3.1.3.3). This resulted in range of sheet resistances at room temperature from 10's k$\Omega\square^{-1}$ to 10's $\Omega\square^{-1}$, all showing a metallic temperature dependence. From this a sample with a resistance of $\approx$ 50 $\Omega\square^{-1}$ at 10 K was selected, such that there was still a significant tuneability with light but a large number of oxygen vacancies were present. Although the amorphous top layer in Ar^+ irradiated STO is thought to be passivating, samples were found to increase in resistance at room temperature and in air on the time scale of days. This was presumably due to the reoxidization of the surface, or the build up of surface absorbents, consequently samples were fabricated then cooled down within a few hours.

4.3.1 Results and discussion

The build up and decay of photoconductivity as a function of wavelength, when illuminated with 50 μWcm^{-2} light at 10 K is shown in figure 4.9. The shutter was opened after 100 s of measuring the dark resistance (relative time of 100 seconds in 4.9 top), left open

for the photoconductivity to build up for 300 seconds, then closed allowing the excited carriers to decay (relative time of 100 seconds in 4.9 bottom). Broadband IR light (≈ 2 mWcm^{-2}) was found to quench the persistent photoconductivity (as described in section 4.2.2) allowing a dark resistance of $R = 47.2 \pm 0.2\ \Omega\square^{-1}$ to be consistently achieved, between measurements.

The spectral response of photoconductivity (shown in figure 4.10) is found to be similar to that of stoichiometric STO (see figure 4.1). The largest enhancement in conductivity occurs when 370 nm light is used to illuminate the sample increasing the conductivity by a factor of ≈ 4 compared to the dark state. However in contrast to stoichiometric STO photoconductivity is observed when illuminated with below band-gap energy light (390, 410, 430, and 450 nm). Since these wavelengths have insufficient energy to create electron hole pairs by a band to band excitation they are not absorbed by stoichiometric STO, therefore any absorption of this light must take place via an in-gap state in the $SrTiO_{3-\delta}$ layer. In-gap states have previously been shown to mediate the creation of free carriers by a two photon absorption process [134], leading to a sub-gap photocurrent. The broadening of the spectral response to at least 450 nm suggests the existence an in-gap state or states which reduces the energy of absorption by ≈ 0.5 eV, consistent with photoluminescence measurements of Ar^+ irradiated STO [96] and bulk $SrTiO_{3-\delta}$ [135].

After the lamp was switched off long timescale persistent photoconductivity can be observed, similarly to in previous measurements of bulk $SrTiO_{3-\delta}$ [117, 119–121]. Figure 4.10 shows an example of the decay over ≈ 20 hours, even after this time a significant photoconductivity remains. Amongst the above-gap light the longest lifetimes are observed for the shorter wavelengths, indicating that the enhancement in photocarrier lifetime occurs close to the surface of the sample, where oxygen vacancies are present. For longer wavelengths of light the photoconductivity is larger, however a rapid initial decay occurs after illumination has ceased. This is indicate of bulk photocarriers decaying quickly, with the persistent photocarriers remaining near to the surface. In the persistent photoconductivity observed in bulk $SrTiO_{3-\delta}$, the origin of long photogenerated electron lifetimes was thought to be related to hole trapping by in-gap states. In Ar^+ irradiated STO in-gap states only exist in the $SrTiO_{3-\delta}$ layer at the surface. It is possible that the persistent photoconductivity could be caused either by hole trapping by in-gap states in the $SrTiO_{3-\delta}$ layer, or alternatively the positively charge oxygen vacancies may lead to a spatial separation of electrons and hole without trapping.

The decay of photoconductivity is well fitted to a stretched exponential function (equation 4.2), but not to single or double exponentials. Good fits can also be made to a logarithmic decay,

$$\frac{\sigma(t)}{\sigma(t=0)} = 1 - \alpha \ln\left(\frac{t}{\tau_0} + 1\right), \tag{4.3}$$

which has previously been associated with persistent photoconductivity due to charge separation in GaAs heterostructures [49]. Examples of both fits are shown in the inset of figure 4.9. Stretched exponentials are used here, however, for consistence with the majority of the literature on persistent photoconductivity.

An $R(T)$ of the sample between room temperature and 10 K, performed before any exposure to UV light and the decay of photoconductivity as a function of temperature between 10 and 35 K, using a power of 50 μWcm^{-2} and wavelength of 310 nm are shown in figure 4.11.

Prior to any UV exposure the sample shows a metallic temperature dependence between 300 and 10 K, with a RRR $\approx$ 38, which is consistent with previous measurements [133]. When illuminated the temperature dependence is weak between 10 and 35 K only changing by $\approx 3\ \Omega\Box^{-1}$. After the shutter was closed the rate of decay was almost exactly the same across the range of temperatures, in fact after 300 seconds the photoconductivity was slightly larger at 20 K compared with 10 K. This would seem to imply the rate of decay is not primarily driven by the rate of thermal detrapping over this range of temperatures. The rate of recombination may be dominated by the frequency of encounters of electrons and holes rather than a thermal detrapping process. In this case a larger mobility would lead to more frequent encounters of electrons and holes and therefore quicker recombination [136,137]. The rate is often described by the Langevin model [138]

$$R \propto (\mu_e + \mu_p). \tag{4.4}$$

The mobility of Ar^+ irradiated STO is not found to vary significantly between 10 and 35 K [133], therefore if recombination is indeed encounter driven no significant temperature dependence should occur.

The build-up and decay of photoconductivity as a function of lamp power over four orders

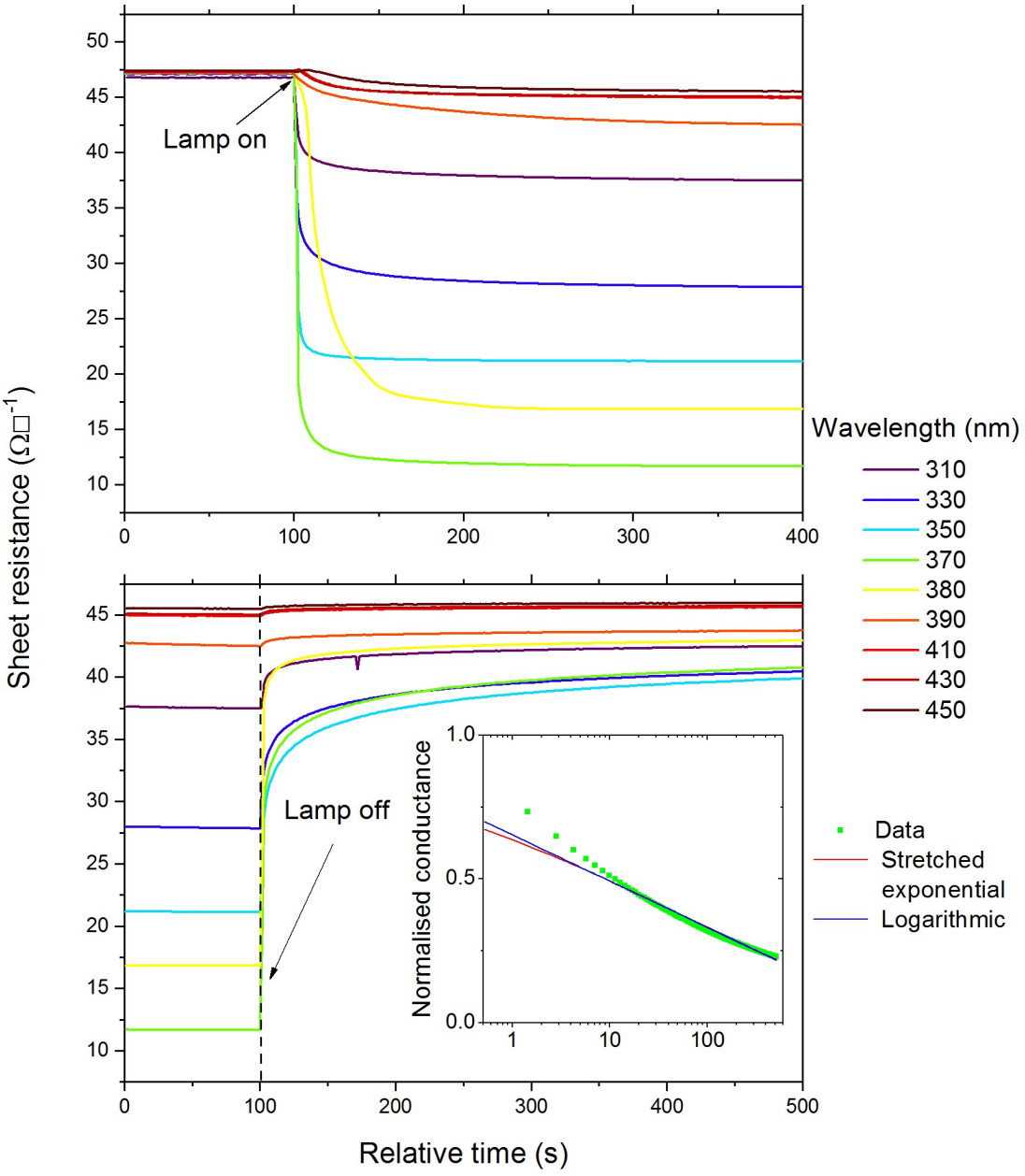

Figure 4.9: The build-up (top) and decay (bottom) of photoconductivity as a function of wavelength, using a lamp power of 50 μWcm^{-2} at $T = 10$ K. Examples of logarithmic and stretched exponential fits

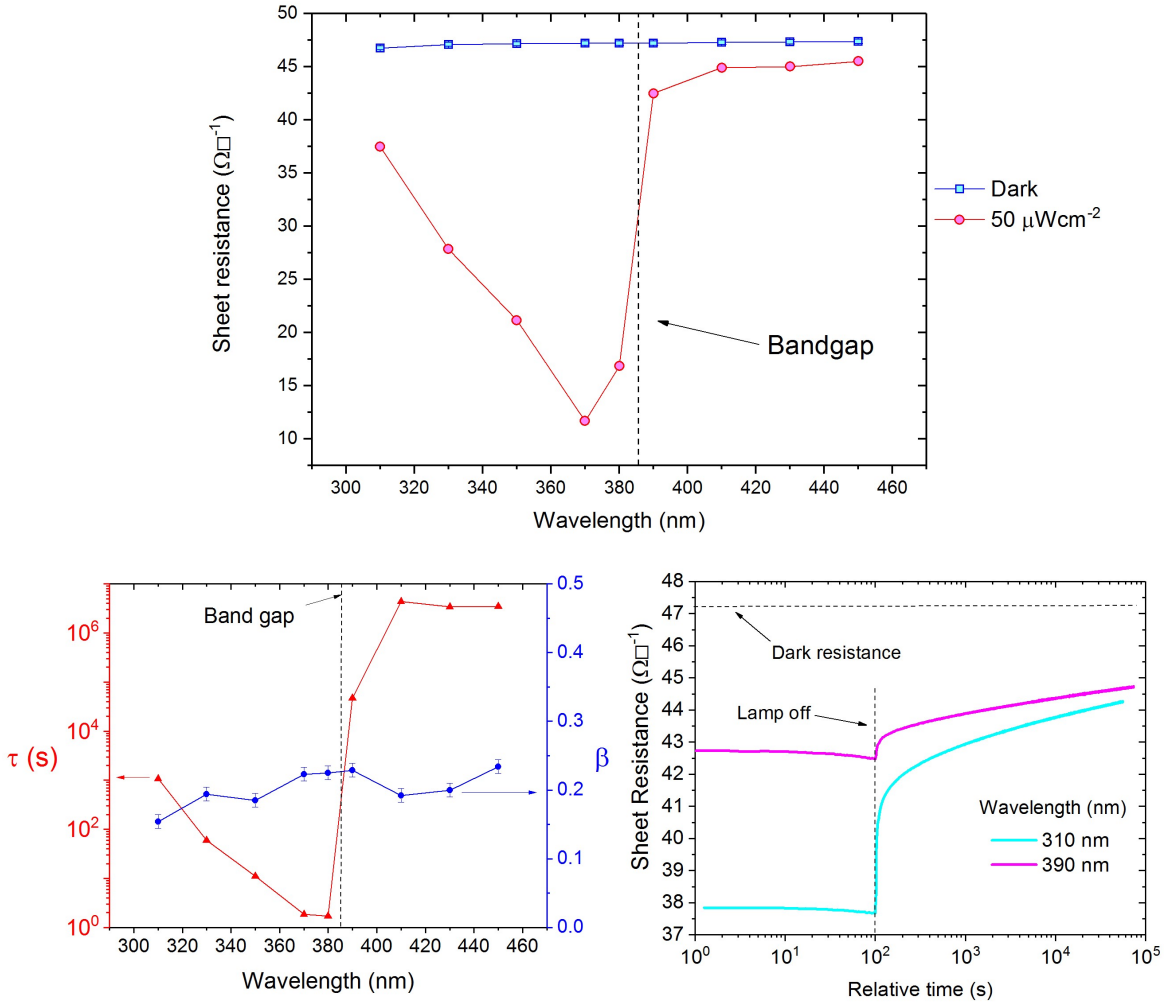

Figure 4.10: The spectral response after 300 seconds (top), fitting parameters from a stretched exponential fit(bottom left), and (bottom right) examples of two extended timescale decays, using a 50 μWcm^{-2} lamp power at $T = 10$ K.

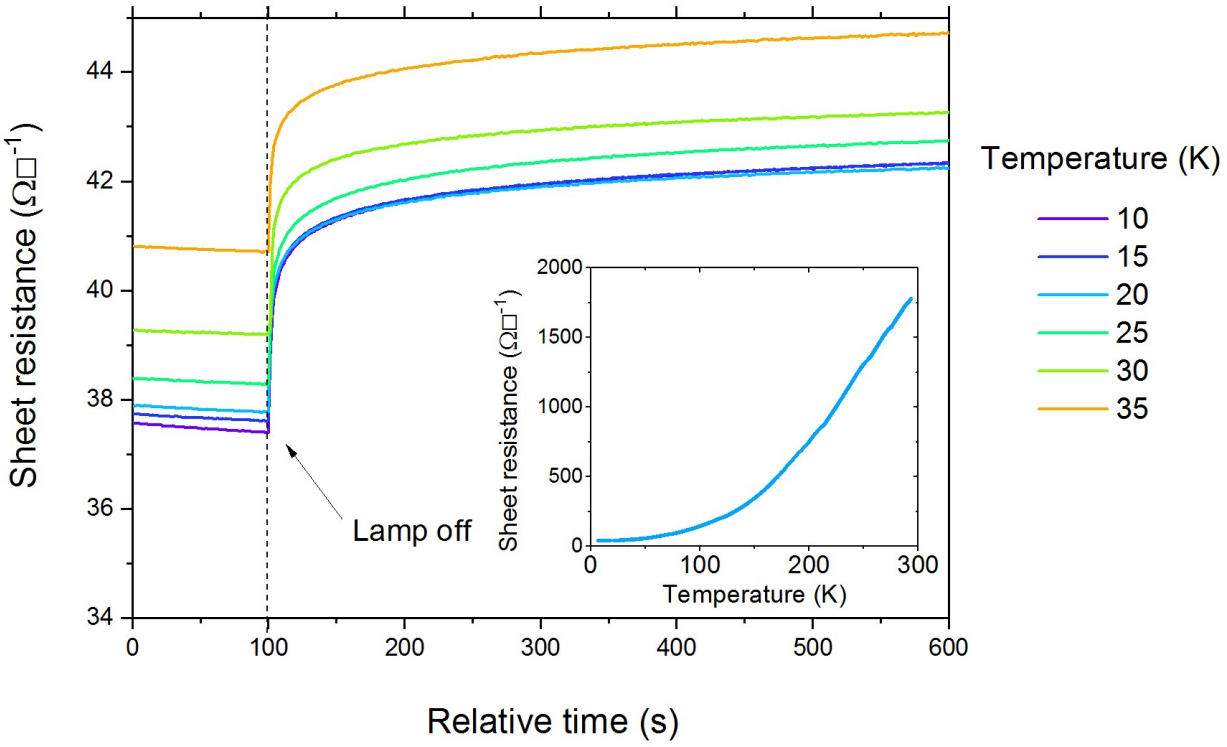

Figure 4.11: The decay of photoconductivity as a function of temperature and a dark $R(T)$ taken prior to any photoconductivity measurements (inset). A lamp power of 50 μWcm^{-2} and wavelength of 310 nm were used to illuminate the sample.

of magnitude is shown in figure 4.12. As the power is increased the initial rate of decay becomes larger, indicating that there are a greater number of un-trapped or separated carriers at higher powers, which recombine quickly. This is in contrast to persistent photoconductivity in nominally stoichiometric STO (see section 4.2.2) where the opposite dependence on power was observed. After the initially rapid decay the rate becomes similar for all powers. This is manifested in the fitting parameters (shown in figure 4.13) which show a large increases in lifetime as power is decreased and a smaller value for β for larger powers. The increase in carrier density as a function of generation rate is found to vary as $\Delta n \propto G^{0.3}$, a case of sublinear photoconductivity (shown in figure 4.13). This again indicates that the average carrier lifetime is larger at lower carrier densities.

The most striking feature of the build up of photoconductivity is that for the two lower powers there is an initial region of negative photoconductivity when the light it turned

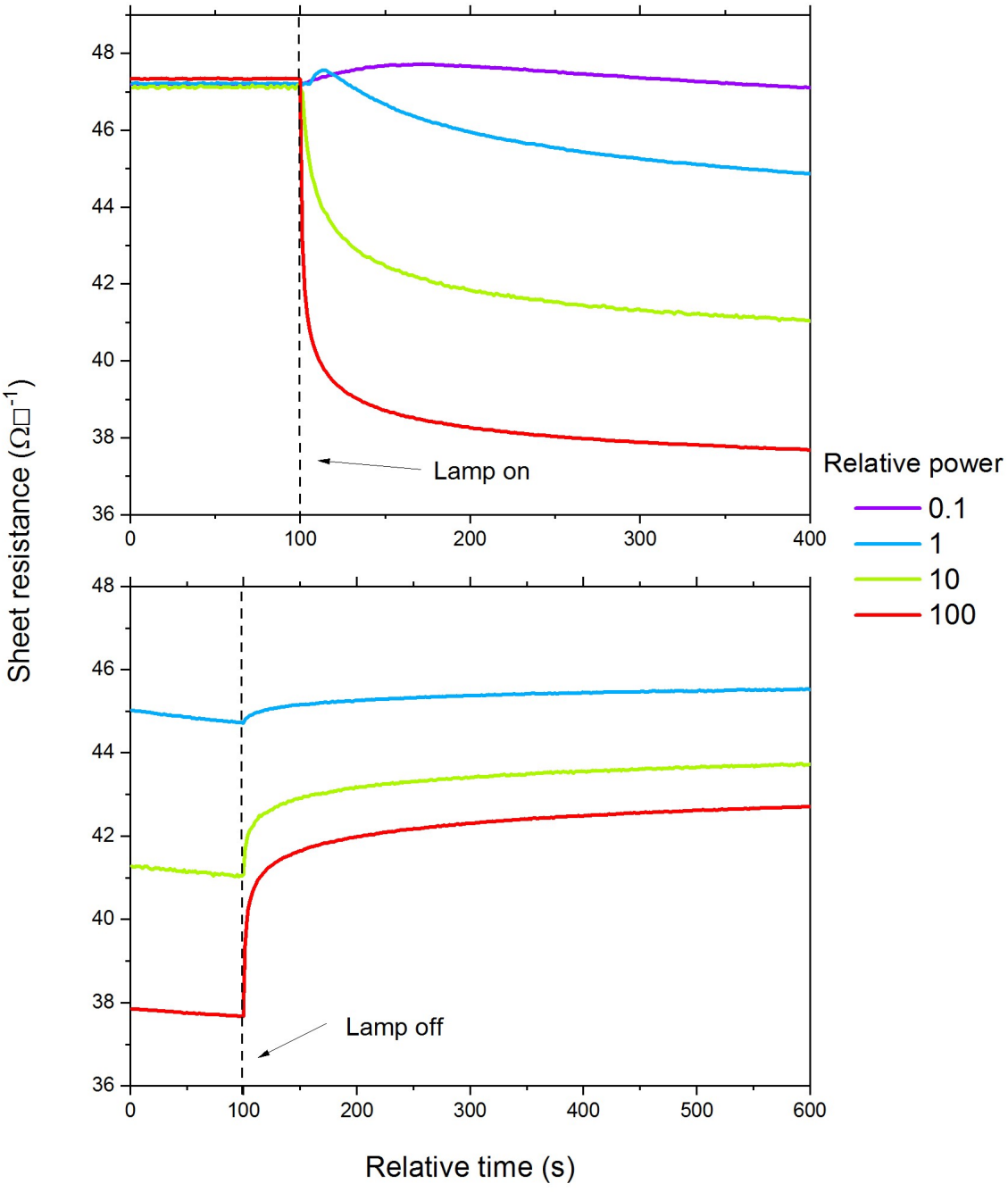

Figure 4.12: The build-up (top) and decay (bottom) of photoconductivity as a function of illumination intensity. A relative lamp power of 100 corresponds to 50 μWcm^{-2}. A wavelength of 310 nm was used and T =10 K.

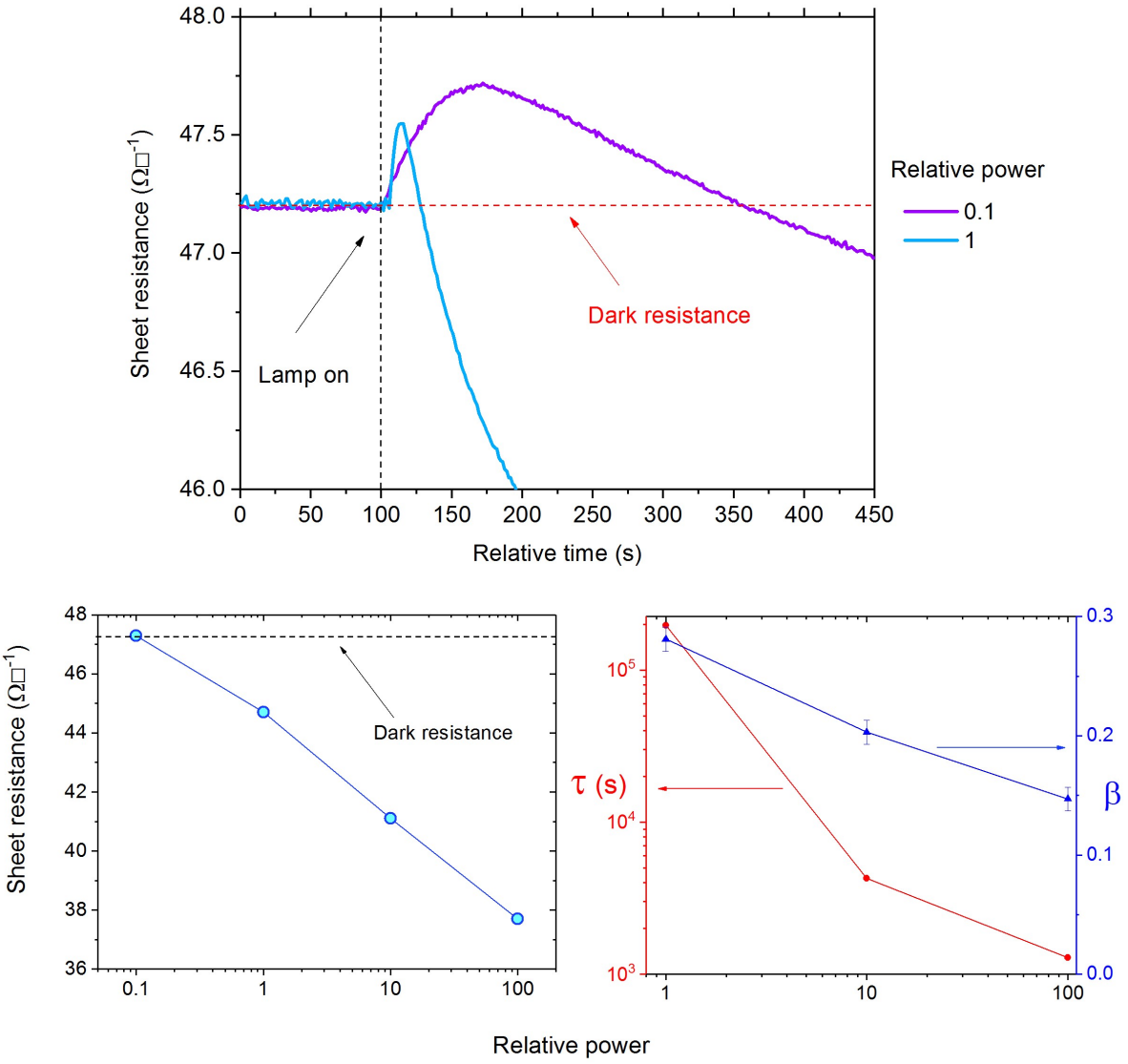

Figure 4.13: The region of negative photoconductivity observed at relative powers of 0.1 and 1 (top), the resistance after 300 seconds of illumination (bottom left), and fitting parameters from a stretched exponential function (bottom right), lines are a guide to the eye. A relative power of 100 corresponds to 50 μWcm^{-2}, all data was taken at $T = 10$ K.

on, this is shown in more detail in figure 4.13 (top). This transient negative photoconductivity lasts for ≈ 30 s and ≈ 255 s for relative powers of 1 and 0.1 respectively, before normal positive photoconductivity begins to dominate.

Negative photoconductivity can be described by a two center recombination model, with an unoccupied sensitizing level and an occupied recombination center. Firstly an electron is optically excited into the sensitizing level, leaving a hole in the valence band. This hole is subsequently captured by an efficient recombination center and recombines with an electron from the conduction band, reducing the carrier density. Finally the electron trapped in the sensitizing level is thermally excited into the conduction band restoring the dark conductivity, this is shown schematically in figure 4.14. Negative photoconductivity occurs provided that the rate of thermal excitation of an electron from the sensitizing level to the conduction band is smaller than the rate of capture of electrons by the recombination center. A further condition is that hole capture is more favorable by the recombination center than the sensitizing level $\beta_{p,S} < \beta_{p,R}$.

Previous works [101, 105], as well as the results in section 4.2.1, indicate that efficient recombination centers are the dominant channel of recombination in nominally stoichiometric STO, satisfying one of the requirements for negative photoconductivity. Photoluminescence spectroscopy measurements indicate that this recombination may be mediated by self-trapped electrons and holes. Sensitizing levels are also found in nominally stoichiometric STO, which were earlier attributed to strontium vacancies, however these have a much larger capture cross section for holes than electrons, and are located below the Fermi level, consequently they cannot be responsible for negative photoconductivity. Therefore the sensitizing level must have been induced by the Ar^+ irradiation.

In Ar^+ irradiated STO Kan *et al.* found a blue (2.8 eV) and green (2.4 eV) luminescence peak, attributed to the recombination of a free electron and self-trapped polaron, and an electron and hole via a self-trapped exciton, respectively. The blue luminescence was only observed in reduced STO samples (both thermally and by Ar^+ irradiation) leading the authors to suggest that the hole polaron was localised around an oxygen vacancy. Recent DFT calculations have indicated that the two electrons donated by oxygen vacancies play very different roles, one acting as a shallow donor and the other becoming trapped in a small polaron around the oxygen vacancy [125]. An oxygen vacancy level seems, therefore, a plausible candidate for the sensitizing level causing negative photoconductivity. Firstly, since one electron is donated to the conduction band there is an unoccupied state

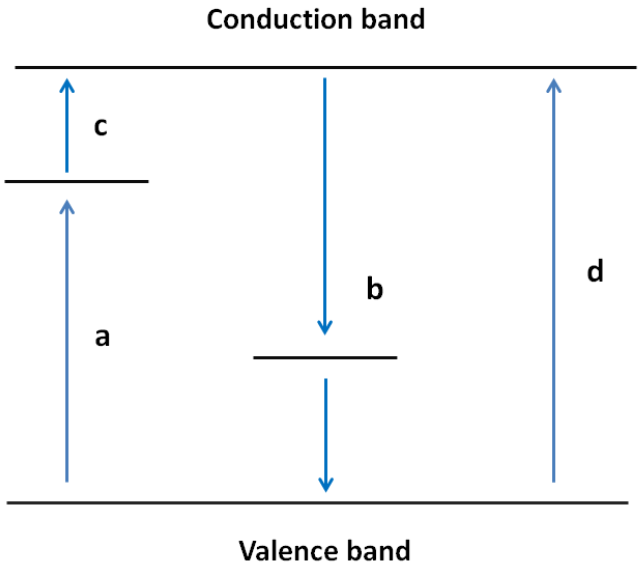

Figure 4.14: A schematic representation of the possible defect levels and transitions which lead to transient negative photoconductivity; a) an electron is optically excited into the sensitizing level, leaving a hole in the valence band, b) the hole is captured by an efficient recombination center and recombines with an electron from the conduction band, reducing the carrier density, and c) the electron trapped in the sensitizing level is thermally excited into the conduction band restoring the dark conductivity. Once all of the sensitizing levels are occupied by electrons or an equilibrium between optical and thermal excitation is reached process d) direct absorption begins to dominate and positive photoconductivity is recovered.

for a valence band electron to be excited into. Secondly since oxygen vacancies are either positively charged or neutral depending on whether they are singly or doubly occupied the condition $\beta_{p,S} < \beta_{p,R}$ should be easily satisfied.

The negative photoconductivity observed here is found to be largest, and persist for the longest, at lower rates of optical excitation. This indicates that there is a specific dose of illumination required to saturate the negative photoconductivity, corresponding to all sensitizing levels becoming occupied with electrons. Once this process is complete, normal band to band carrier generation would begin to dominate and photoconductivity would begin to increase. The location of the peak of negative photoconductivity occurs at a dose of $\approx 10^{14}$ photons cm^{-2}. Given that a sheet resistance of $\approx 50\ \Omega\square^{-1}$ is measured here, and assuming a mobility of $\approx 10^3$ cm^{-2}V^{-1}s^{-1} [133], the sheet carrier density in the dark corresponds to $\approx 10^{14}$ cm^{-2}, which is also the density of oxygen vacancies since each electron in the conduction band has been donated by a vacancy. Therefore the illu-

mination dose at which the onset of positive photoconductivity occurs is approximately the same as the number of oxygen vacancies.

4.4 Conclusion

In this chapter results have been presented for the equilibrium and transient photoconductivity in stoichiometric $SrTiO_3$ and $SrTiO_{3-\delta}$.

In nominally stoichiometric STO measurements of the temperature dependence of photoconductivity between 10 and 55 K reveal a large increase in photoconductivity at $\approx$ 35 K consistent with previous measurements by Kozuka [22] and Osawa [105]. The long photogenerated electron lifetimes have previous been attributed to a sensitizing level with a much larger capture cross section for holes than electrons, suppressing the recombination through an efficient recombination center. Measurements of photoconductivity as a function of photon flux yield a value of $\gamma = 0.94$ indicating that monomolecular recombination is dominant at $T = 10$ K and that the photocarrier lifetime is not dependent on the density of carriers. From this data an estimate of a the lower limit of the density sensitizing levels of 10^{18} cm^{-3} can be made, which is consistent with previous reports of the density of strontium vacancies [123]. These data offer further evidence that the long carrier lifetimes observed in STO at low temperatures are brought about by hole trapping at strontium vacancies.

Below $\approx$ 1 K persistent photoconductivity is found to emerge in nominally stoichiometric STO. The wavelength dependence of the persistence shows that it is a bulk phenomena and not caused by surface defects. The onset of persistent photoconductivity coincides with a large increase in the capture cross section of a charged defect, suggesting that hole trapping at strontium vacancies is again responsible for the long photogenerated electron lifetimes.

Finally the photoconductivity of Ar^+ irradiated STO, which creates an $\approx$ 20 nm of $SrTiO_{3-\delta}$, has been measured. Consistent with previous measurements of $SrTiO_{3-\delta}$ long lived persistent photoconductivity is observed [117, 119–121]. However transient negative photoconductivity has also been observed. The negative photoconductivity is found to persist until a specific dose of illumination has been reached, which coincides with the density of oxygen vacancies. The origin therefore appears to be the optical excitation

of an electron from the valence band into oxygen vacancy defect levels and subsequent capture of holes and conduction band electrons by an efficient recombination center.

Chapter 5

Optically Induced Persistent Photoconductivity

In this chapter results are presented for optically induced persistent photoconductivity in STO, motivated by previous work indicating that oxygen vacancies can be created by exposure to high intensity UV light. The photocarrier lifetime can be dramatically enhanced by prolonged UV exposure, leading to photoconductivity which persisted on the timescale of hours. A systematic study of this photoinduced state is presented here.

5.1 Background and motivation

STO based devices and heterostructure host a myriad of interesting physics [139, 140]. The most extensively studied of these is the (super)conducting two dimensional electron gas (2DEG) which can be formed at the LAO/STO interface [141–144]. However 2DEGs can also be formed in bare STO, for example by argon irradiation [133], electrolyte gating [145], delta doping [23], and simply by cleaving in vacuum [146]. Most recently Meevansana *et al.* [147] showed that through exposure to intense ultraviolet light provided by a synchrotron, a 2DEG can be created at the surface of cleaved (001) strontium titanate.

Prior to irradiation Meevansana *et al.* did not observe a 2DEG however they found that the carrier density could be tuned by progressively larger exposure doses of radiation until a 2DEG with a sheet carrier density as high as 8×10^{13} cm^{-2} was formed (shown in figure 5.1). The authors ruled out a surface reconstruction as there was no change in low energy electron diffraction pattern before and after exposure, and suggested there results were consistent with the creation of oxygen vacancies localised at the surface, which due to there positive charge, would cause an accumulation of electrons forming a 2DEG at the surface of the sample. However other in-gap states due to adsorbed impurity such as hydrogen could not be ruled out.

Subsequently it was shown by McKeown Walker *et al.* [148] that the induced 2DEG could be removed with atomic oxygen, supporting the hypothesis of oxygen desorption. Furthermore McKeown Walker *et al.* [149] proposed that the mechanism by which oxygen vacancies are created is Ti 3p core hole Auger decay. In this scenario the incident photons promote an deep electron into the conduction band leaving a Ti 3p core hole behind. The Ti 3p hole is filled with an electron from the neighboring O 2p orbital and two further Augur electrons are ejected, leaving the oxygen ion positively charged [150–152]. Finally the coulomb repulsion between the O^+ and Ti^{4+} ions causes the oxygen to be emitted from the surface. The threshold energy for this process to occur is 38 ev, and indeed McKeown Walker *et al.* showed that rate at which a 2DEG was induced was much larger for 53 eV photons compared with 26 eV. However a surface state was also induced at 26 eV albeit at a slower rate, suggesting a slower, lower energy process may also be occurring. Suwanwong *et al.* [153] found that the induced state was stable at much lower vacuums than previously investigated, showing slow recovery at oxygen partial pressures as high as 4×10^{-6} mbar. As well as this it was also shown by King *et al.* [154] that a 2DEG

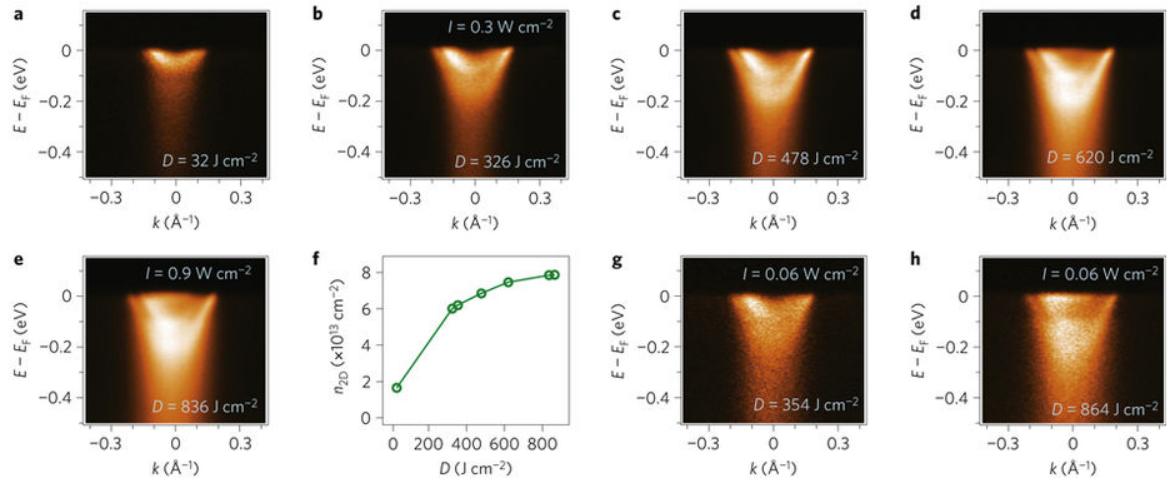

Figure 5.1: Emergence of a 2DEG with progressively larger doses of 55 eV synchrotron radiation (**a**-**e**) and sheet carrier density as a function of dose (**f**). **g** and **h** are at the same dose as **b** and **e** respectively but measured immediately afterwards with a lower intensity probing beam. Taken from Meevansana *et al.* [147].

can be similarly induced at the (100) surface of potassium tantalate again attributed to oxygen vacancies, suggesting the mechanism of defect creation may be applicable for other transition metal oxides.

The photoinduced creation of oxygen vacancies in these ARPES studies is consistent with results from photoluminescence spectroscopy [135]. Mochizuki *et al.* found that an in-gap state was induced by irradiation with a 325 nm laser when in vacuum. Introducing oxygen reversed this effect removing the in-gap state and return the sample to its original unirradiated form. The luminance from the induced in-gap state was consistent with that of reduced STO leading the authors to conclude that there were photoinduced oxygen vacancies. A particularly interesting implication of this work is that defect creation would seem to occur when STO is irradiated with much lower photon energies than those used in the ARPES measurements outlined above and in fact be accessible with a typical lab based source. This potentially provides an alternative route to creating defects at the surface of STO and other transition metal oxides, paving the way for continuously tunable and rewritable electronics. Therefore a more detailed understanding of this photoinduced state is important.

Photoconductivity has previously been used as a tool for studying and tuning the properties of LAO/STO interfaces [28, 155–159]. One of the most striking observations of these works is long lived persistent photoconductivity, which has been attributed to the spatial separation of electrons and holes by the potential well at the interface. In addition to this the lifetime of the persistent photocarriers has also been shown to increase when a larger density of oxygen vacancies are present in the STO substrate [160], or when palladium nanoparticles are evaporated onto the surface [161], suggesting that defects and surface adsorbates may also play an important role. Furthermore a number of previous works (including section 4.3 of this thesis) have observed persistent photoconductivity in STO itself when oxygen vacancies are present, both in bulk reduced [117,121] samples and thin films of oxygen vacancies produced by Ar^+ irradiation. Consequently if either oxygen vacancies, a potential well, or both can indeed be created at the surface of STO by intense UV exposure then this too would likely also to lead to persistent photoconductivity.

In this chapter measurements of both the equilibrium and persistent photoconductivity of STO after prolonged exposure to UV radiation (typically a dose of ≈ 100 Jcm^{-2}) are outlined, in order to gain a more detailed understanding of the formation and behaviour photoinduced defects. The results presented here show that long lived persistent photoconductivity can indeed be induced, indicative of the creation of a surface state similar to that previously observed by ARPES and photoluminescence measurements.

Samples of stoichiometric mixed termination (100) STO were first exposed to high intensity UV radiation (3 mWcm^{-2}) of extended periods of time (8-12 hours) to create a defect rich surface state. Broadband UV light (the spectrum is shown in figure 3.11) was typically used instead of the monochromatic UV used elsewhere in this thesis so as to maximise the exposure power, however despite this the surface dose in this work is much smaller than that of the ARPES experiments outline above. Consequently this exposure is not expected to create a sufficient number of defects to form a conducting 2DEG, however the lifetime of photoinduced carriers has been shown to be significantly increased by even low concentrations of oxygen vacancies or other defects [121]. Persistent photoconductivity can therefore be utilised as a particularly sensitive probe of the formation of defects. After the creation of a surface state the induced persistent photoconductivity as a function wavelength, power, illumination time and temperature was systematically measured using a lower power monochromatic probe light, similarly to in chapter 4, This procedure is shown schematically in figure 5.2.

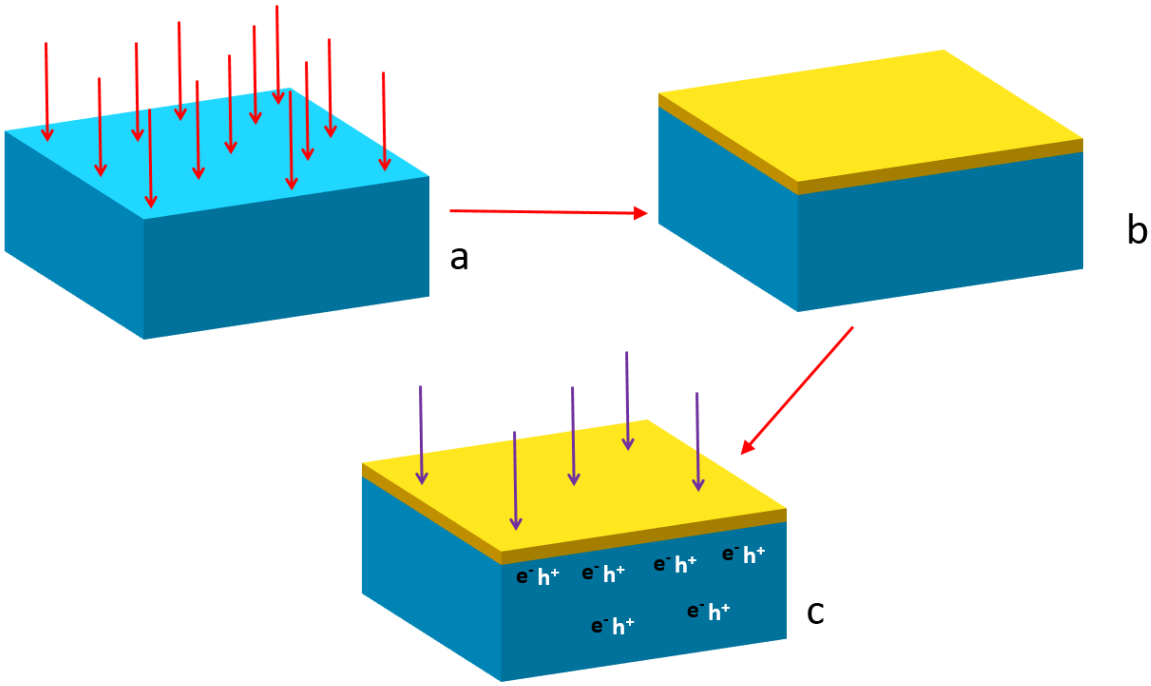

Figure 5.2: Schematic of the creation and subsequent probing of an induced surface state. **a)** Stoichiometric STO is exposed to high intensity broadband UV light, **b)** after extended exposure a surface state is created this state is permanent at low temperatures, **c)** the induced surface state is probed by photoconductivity with monochromatic illumination of various wavelengths and intensity.

5.2 Optically inducing persistent photoconductivity

To establish the relationship between UV exposure dose and photocarrier lifetime, nominally stoichiometric STO was exposed to 3 mWcm^{-2}, broadband UV light in 8 steps of $\approx$ 12 Jcm^{-2} (approximately 1 hour of exposure), leading to a cumulative dose of 98 Jcm^{-2} incident on the surface of the sample. After each step the sample was quenched with 2 mWcm^{-2} broadband IR light and left for 10 minutes to allow carriers created during the high intensity exposure to recombine, after this procedure the resistance of the sample was measured to verify that it was insulating (typically in excess of 10 M$\Omega\square^{-1}$) and that there was not a significant density of remaining photocarriers. The sample was then illuminated with 50 μWcm^{-2}, 310 nm light, at a temperature of 15 K for two minutes, after which the lamp was turned off, and the decay of photoconductivity measured.

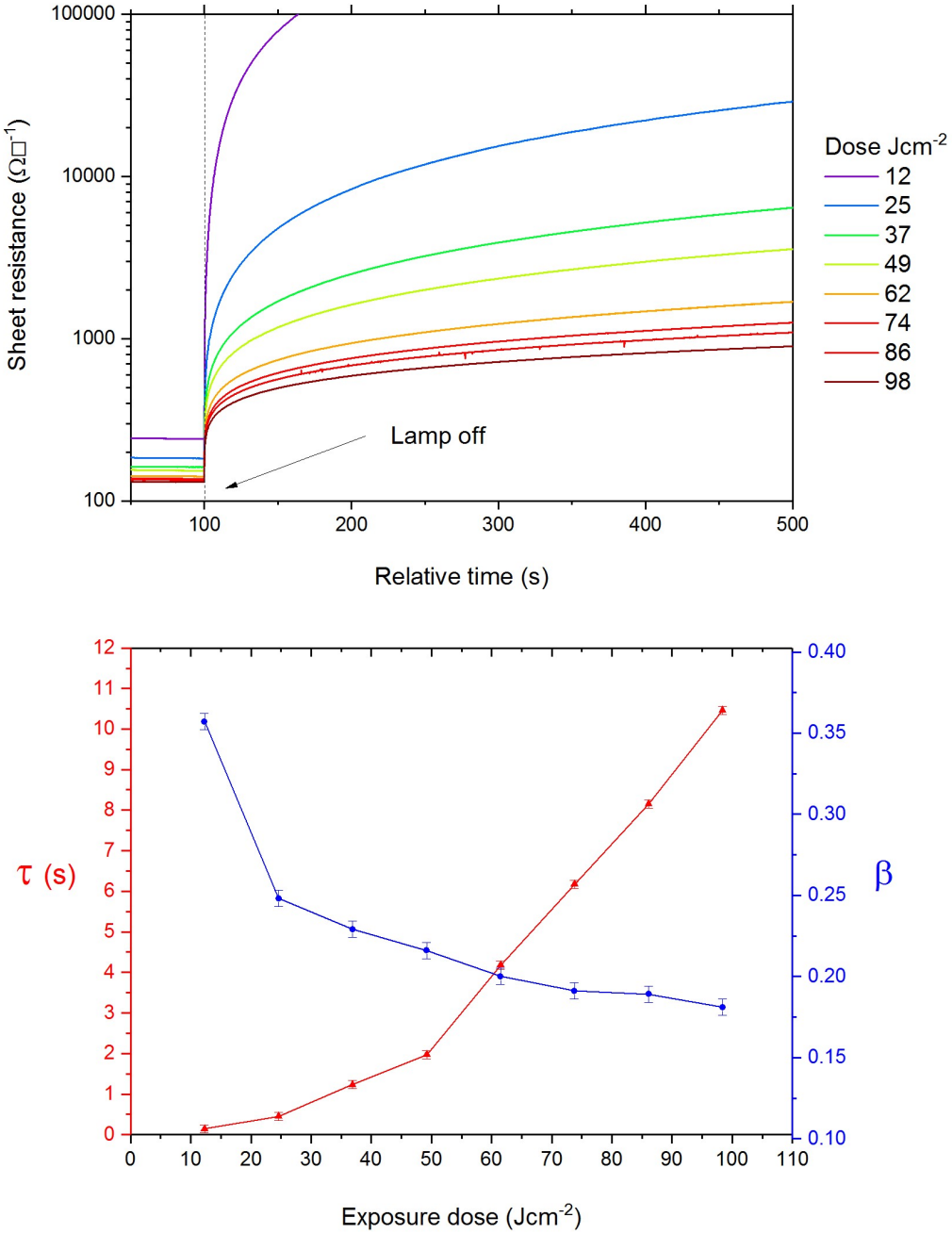

Figure 5.3: The exposure dose dependence of the decay of photoconductivity (top) and extracted parameters β and τ from a stretched exponential fit (bottom). The sample was exposed with broadband UV light, quenched with IR light for two minutes to remove photocarriers then probed with 310 nm light with a power of 50 μWcm^{-2} at $T = 15$ K.

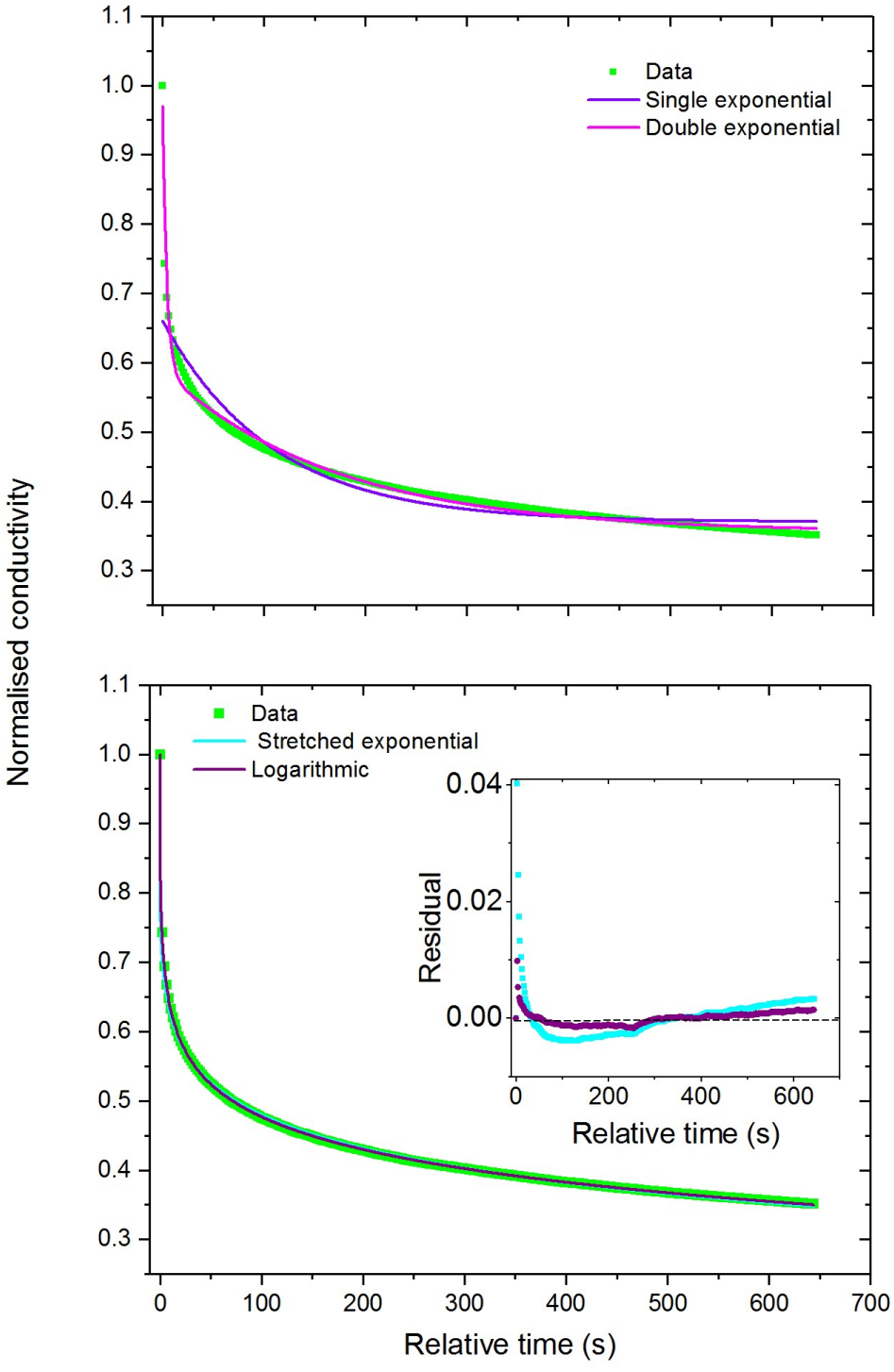

Figure 5.4: Examples of single and double exponential fits (top) and logarithmic and stretched exponential fits (bottom). The data was taken after the sample had been illuminated with 310 nm, 5 μWcm^{-2} light at $T = 10$ K.

The decay in photoconductivity as a function of exposure dose is shown in figure 5.3 (top). This data clearly shows that persistent photoconductivity can be controllably and progressively induced by high intensity UV exposure, even with photon energies of only $\approx$ 3-5 eV. After exposure photoconductivity is extremely long lived, at a dose of 98 Jcm^{-2} the sheet resistance is still less than 1 k$\Omega\square^{-1}$ almost 10 minutes after the shutter has been closed, in contrast to unexposed STO where sheet resistances in excess of M$\Omega\square^{-1}$ are reached in a mater of seconds in similar conditions (see figure 4.3 for example).

The dramatic enhancement in photocarrier lifetime is a clear indication of photoinduced defects, however it is not accompanied by any observable change to the dark conductivity, suggesting the density is much lower than achieved by synchrotron irradiation and is insufficient to bring about a metal insulator transition. Although the total dose after this period of exposure is of a similar magnitude to the previous ARPES studies described above, the average penetration depth of the broadband light is much larger and given the spectrum of the xenon lamp used here it can be estimated that less than 10 % of the total dose is absorbed within even the first 30 nm. It is reasonable to assume that the creation of the surface state depends on the dose of radiation within the first few nanometers of the surface rather than the dose received by the bulk, therefore the effective dose is much lower that the total 98 Jcm^{-2}.

In agreement with previous measurements of persistent photoconductivity in STO and LAO/STO heterostructures the decay of photoconductivity is well fitted to a stretched exponential function,

$$\frac{\sigma(t)}{\sigma(t=0)} = \exp\left(\left(-\frac{t}{\tau}\right)^{\beta}\right), \tag{5.1}$$

but not to single or double exponentials. This is often interpreted as a decay involving either a multi-step serial relaxation [50] or several parallel processes taking place simultaneously [51]. Good fits can also be made to a logarithmic decay,

$$\frac{\sigma(t)}{\sigma(t=0)} = 1 - \alpha \ln\left(\frac{t}{\tau_0} + 1\right). \tag{5.2}$$

This is has previously been associated with persistent photoconductivity due to charge separation in GaAs heterostructures [49].

Figure 5.4 shows examples of double and single exponential functions (top) and stretched

exponential and logarithmic functions (bottom), fitted to the decay in normalized photoconductivity after illumination with 310 nm, 5 μWcm^{-2} light at 10 K has ceased. It is clear that the latter two function are much better fits to the data that both single and double exponentials despite only having two fitting parameters, in contrast to the six of a double exponential. It is also worth noting that both logarithmic and stretched exponential fits have similar residuals (show in the inset of figure 5.4), underestimating the initial rapidity of the decay. Although the fit to a logarithmic decay is in fact slightly better, predominantly stretched exponential fits are used in this chapter so as to be consistent with previous studies of persistent photoconductivity in STO and LAO/STO heterostructures.

The lifetime τ and stretching parameter β extracted from stretched exponential fits are shown as a function of exposure dose in figure 5.3 (bottom). The lifetime grows from $\approx$ 0.2 seconds after a dose 12 Jcm^{-2} by around two orders of magnitude to $\approx$ 10 seconds after a dose 98 Jcm^{-2}. The increase in lifetime is accompanied by a reduction in the stretching parameter from about 0.35 to 0.17 indicating that the character of the decay is less exponential with increased dose. The reduction in the stretching parameter could indicate a broadening of the distribution of photoinduced in gap states as a function of dose [162]. However it should also be noted that in the case of the lowest exposure dose (12 Jcm^{-2}) the rapidity of the decay was such that the fit was made over a shorter range (70 s) that the subsequent doses (400 s), which has previously been shown to artificially increase the value of β (see section 2.1.4.2). It is possible that this may account of initially larger drop in β between 12 Jcm^{-2} and 25 Jcm^{-2}, however the remainder of the dose range would be unaffected. This range of values for the stretching parameter is also similar to those observed in nominally stoichiometric STO at less than 1 Kelvin and Ar^+ irradiated STO (see chapter 4), as well as the previous studies of persistent photoconductivity in STO and LAO/STO heterostructures.

5.3 Probing the optically induced state

In this section the optically induced state described in the previous section is studied, as a function wavelength, power, illumination time and temperature. For consistency these measurements were made on a single sample (with the exception of section 5.3.0.4 which used a different sample with the same exposure dose) after an exposure of 147 Jcm^{-2} (12 hours), however qualitatively similar results were obtained with both lower and higher exposure doses on different samples.

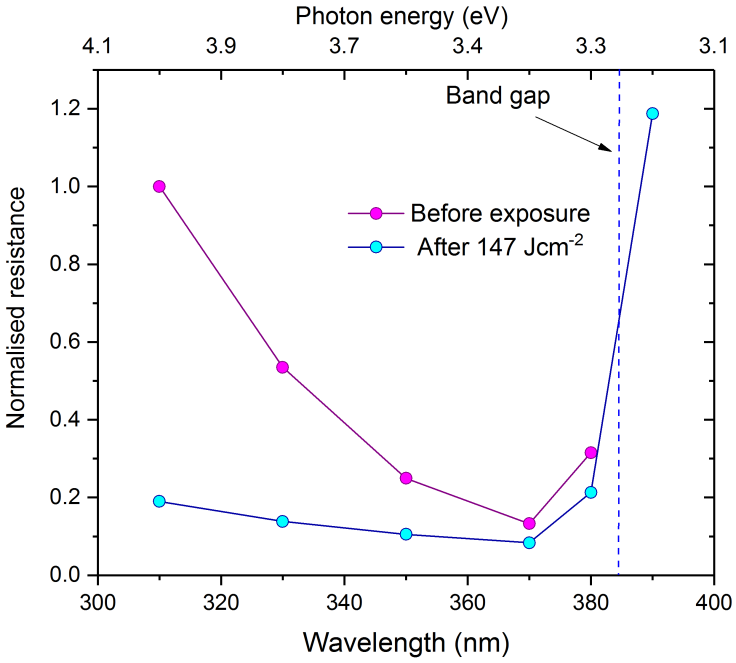

Figure 5.5: Normalised resistance as a function of wavelength between 310 and 390 nm before (purple) and after (blue) an exposure dose of 147 Jcm^{-2}. A lamp power of 50 μWcm^{-2} was used at $T = 10$ K.

5.3.1 Spectral response and wavelength dependence

The spectral response of photoconductivity at 10 K before and after 147 Jcm^{-2} (12 hours) of broadband UV exposure, is shown in figure 5.5 (normalised to the resistance at 310 nm before exposure). Before exposure a spectral response similar to that shown previously in section 4.1 is observed, however after the exposure two key changes to the spectrum occur. Firstly a measurable photoconductivity is observed when the sample is illuminated with sub band-gap energy photons, in contrast with the unexposed sample which shows a sharp cut off at the band gap. The broadening of the spectral response indicates that states within the band gap have been created by the UV exposure, allowing new optical transitions with lower that band gap energies to take place. These in-gap states have previously been shown to mediate the creation of free carriers by a two photon absorption process [134], leading to a sub-gap photocurrent. Secondly after exposure the resistance is found to be lower for all wavelengths used to illuminate the sample and that the increase in photoconductivity is largest at shorter wavelengths. Since the penetration depth of the light is smaller for shorter wavelengths this implies the enhancement in photoconductivity is largest near to the surface.

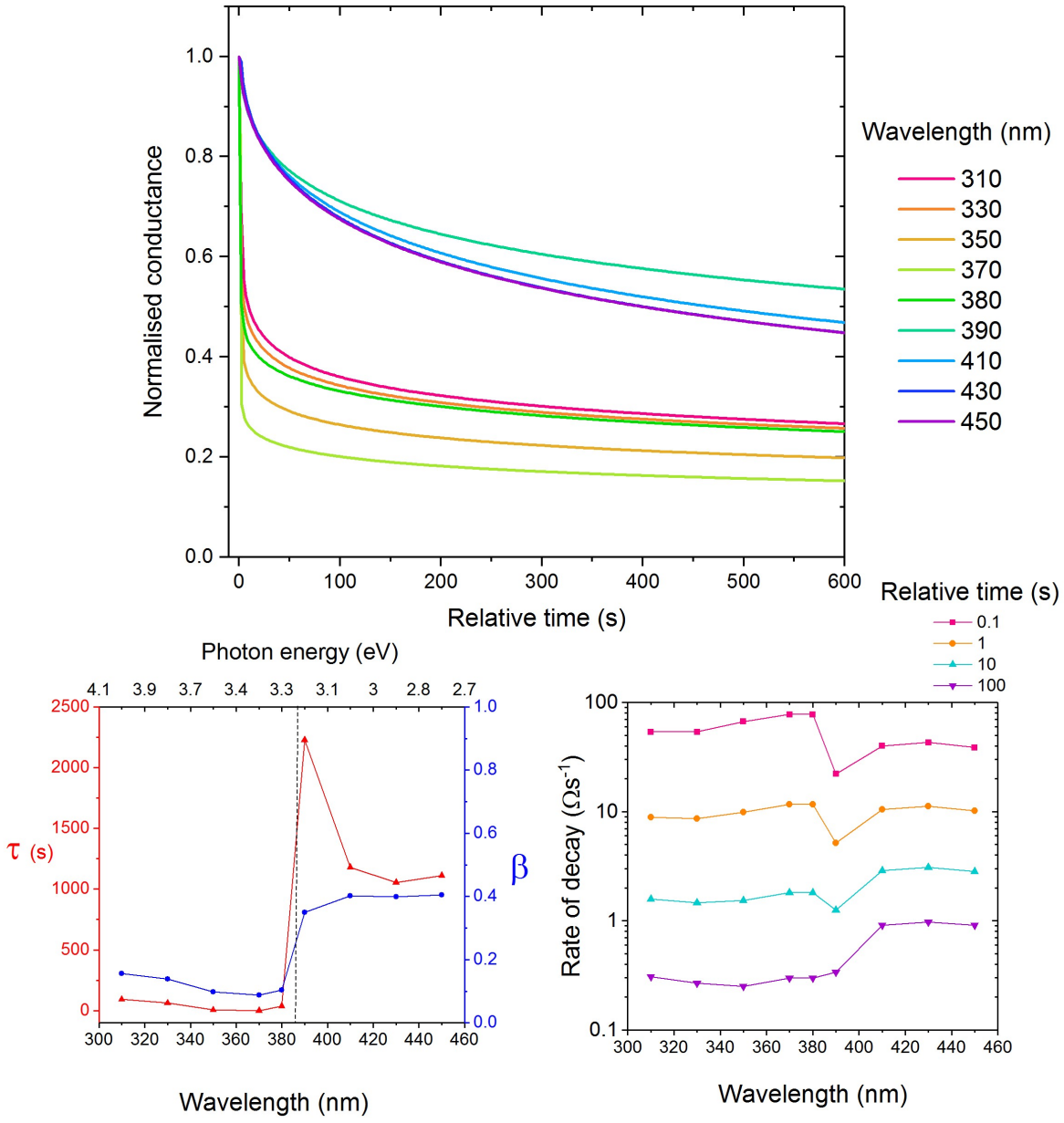

Figure 5.6: Normalised conductance as a function of wavelength between 310 and 450 nm (top), extracted parameters from a stretched exponential fit (bottom left), and the rate of decay after 0.1, 1, 10, and 100 s of the shutter closing. The sample was illuminated with a lamp power of 50 μWcm^{-2} at $T = 10$ K

To investigate this further the persistent photoconductivity as a function of wavelength was also measured by illuminating the samples for five minutes, then closing the shutter and measuring the decay in photoconductivity for ten minutes. Figure 5.6 (top) shows the normalised persistent photoconductivity as a function of wavelength, the extracted parameters from a stretched exponential fit (bottom left), and the calculated rate of decay (bottom right).

Firstly a clear separation of wavelengths above (310, 330, 350, 370 nm) and below (390, 410, 430, 450 nm) the band gap is observed in the normalised conductivity, the below band gap illumination leading to much longer lifetimes and a larger stretching parameter. In contrast above band-gap light shows a more rapid initial decay followed by much slower tail, i.e. a less exponential decay with a smaller stretching parameter. A similar relationship between λ, τ, and β was observed in the persistent photoconductivity in LAO/STO [156].

Within the above band gap light the lifetime is largest for 310 nm illumination ($\approx$ 100 s) and smallest for 370 nm ($\approx$ 0.5 s), both are much larger that the lifetimes of stoichiometric STO at this temperature (for example see figure 4.3), the trend of surface enhancement in lifetime is similar to that seen in the spectral response shown above. This change in lifetime is also accompanied by a reduction in the stretching parameter from 0.16 to 0.09, i.e. the decay is less exponential at 370 than 310. Consequently despite the dramatic difference in lifetime, the rate of decay is actually very similar on longer timescales, for example after 100 seconds the rate of decay is approximately 0.3 Ωs^{-1} for both wavelengths. This disparity between the rate of decay on shorter and longer timescales can be explained if the lifetime of carriers is dependent on the depth that they are generated within the sample. The initial behaviour of the decay is dominated by bulk carriers with short lifetimes recombining quickly, whereas the behaviour of the decay on long timescales is dominated by the surface where carriers have longer lifetimes (either because of minority carrier trapping localised to the surface or by charge separation due to a potential well at the surface). This scenario could explain the difference in initial decay rate and the similarly in longer timescale behavior of 310 and 370 nm light.

As well as comparatively longer lifetimes, the persistent photoconductivity of below band gap light also has much larger stretching parameters ($\approx$ 0.4 for 410, 430, and 450 nm) as a consequence of not showing the rapid initial decay seen in above band gap light. Instead

the rate of decay changes more slowly, crossing over from slower to faster than above band gap light after around 10 seconds of decay. Since below band-gap light does not have sufficient energy to promote electrons directly from the valance to the conduction band all of the carriers must be created via a defect level. The dependence of the equilibrium and persistence photoconductivity on wavelength discussed above indicates that these defects must be located close to the surface of the sample and therefore carriers generated by below band gap light must also be initially located near to the surface where the lifetime is largest. Furthermore the generation of carriers via a defect level is less efficient than band to band generation, leading to a smaller number of photocarriers which would also result in a longer lifetime (see section 5.3.2). The observation of photoconductivity at wavelengths as large as the 450 nm, the longest monochromatic light accessible by the xenon lamp used in this work, indicates that the induced defect state must be at least 0.5 eV within the bandgap.

5.3.2 Illumination time and power dependence

Persistent photoconductivity as a function of lamp power was measured by illuminating the sample with 310 nm light until the photoconductivity saturated, then closing the shutter and allowing the photoconductivity to decay for approximately ten minutes. The power was varied over four orders of magnitude from 0.1 % to 100 % of 50 μWCm^{-2}. Figure 5.7 shows the normalised persistent photoconductivity as a function of lamp power (top left), the rate of decay (bottom left), the extracted fitting parameters from a stretched exponential fit (top right), and the resistance as a function power after 60 seconds of illumination and after saturation (bottom right).

A striking feature of the persistent photoconductivity is a decrease in lifetime from approximately 4000 seconds at a relative power of 0.1 % to 150 seconds at a relative power of 100 %. The large decrease in lifetime is, however, accompanied by a substantial decrease in the stretching parameter from 0.29 at a relative power of 0.1 % to 0.15 at 100 %. Together these correspond to a more rapid initial decay for higher lamp powers but a similar rate of decay for all powers on longer timescales. Physically this could be attributed to a larger density of excess un-trapped carriers when the carrier generation rate is higher, due to saturating a finite density of traps. These excess carriers would have a much shorter lifetime than trapped carriers and decay quickly reducing the average lifetime at higher powers, however once they had recombined the rate would be determined by the recombination of trapped carriers and the lifetime would become larger.

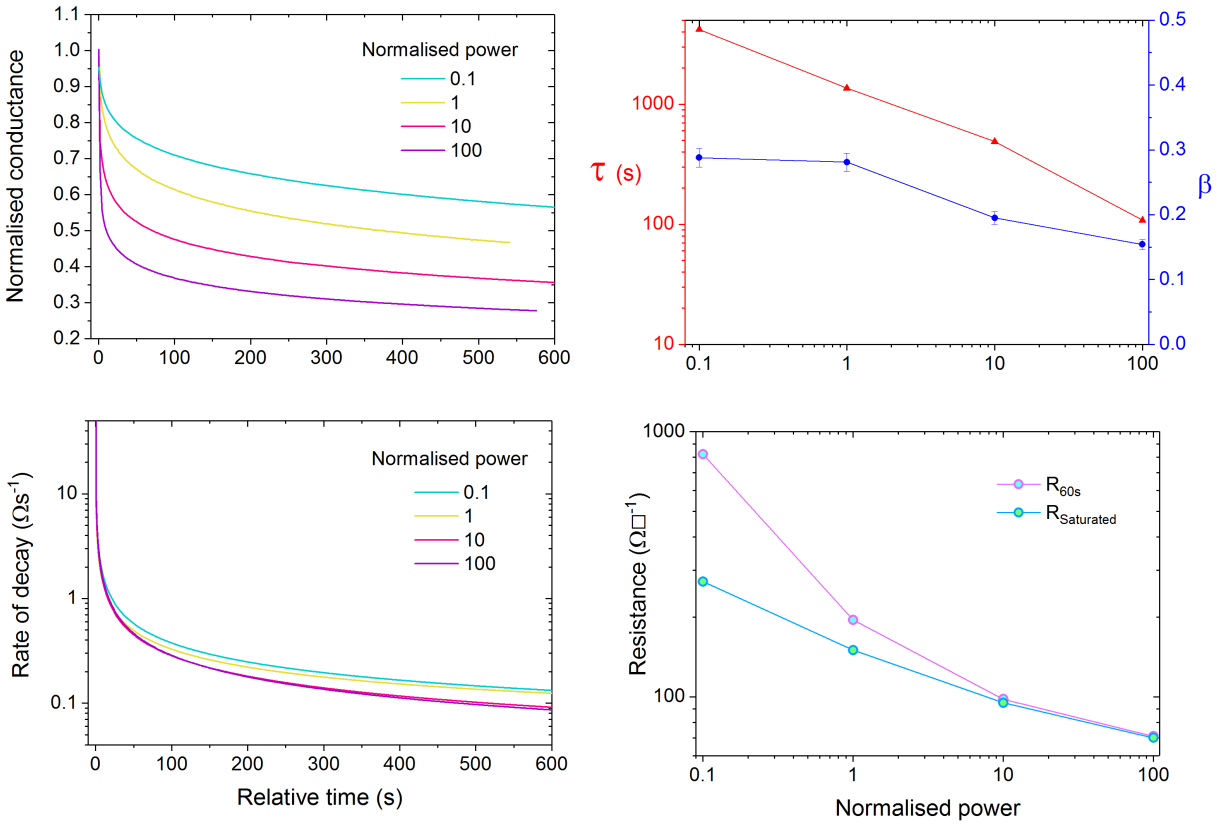

Figure 5.7: Normalised persistent photoconductivity as a function of lamp power (top left), extracted parameters from a stretched exponential fit (top right), the rate of decay (bottom left), and the resistance after 60 seconds of illumination (purple) and saturation (blue). A relative power of 100 corresponds to 50 $\mu W Cm^{-2}$, the wavelength used was 310 nm, $T = 10$ K.

Figure 5.7 (bottom right) shows the resistance as a function of relative power, measured after 60 seconds of illumination (purple) and after the saturation had been reached (blue). Firstly it can be seen that the two lower relative powers (0.1 % and 1 %) do not lead to a saturation in photoconductivity after 60 seconds, in fact at 0.1 % an illumination time of around one hour was required to saturate the photoconductivity. In nominally stoichiometric STO the photoconductivity was found to be approximately linear in generation rate (for example see figure 4.3), meaning that the lifetime was not dependent on the density of carriers. In contrast, after UV irradiation, the power dependence of resistance is much smaller, with the saturated photoconductivity varying by less than an order of magnitude over four orders of magnitude of power, again pointing towards a

density dependent lifetime.

The relationship between the build up and decay of photoconductivity, and the illumination dose was investigated further by systematically measuring persistent photoconductivity as a function of illumination time. Figure 5.8 (top) shows the build up of photoconductivity over approximately five minutes of illumination using a small normalised power of 1 % (grey line) and the decay of photoconductivity after the shutter has been open for varying intervals between 23 and 168 seconds.

The longer the sample is illuminated for, the larger the lifetime is found to be, varying from approximately 40 to 1200 seconds. However, in contrast to the two previous sets of results a significant change in the stretching parameter is not observed, initial falling from 0.31 to 0.28 between 23 and 115 seconds of illumination, consistent with a broadening of the distribution of occupied trap states, but remaining the same thereafter. Consequently the rate of decay is always higher on any timescale for shorter illumination times, an indication that fewer carriers are trapped (shown in figure 5.8, bottom left).

5.3.3 Temperature dependence

Persistent photoconductivity as a function of temperature was measured by illuminating the sample with 310 nm, 50 μWCm^{-2} light until the photoconductivity saturated, then closing the shutter and allowing it to relax for ten minutes, or for as long as possible for more rapid decays (i.e above 30 K). Figure 5.9 shows the build-up (top) and decay (bottom) of photoconductivity between 7.5 and 37.5 K. Figure 5.10 show the analysis of this data; the rate of decay as a function of time, the fitting parameters from a stretched exponential fit, the resistance as a function of temperature after 300 s of build-up, and an Arrhenius plot of the rate of decay.

It can be clearly observed that increasing the temperature suppresses persistent photoconductivity, the lifetime decreasing quickly from $\approx$ 850 s at 7.5 K to around than 1 s at 30 K. The functional form of this reduction in lifetime is approximately exponential in temperature, a best fit is shown in figure 5.10 (bottom left). Between 7.5 and 20 K the stretching parameter shows a small, approximately linear, increase from 0.2 to 0.24, followed by a peak in β, reaching 0.34 at 25 K before falling to 0.2 again at 30 K. This can

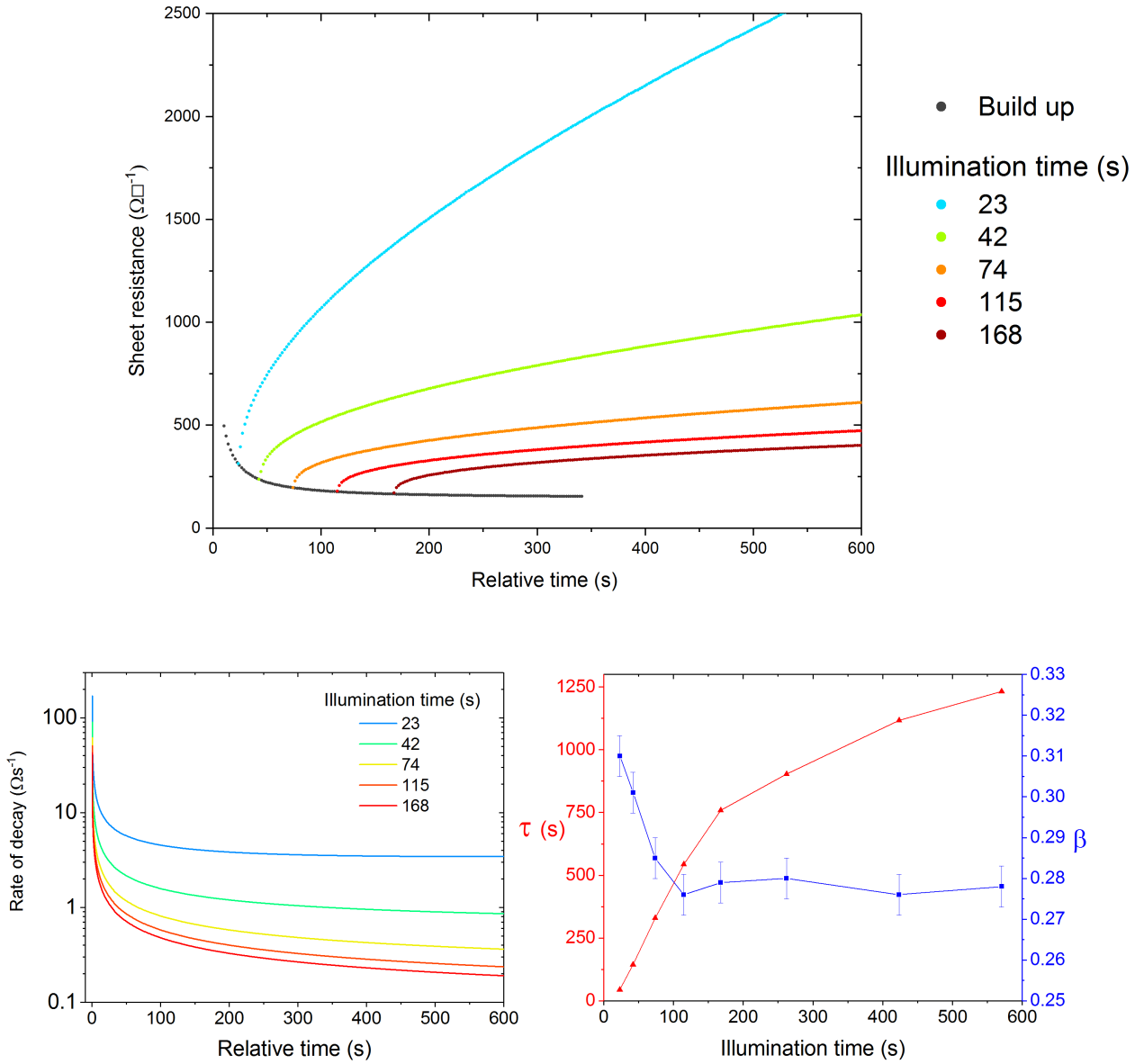

Figure 5.8: The build up (grey) and decay (rainbow) of photoconductivity as a function of illumination time (top), extracted parameters from a stretched exponential fit (top right), the rate of decay (bottom left). The sample was illuminated with a low power of 0.5 μWCm^{-2} to ensure a slow build up of photoconductivity, the wavelength used was 310 nm, at $T = 10$ K.

also been seen in the resistance curves, where the decay for 27.5 and 30 K show a more stretched decay, i.e. initially rapid followed by a much slower tail, as compared with the decay at 25 K. Indeed in the rate of decay (5.10 top left), there is a cross-over between 30, 27.5, and 25 K, the decay becoming faster for lower temperatures after around 200 s. Furthermore the build up of photoconductivity shows a similar small deviation from the typical behavior at both 27.5 and 30 K, where the resistance is initially higher and the build up rate is larger to compensate for this.

In a simple model of persistent photoconductivity where minority carriers are thermally freed from a single trap level, with negligible re-trapping the lifetime can be expressed as

$$\frac{1}{\tau} = N_c \beta_n \exp\left(-\frac{E_a}{k_b T}\right), \tag{5.3}$$

where N_c is the density of states in the conduction band, β_n is the electron capture coefficient, and E_a is the depth of the trap with respect to the valence band. Therefore the gradient of an Arrhenius plot of $\ln(\tau)$ against $\frac{1}{T}$ is equal to $\frac{E_a}{k_b}$, this is shown in figure 5.10 (top right). Perhaps unsurprisingly the straight line characteristic of Arrhenius-type thermal activated de-trapping from a single level is not observed, indicating that the decay originates from a more complex process than this .

Physically this corresponds to a slower than expected variation in lifetime as a function of temperature, $\tau \propto \exp(-T)$ instead of $\tau \propto \exp(\frac{1}{T})$. In some semiconductors the rate of recombination is also related to the mobility of the carriers, a larger mobility leading to more frequent encounters of electrons and holes and therefore quicker recombination [136, 137]. The rate is often described by the Langevin model [138]

$$R = k_L n p, \tag{5.4}$$

where n and p are the densities of electrons and holes respectively, and k_L is given by

$$k_L = \frac{e\mu}{\epsilon\epsilon_0} \tag{5.5}$$

where μ is the combined mobility of electrons and holes and ϵ is the dielectric constant. In STO the mobility of photogenerated electrons has previously been shown to be around 10 times higher at 7.5 K compared with 30 K [22], consequently this could lead to two competing effects on the lifetime as a function of temperature. Firstly thermal de-trapping of the minority carrier which increases as the temperature is raised, leading to quicker

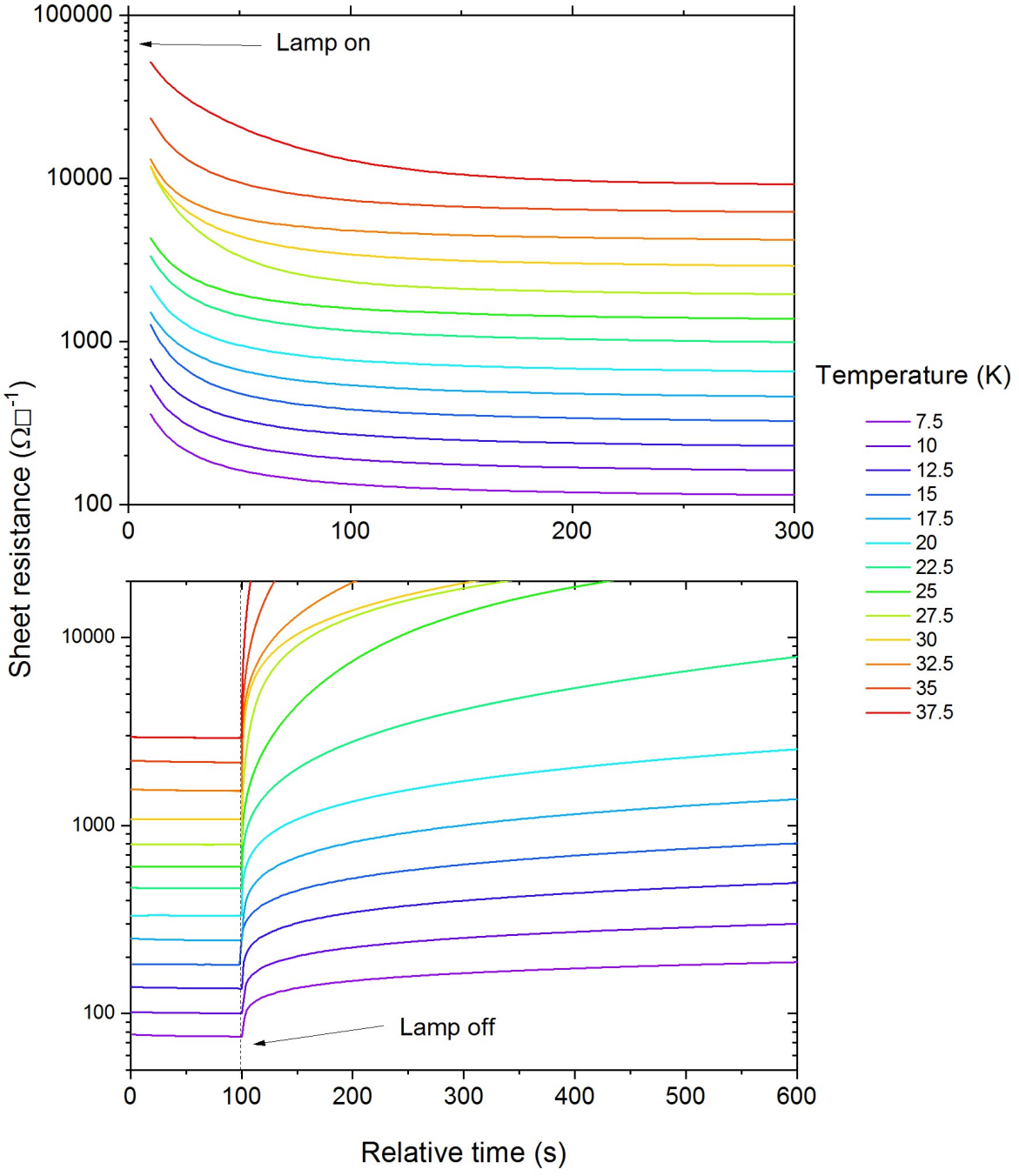

Figure 5.9: The build up of photoconductivity over five minutes (top) and the persistent photoconductivity (bottom) between 7.5 and 37.5 K. 310 nm, 50 μWCm^{-2} light was used to illuminate the sample.

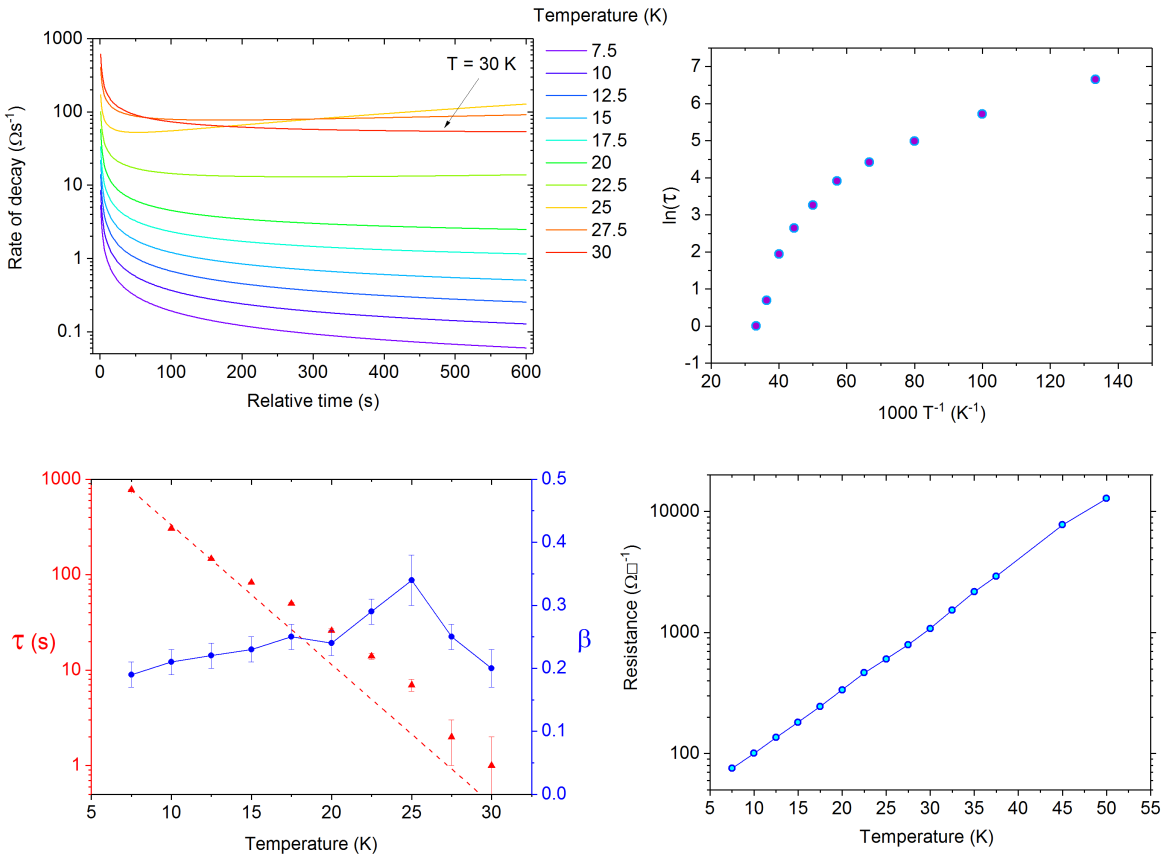

Figure 5.10: The rate of decay as a function of temperature (top left), extracted parameters from a stretched exponential fit (bottom left), an Arrhenius plot of $\ln(\tau)$ against $\frac{1}{T}$ using the lifetime from the fit (top right), and the resistance after five minutes of illumination (bottom right).

recombination. Secondly the mobility of photocarriers which decreases as the temperature is raised, leading to slower recombination.

Using data for the dielectric constant from muller *et al.* [128] and mobility from Kozuka [22] the Langevin recombination rate as a function of temperature was estimated. Due to the increase in the dielectric constant at lower temperatures, which increases the capture radius, the effect of a changing mobility is largely canceled out and adjusting the rate previously used in the Arrhenius plot to include the addition Langevin term does not make a significant difference to the functional form. It is therefore unlikely that the non-Arrhenius behavior is due to a change in mobility.

Another possible explanation of this behavior is that a range of activation energies exists

as apposed to detrapping from a single level. A non-Arrhenius temperature dependence of lifetime, with a functional form similar to that shown in figure 5.10 has previously been observed in LAO/STO heterostructures [157, 160], which was attributed to electrons escaping the interfacial potential well. Given the similarly of the data it is plausible that the same mechanism could responsible for the persistent photoconductivity shown here, with the potential well at the surface caused by positively charged defects, such as oxygen vacancies, or adsorbents.

Another key feature is the change in resistance as a function of temperature (5.10 bottom right), which increases exponentially. The photoconductivity is well fitted to the equation,

$$\ln(\rho) = -0.12T - 4.3. \tag{5.6}$$

Although an exponential temperature dependence has been previously measured at very low temperatures, both in this thesis and elsewhere [22] (see figure 4.2), a rapid increase in resistance centered at $\approx$ 35 K is also observed [105]. In chapter 4 this was attributed to an increase in the free electron lifetime, due to hole trapping by an sensitizing level, likely to be strontium vacancies. It has been suggested that above $\approx$ 35 K the sensitizing level is thermally quenched, ceasing to effectively trap holes [101, 105]. However a rapid increase in the rate of recombination is clearly absent in the temperature dependence of resistance present here after UV exposure, which remains exponential at least as high as 50 K. This implies that the sensitizing level is no longer the cause of long lived electrons after exposure.

5.3.4 Stability and reversibility

The longevity of the induced state was investigated by leaving the sample unilluminating between measurements for five days at approximately 5 K. Before and after this the persistent photoconductivity was measured by illuminating the sample with 310 nm, 50 μWCm^{-2} light at 10 K until the photoconductivity saturated, then closing the shutter and measuring the decay in conductivity, this is show in figure 5.11 (bottom). After five days with no illumination the equilibrium photoconductivity is $\approx$ 10 % smaller and the decay persistent photoconductivity faster, although both remain comparable to when measured immediately after exposure and long lived persistent photoconductivity is still observed. This indicates that, provided the sample is kept at low temperature and in vacuum, the rate of recovery of the sample to its original state is low.

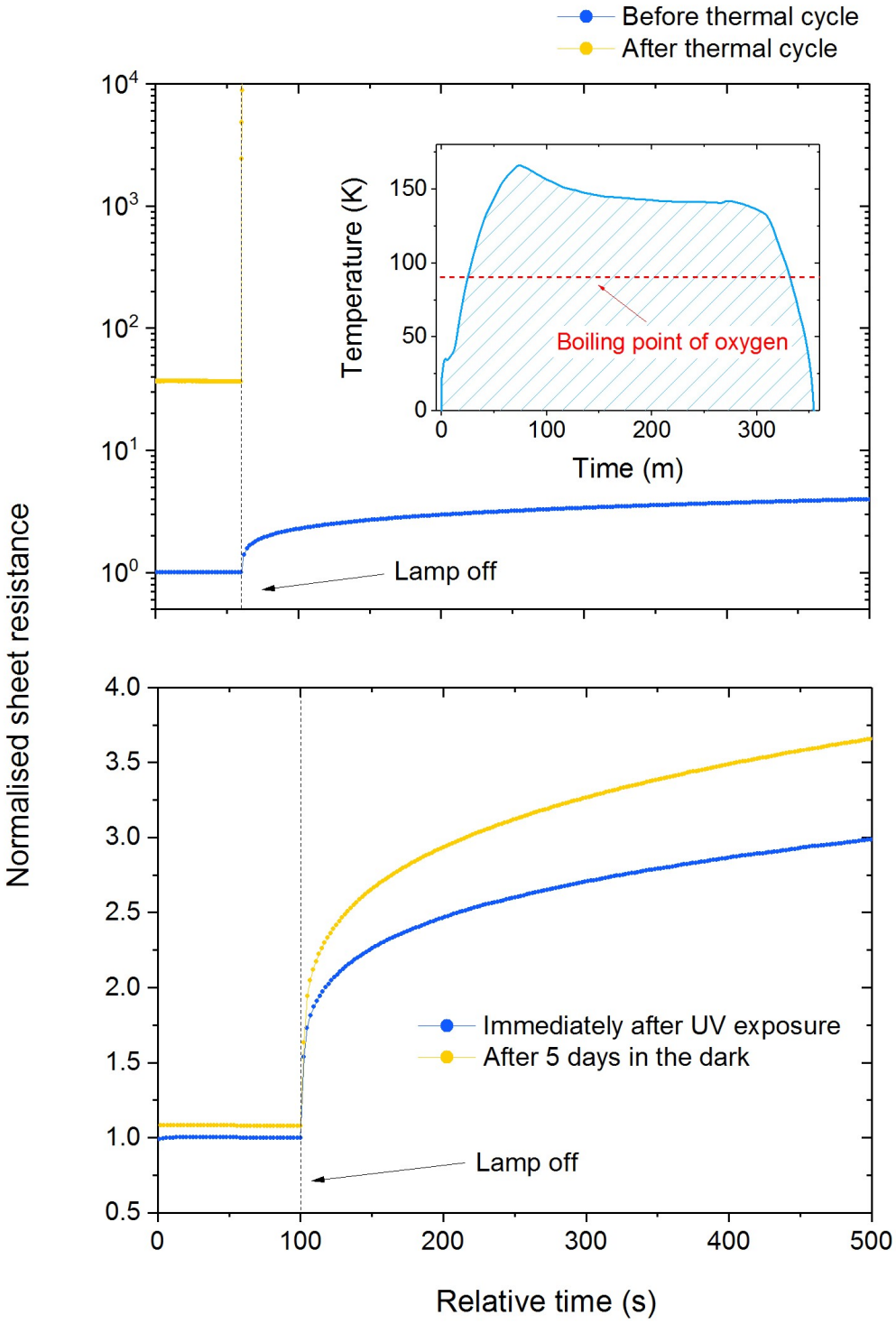

Figure 5.11: Persistent photoconductivity before (blue) and after (yellow) a thermal cycle to 150 K (top) and persistent photoconductivity before (blue) and after (yellow) five days in the dark at approximately 5 K (bottom). 310 nm, 50 μWCm^{-2} light was used to illuminate the samples at $T = 10$ K.

Following this the sample was thermally cycling to a maximum temperature of around 150 K for approximately five hours, the temperature profile of this is shown in the inset of figure 5.11(top). Again the persistent photoconductivity was measured before and after thermal cycling by illuminating the sample with 310 nm, 50 μWCm^{-2} light at 10 K until the photoconductivity saturated, then closing the shutter and measuring the decay in conductivity, this is show in figure 5.11 (top). The thermal cycle completely removes the induced persistence photoconductivity with the sample increasing in resistance to several M$\Omega\square^{-1}$ in only a few seconds, and the equilibrium photoconductivity returning to its original unexposed value.

Two potentially significant temperatures are crossed during this thermal cycle which may be related to the recovery of the sample to its original irradiated state, the boiling point of oxygen (90 K) and the cubic-tetragonal phase transition of STO (105 K) [6–8]. In the previous studies of UV induced defects in STO outlined in section 5.1, oxygen was found to reverse the effect of exposure, though to be due to oxygen filling vacancies which had been induced at the surface of the sample. When the temperature of the probe is increase above 90 K, oxygen which had previously been frozen onto the inside of the vacuum can becomes gaseous increasing the oxygen partial pressure and allowing it to recombine with vacancies in the sample. If the origin of persistent photoconductivity is indeed oxygen vacancies then raising the probe temperature above 90 K would lead to a refilling of vacancies restoring charge neutrality to the surface removing persistent photoconductivity. However along with increasing the partial pressure of oxygen thermally cycling to 150 K also causes the STO to pass through the cubic-tetragonal phase transition. Thermally cycling through this transition has previously been associated hysteric transport in STO [163] and LAO/STO [164, 165], though to be due to the reordering of oxygen vacancies around domain walls.

Due to the design of the probe used for this experiment favoring high cooling power temperatures in excess of $\approx$ 70 K could not be reached by heating the sample stage alone. Instead the whole probe had to be lifted inside the dewar so that it was no longer immersed in liquid helium. This method made precise control of the sample temperature difficult, meaning that the cubic-tetragonal phase transition and boiling point of oxygen could not be distinguished experimentally. However given the previous evidence for oxygen erasing the photoinduced state the softening of the cryogenic vacuum seems the more likely of the two possibility to be responsible for removing persistent photoconductivity.

5.4 Conclusion

The work presented in this chapter details the observation of optically induced persistent photoconductivity in STO, motivated by previous work indicating that oxygen vacancies can be created by exposure to high intensity UV light [135, 147, 148, 150, 153]. In this chapter broadband UV exposure has been shown to induce persistent photoconductivity, with the lifetime of the photocarriers increasing as the exposure dose is made progressively larger. The persistent photoconductivity can be completely removed by thermally cycling to 150 K suggestive that exposure to oxygen reverses the UV exposure.

The persistent photoconductivity is found to decay faster when longer, more deeply penetrating, wavelengths are used to probe the photoinduced state, compared with shorter, more surface sensitive, light. This is similar to the wavelength dependence observed in both Ar^+ irradiated STO and LAO/STO heterostructures [156], and indicates that the persistent photoconductivity occurs near to the surface, rather than in the bulk. A broadening of the spectral response is also observed with photoconductivity measured when illuminated with 450 nm light, meaning that optical transitions with at least 0.5 eV less energy than the band gap can occur, suggestive that an in-gap state has been created by UV exposure. This is again similar to the spectral response of Ar^+ irradiated STO and LAO/STO heterostructures [156], where the sub-gap photoresponse was attributed to a two photon absorption process via an oxygen vacancy defect level. The lifetime is also found to be dependent on temperature, the rate of decay being $\approx 10^3$ times larger at 30 K compared to 7.5 K. However it does not follow an Arrhenius-like temperature dependence, indicative of a range of activation energies rather than detrapping from a single level.

Collectively these results suggest that the origin of persistent photoconductivity is the spatial separation of electrons and holes by surface band bending due to a positively charged defect, shown schematically in figure 5.12. In the ARPES measurements outlined in section 5.1 oxygen vacancies were shown to be responsible for the band bending, however in this work the STO was exposed with much smaller photon energies of 3-5 eV, than previously used in ARPES measurements ($\approx$ 55 eV). The photons used in this experiment do not have sufficient energy to cause core hole Auger decay, which was shown to be the mechanism by which oxygen vacancies were created by McKeown Walker *et al.* [149]. However results from Mochizuki *et al.* [135] suggest that oxygen vacancies can

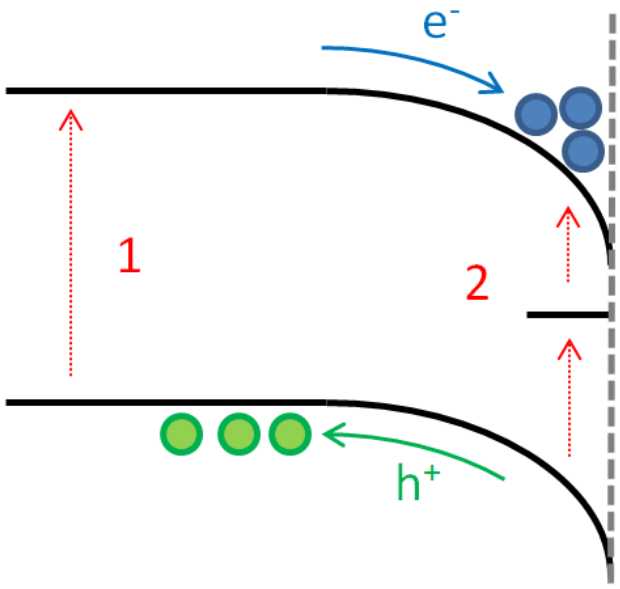

Figure 5.12: A schematic representation of photoinduced band bending leading to the spatial separation of electrons and holes. Optical transitions are represented by red arrows; transition 1 represents normal intrinsic adsorption in the bulk and transition 2 represents two photon adsorption via a defect level at the surface.

be formed by photon energies as low as 3.8 eV, furthermore the photodesorption of lattice oxygen by just above band-gap light has been has been reported in zinc oxide [166–168] and titanium oxide [169]. The photodesorption of surface absorbed molecular oxygen has also been reported to cause optically induced persistent photoconductivity in both of these materials [170–172], in these cases the mechanism of persistent photoconductivity is though to be the extraction of holes from the substrate by negatively charged adsorbed oxygen, which is subsequently freed from the surface. In air this results in an adjustment of the balance of absorption and desorption, however in vacuum the desorbed oxygen is pumped away and the decay in photoconductivity is negligible until air is reintroduced to the chamber [166]. However the situation is somewhat different in the UV exposed STO shown here, as the persistent photocarriers can be removed by both optical and thermal quenching without removing the optically induced defects themselves (which require higher temperature thermal cycling to remove).

Given the similarity of the results presented in this chapter to the persistent photoconductivity of Ar^+ irradiated STO (see chapter 4) and to LAO/STO heterostructure were oxygen vacancies have been deliberately introduced [160], it seems most likely that the de-

fects are oxygen vacancies. Other effects such as photo-catalytic water splitting [173,174] producing positively charge hydrogen at the surface [175], similar to the so called water cycle mechanism proposed by Bi *et al.* [176] to explain the induced conductivity by conducting AFM writing at LAO/STO interfaces [177], cannot however be ruled out.

Chapter 6

Optically Tunable Superconducting Devices

In this chapter results are presented for optically tunable superconducting-semiconducting hybrid devices. Junctions are composed of superconducting niobium and a photosensitive strontium titanate gap, with and without a metallic interlayer. Although no devices become fully superconducting a potential future route to realising optically tunable superconducting-semiconducting hybrid Josephson junctions is discussed.

6.1 Background and motivation

6.1.1 Superconducting-semiconducting Josephson junctions

Superconducting-Semiconducting hybrid Josephson junctions (S/Sm/S) host a myriad of interesting behaviour and may prove practically useful for there potential application in quantum computing [178] and opto-electronic devices, for a recent review see [179]. There are several examples of S/Sm/S Josephson junctions based around semiconductors such as Ge/Si nanowires [180], GaAs [181], and possibly the most extensively studied InAs [182–188]. Recently there has been significant interest in both InSb and InAs nanowire junctions as a growing body of evidence suggests they may host Majorana fermions [189–196]. For example, Rokhinson *et al.* [197] observed a doubling of the Shapiro step size in InSb nanowire Josephson junctions when a magnetic field was applied in the plane of the nanowire to break the degeneracy between up and down spins. This change in the periodicity of to the Josephson equation (equation 2.39) from 2π to 4π is a key experimental signature of Majorana fermions [198].

Typically the carrier density of the semiconductor in S/Sm/S junctions can be tuned with a gate voltage [199, 200], however as early as 1968 Giaever [201] showed that it was also possible to tune devices optically. He measured Pb/CdS/Pb devices which did not show any supercurrent in the dark but found that it was possible to turn the Josephson effect on by exposure to light, indicating that the coupling between the superconductors could be enhanced when illuminated. Shortly after this Andreozzi [202] *et al.* also found an optically tunable supercurrent in In/CdS/In junctions. Later in indium doped PbSnTe devices with Pb/In superconducting electrodes Takaoka *et al.* [203] showed that the origin of the optical tuneability was both an increase in the normal state coherence length ξ_N due to an increased carrier density and a reduction in the interface barrier increasing the probability of Andreev reflection, with increasing illumination intensity. In probably the most comprehensive investigation of optical tuning Schäpers *et al.* [204] measured Josephson junctions fabricated from Nb electrodes and an InGaAs 2DEG. They found that the critical current of the junctions could be increased by as much as 25 % by exposure to light accompanied by a reduction of the normal state resistance of the junction due to photocarriers. Also investigating Nb/InGaAs/Nb junctions Akazaki *et al.* [205] found that when illuminated with longer wavelength light negative photoconductivity (a reduction in carrier density, for example see section 4.3) was observed. However despite reducing the carrier density of the bare 2DEG by $\approx$ 20 % they found that the

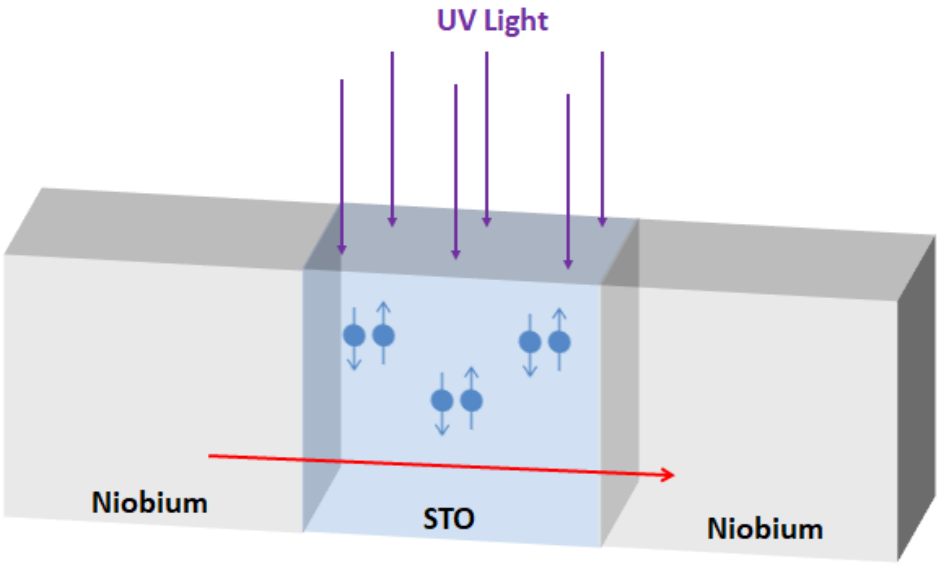

Figure 6.1: A schematic of the Nb/STO/Nb photo-tunable junctions, the current is indicated by the red arrow.

junction resistance was decreased and that the interface transparency was larger. This suggests that the effects of increasing the coherence length and decreasing the interface barrier can be tuned separately by wavelength dependent measurements. More recently Tsumura and coworkers have realized optically tunable semiconducting Josephson junctions in GaAs/AlGaAs 2DEGs [206,207] and in monolayer graphene [208]. Optical tuning of the coupling between two superconductors separated by a photosensitivity semiconducting layer, can be done continuously, reversibly, and in real time, and is therefore an attractive alternative to conventional tuning, such as changing the electrode spacing, in both single junctions and Josephson junction arrays [209–213].

6.1.2 This work

The strong photoconducting response in STO at low temperature makes it an excellent candidate for the photosensitive element of optically tunable S/Sm/S Josephson junctions, potentially with an unprecedented degree of optically tuneability. However examples of STO based Josephson junctions are rare and have only been realized in all oxide devices where STO forms both the superconductor and insulating barrier, by modulating

the carrier density with a gate voltage [214]. Even without optical tuning therefore, this field remains in its infancy.

The broad aim of this work is to make the first steps in achieving highly optically tunable STO based Josephson junctions, by fabricating niobium (Nb) superconducting electrodes separated by a small STO barrier, this is shown schematically in figure 6.1. By varying the intensity and wavelength of illumination the carrier density and thickness of the sheet of electrons coupling the two superconductors can be continuously tuned. The semiconducting band gap of STO is, of course, much larger than the superconducting gap of Nb, in fact by a factor of ≈ 1000. Consequently any light which can generate carriers in the STO will also create excited single particle states in the Nb, suppressing superconductivity. Results present here show that the suppression of T_c is small even at relatively high intensities, and therefore is not prohibitive.

In this chapter representative data from several types of devices based around superconducting Nb and photo-tunable STO are presented. Firstly the simplest Nb/STO/Nb devices, then devices with a metallic interlayer, namely aluminum and titanium (Nb/Al/STO/Al/Nb, Nb/Ti/STO/Ti/Nb).

6.1.3 Summary of fabrication methods and measurements

A detailed description of the fabrication of devices is given in section 3.1, however a brief summary for the particular devices featured in this chapter is given here.

The niobium films used to fabricate these devices were grown by Angelo di Bernardo at the department of material science and metallurgy, Cambridge university. The 7.5 nm transparent niobium shown in section 6.4 was grown by Daniel Chaney in the physics department, Bristol university. The first set of junctions (section 6.2) were made by optical lithography and reactive ion etching for the large features and focused ion beam etching for the gaps. The remaining devices were fabricated in a one step electron beam lithography procedure using ma-N resist and reactive ion etching.

6.2 Nb/STO/Nb planar junctions

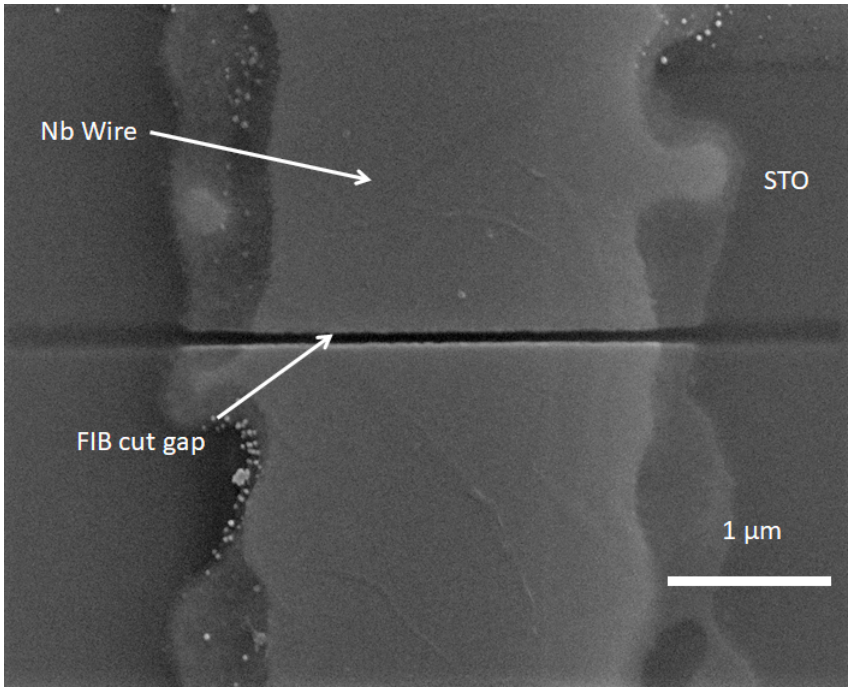

Figure 6.2: An SEM image of the device measured in this section, a characteristic meander in the wire due to diffraction during optical lithography can be seen.

In this section results are presented for a Nb/STO/Nb junction fabricated by optical lithography (the mask design is shown in figure 3.7) and focused ion beam etching, an SEM image of the device is shown in figure 6.2. The results shown here are for the smallest gap that was achieved $\approx$ 60 nm, however qualitative similar results were found for larger gaps, across different samples.

$R(T)$ curves as a function of power using 310 nm light (top) and wavelength at a power of $\approx 50\ \mu\mathrm{Wcm}^{-2}$ (bottom) between 4 and 12 K, are shown in figure 6.3. A superconducting transition of the Nb electrodes occurs at a critical temperature of $\approx$ 8 K, which is not suppressed substantially even by high powers ($\approx 50\ \mu\mathrm{Wcm}^{-2}$) of illumination. However the device does not become fully superconducting for any combination of power and wavelength. The most striking feature of this data is the unusual shape of the superconducting transition, which shows a peak in resistance at the T_c of the Nb electrodes and, for powers exceeding $\approx 6\ \mu\mathrm{Wcm}^{-2}$ *negative* resistance when the Nb electrodes are in the normal state.

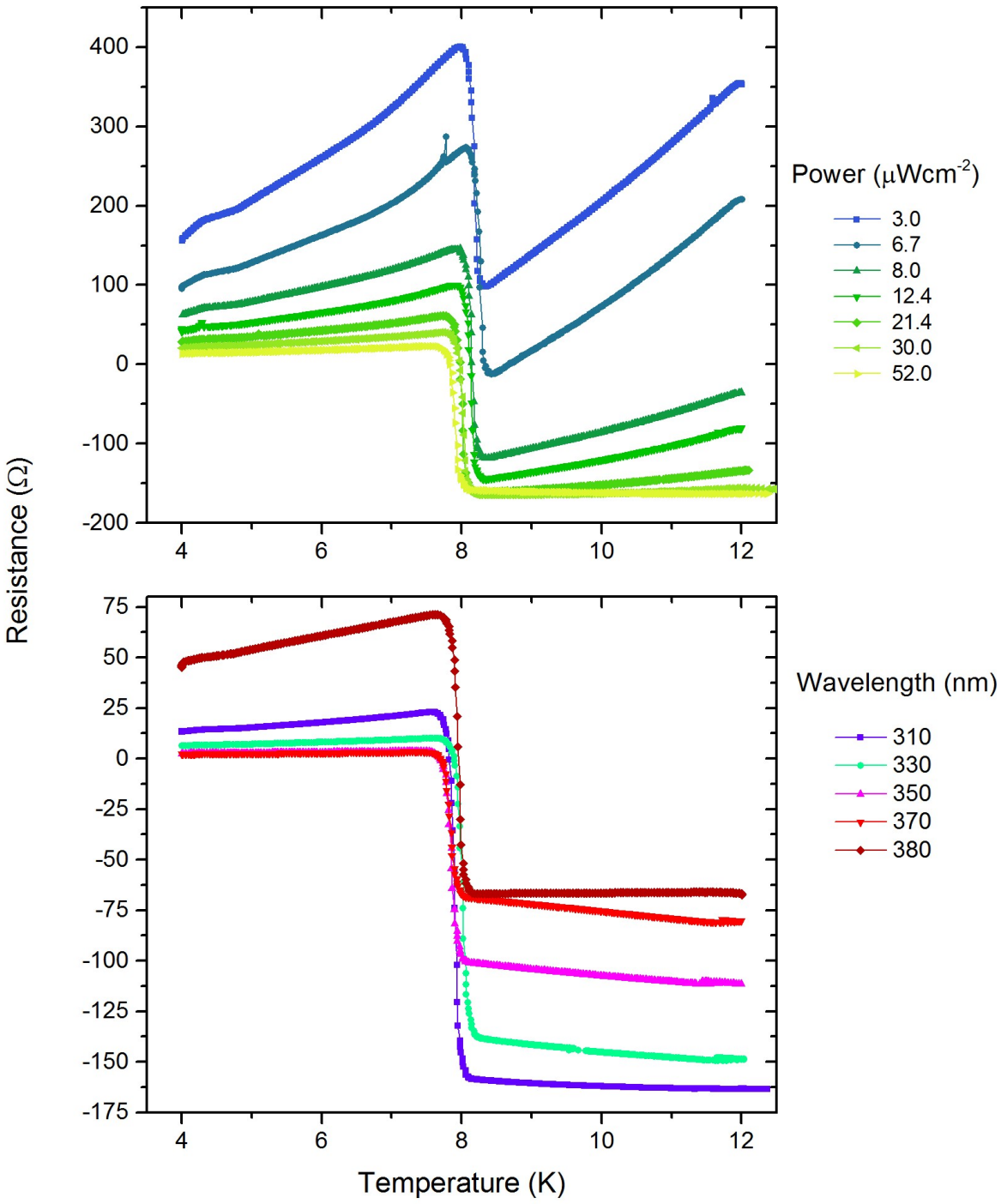

Figure 6.3: $R(T)$s for a 60 by 2000 nm STO gap as a function of power (top) using 310 nm light and wavelength using a power of 50 μWcm^{-2} (bottom).

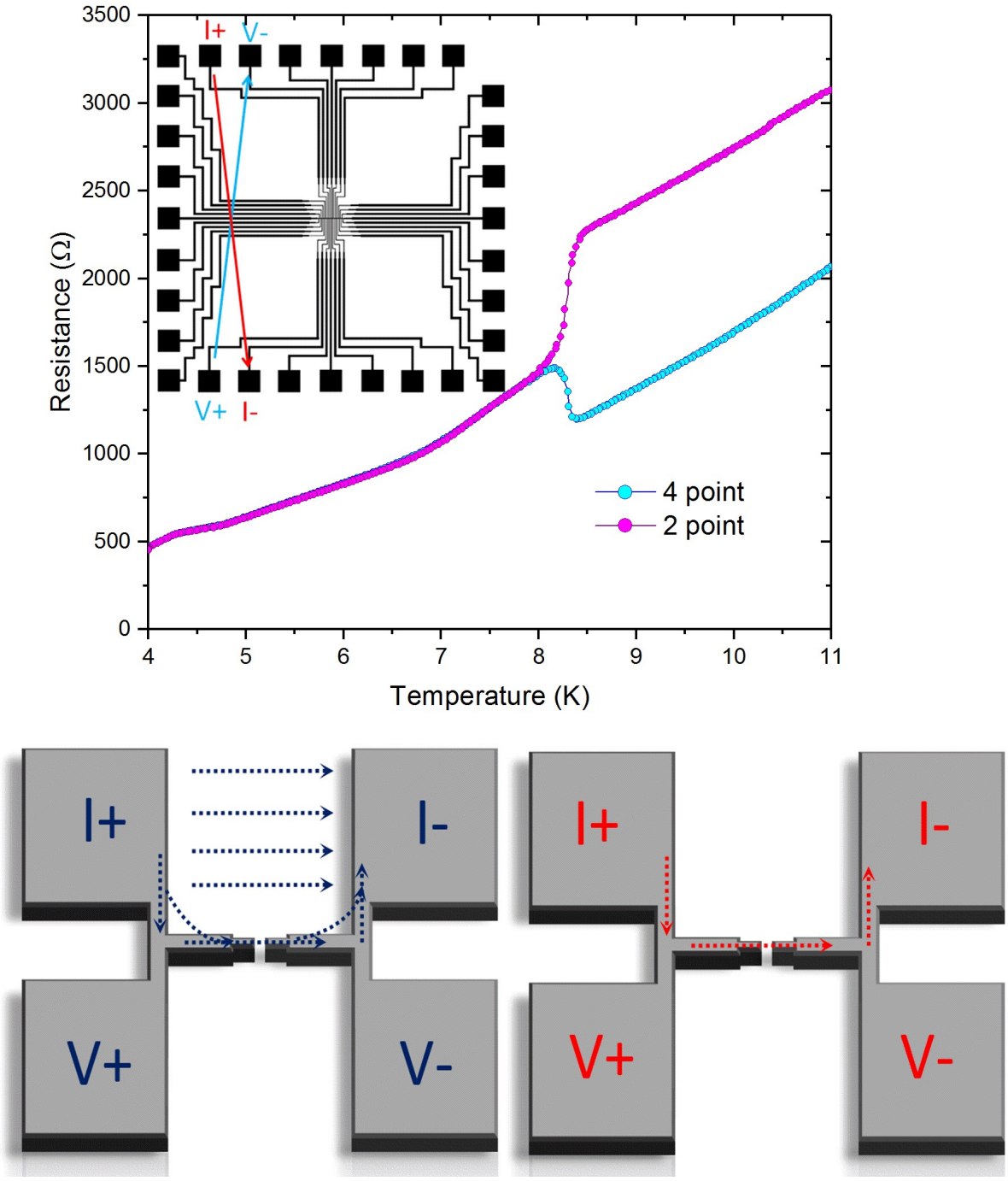

Figure 6.4: Two point (purple) and four point (blue) resistances of a Nb/STO/Nb junction illuminated with $\approx 0.5\ \mu\mathrm{Wcm}^{-2}$ of 310 nm light (top), the geometry of the contact pads used in the device in section 6.2 (inset), and a schematic of the current path illustrating the difference between the current paths in the normal and superconducting state (bottom).

This jump in resistance at the superconducting transition of the electrodes was observed ubiquitously across all devices that were measured, regardless of the fabrication method (EBL or FIB-OL), batch of Nb growth or size of devices. However the functional form of the jump was found to depend the geometry of the contact pads and wires used. In particular negative resistances in the normal state were only found in devices where the contact pads and wires were fabricated using the mask design shown in figure 3.7, such as the device presented in section 6.2. Whereas devices made by EBL (shown schematically in figure 6.4 bottom) showed the same peak in resistance at the critical temperature of the niobium but the normal state resistance did not become negative, data for devices using this geometry are shown in section 6.3.

To investigate this unusual behaviour further the two and four point resistances of the device were measured, this is shown in figure 6.4 (top). When the Nb contact pads and wires to the device are superconducting the two and four point resistances are almost equal (the two point resistance is $\approx 5\ \Omega$ s large which is due to the resistance of the wires between the sample holder in the probe and the nano-voltmeter). However there is a much larger difference ($\approx 1000\ \Omega$ s) between the two and four point resistances when the Nb is in the normal state. Consequently when a two point measurement of the superconducting transition is made the typical behavior that would be expected (i.e. a drop in resistance) is observed, wheres the four point measurement shows a peak in resistance. This is indicative of the four point measurement not giving an accurate reflection of the voltage when the niobium is in the normal state.

This inaccuracy can be explained by considering the path of the current through the sample. When the Nb wires and contact pads are superconducting any contribution of conductivity from the substrate is simply shorted out and all of the current passes through the device. However when the Nb is in the normal state some of the current is carrier by the substrate, directly between the current contacts and misses out the device altogether, this is shown schematically in figure 6.4. Consequently when the Nb is in the normal state a smaller voltage is measured across the device, making the resistance appear to be lower than it actually is, in a four point measurement. As all of the current will pass through the device when the Nb is superconducting a jump in resistance at T_c appears. In a two point measurement both substrate and device contributions to the conductivity are measured and the correct, larger, resistance is observed and a typical superconducting transition is appears. Since the resistance of the Nb wires is not photosensitive the ratio of substrate to device conductivity will be larger for a higher illumination intensities.

Alongside a peak in resistance the devices measured in section 6.2 also show a negative resistance in the normal state when a sufficiently high illumination power is used (see figure 6.3). This is in contrast to the devices presented in section 6.3 which show a peak in resistance at T_c but no negative resistance. This difference can be explained by considering the difference in geometry of the contact pads used in the two types of device, resulting from the different methods of fabrication. In section 6.2 devices were produced by a two stage FIB and optical lithography procedure (described in detail in section 3.1) whereby a set of 31 wire and contact pads were defined, before gaps were etched into a central wire of niobium with current and voltage wires perpendicular to this, rather than the simpler one stage EBL devices presented in section 6.3 (shown schematically in figure 6.4 bottom). As a result of this adjacent contact pads had the opposite polarity i.e. V^+I^-, V^-I^+ were paired, this is shown schematically in the inset of figure 6.4 (top). Therefore in this case when a significant percentage of the current is carried by the STO substrate rather than the Nb wires, the result is effectively a pseudo-four point measurement of the substrate with the incorrect polarity. Consequently when high illumination powers are used and the conductivity is dominated by the substrate the sample appears to have a negative resistance.

The spectral response of the junction measured at $T = 5$ K (shown in figure 6.5 top left) gives values of sheet resistance consistent with those previously measured in nominally stoichiometric samples between 310 and 370 nm (see figure 4.1 for example). However a deviation from stoichiometric behaviour is observed when the device is illuminated with 380 and 390 nm light. At 380 nm the sheet resistance is larger than in stoichiometric samples by a factor of approximately 10. Whereas at 390 nm the sheet resistance is $\approx$ 300 k$\Omega\square^{-1}$, as compared with stoichiometric samples where no photoconductivity is measured. Alongside this a dark resistance of $\approx$ 400 kΩs across the device is also observed. The build up and decay to and from this dark resistance is however relatively rapid, reaching equilibrium in around 60 s similarly to stoichiometric samples, indicating that photocarriers do not become trapped (shown in figure 6.5 top right). The sub-gap photoconductivity and dark conductivity is likely due to damage by the FIB milling of the surface, which is know to occur in STO [215,216]. The rapidity of recombination and similarly of above-gap spectral response as compared with bulk STO samples indicates that the imperfections responsible for the enhancement in dark conductivity do not act either as a minority carrier trap, or as an efficient recombination center. The broadening of the spectral response does however imply that some in-gap state or states are present

and mediate the absorption of sub-gap light. Although FIB-induced oxygen vacancies could explain the increased dark conductivity, they have previous been shown [117, 120, 121] to trap holes and lead to persistent photoconductivity, it is therefore unlikely that a significant density are present. The smaller dark conductivity could, however, be due to implanted Ga^+ ions or to redeposited Nb. IVs were measured as a function of wavelength and lamp power, shown in figure 6.5, however no supercurrent $I_c > 10$ nA was observed.

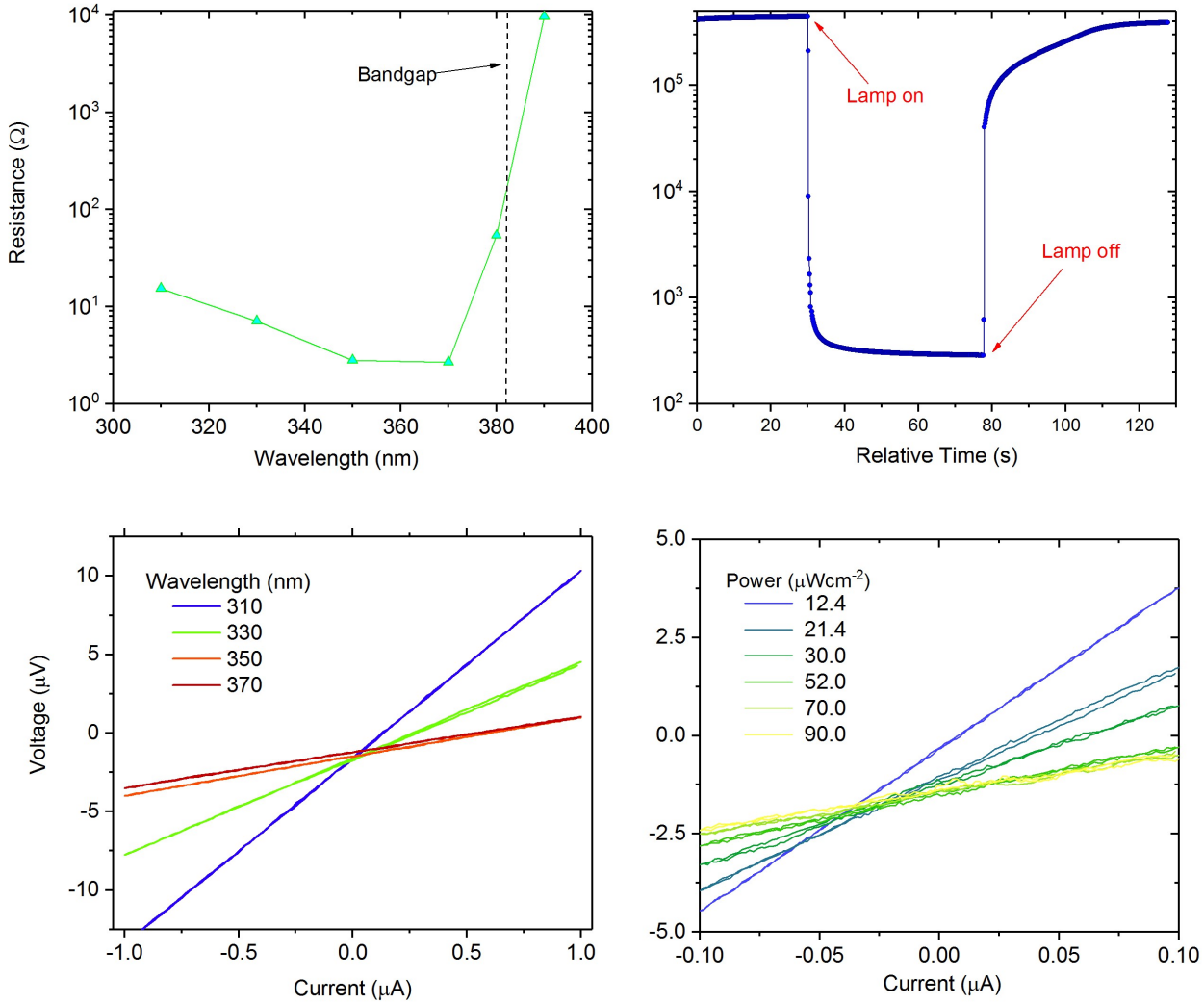

Figure 6.5: The spectral response of the device at $T = 5$ K using a power of 50 μWcm^{-2}(top left), the build up and decay of photoconductivity of the device at $T = 5$ K using a power of 6.7 μWcm^{-2} and wavelength of 310 nm (top right). The IV characteristics for the device as a function of power (bottom right) and wavelength (bottom left) at $T = 4$ K.

6.3 Junctions with a metallic interlayer

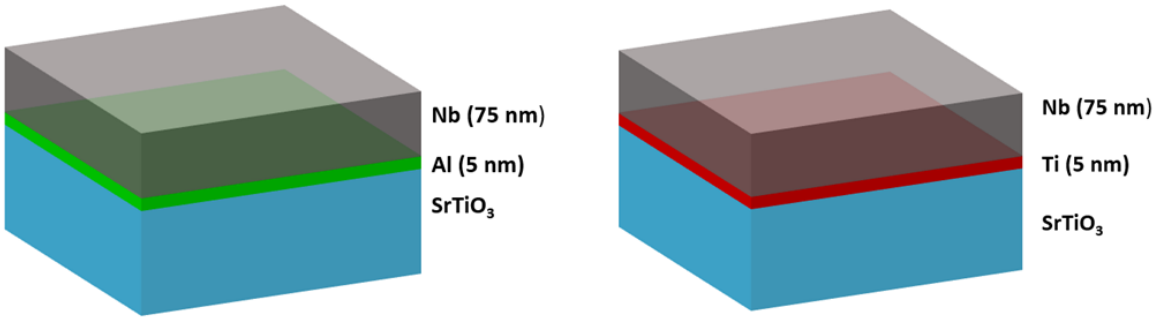

Figure 6.6: Schematics of the bilayer films grown on STO.

In many semiconducting Josephson junctions the interface transparency is low which, as shown by Blonder, Tinkham, and Klapwijk reduces the probability of Andreev reflection and therefore suppresses the Josephson effect [80–82]. However superconducting-semiconducting interfaces with near unity transparency can be fabricated, for example between niobium and InAs [187,217,218] as well as with other superconducting electrodes such as aluminum [219] or tantalum [220]. This can be achieved by growing the semiconductor and superconductor in-situ [221, 222] or by argon milling the surface of the semiconductor before depositing a metallic layer, such as titanium or palladium, between the semiconductor and superconductor [223, 224].

In section 6.2 devices made from Nb films on STO did not show the Josephson effect, a potential cause of this could be poor interface transparency. Consequently devices with a metallic interlayer were made, in an effort to improve the interface transparency. Here results are presented for devices fabricated from films of niobium with 5 nm layers of titanium and aluminum between the superconducting niobium layer and the insulating STO substrate (shown schematically in figure 6.6).

6.3.1 Aluminum interlayer

In this section data for devices fabricated from a Nb/Al bilayer film on an STO substrate is presented. Due to the additional wet etching required to remove the aluminum, a thicker layer of photoresist was used during fabrication, consequently the size was ultimately sightly larger than in single layer devices. Data for a 200 nm Nb/Al/STO/Al/Nb

device (an SEM image is shown in figure 6.8) and a continuous 1 μm wire of Nb/Al on STO are presented below.

$R(T)$ curves as a function of power, using 370 nm light, and wavelength, at a power of $\approx$ 50 μWcm^{-2}, between 4 and 10 K are shown in figure 6.7. Similarly to the device shown in section 6.2 the Nb electrodes become superconducting at a critical temperature of just over 8 K at low lamp powers, suppressed to around 6.5 K at a power of $\approx$ 220 μWcm^{-2} (the maximum power used is this section is larger than in section 6.2 as 370 nm light is used). This reduction in T_c is reflected in the 1 μm wire (figure 6.8 top right) as well as a reduction in the size of the transition as the illumination intensity is increased and the substrate becomes more conducting. Once again a peak in resistance at the T_c of the Nb electrodes is observed, although it is much smaller than in section 6.2 as the geometry of the contacts (the same as shown in figure 6.4) is such that the change in the current path is less extreme and does not lead to a negative resistance. IVs were measured as a function of wavelength and lamp power, shown in figure 6.8, however no supercurrent $I_c > 10$ nA was observed at $T = 4$ K.

The spectral response of the device measured at 5 K is shown in figure 6.8 (bottom left). Making a simple approximation of the current being homogeneous through a rectangle of 1 μm by 200 nm, the values of sheet resistance are found to be larger by approximately a factor of 2 than those previously measured in stoichiometric samples, between 310 and 370 nm (see figure 4.1 for example). The normalised spectral response is, however, similar to that found in stoichiometric STO indicating that the reduction in photosensitivity is unrelated to the sheet thickness of the photocarriers. After the shutter was closed the photoconductivity was found to initially decay rapidly, the resistance increasing by two orders of magnitude in < 5 s, shown in figure 6.8 (top right). However after the initial decay a much slower tail was observed, indicative of a small density of hole traps which do not have a significant effect on the photosensitivity at high generation rates.

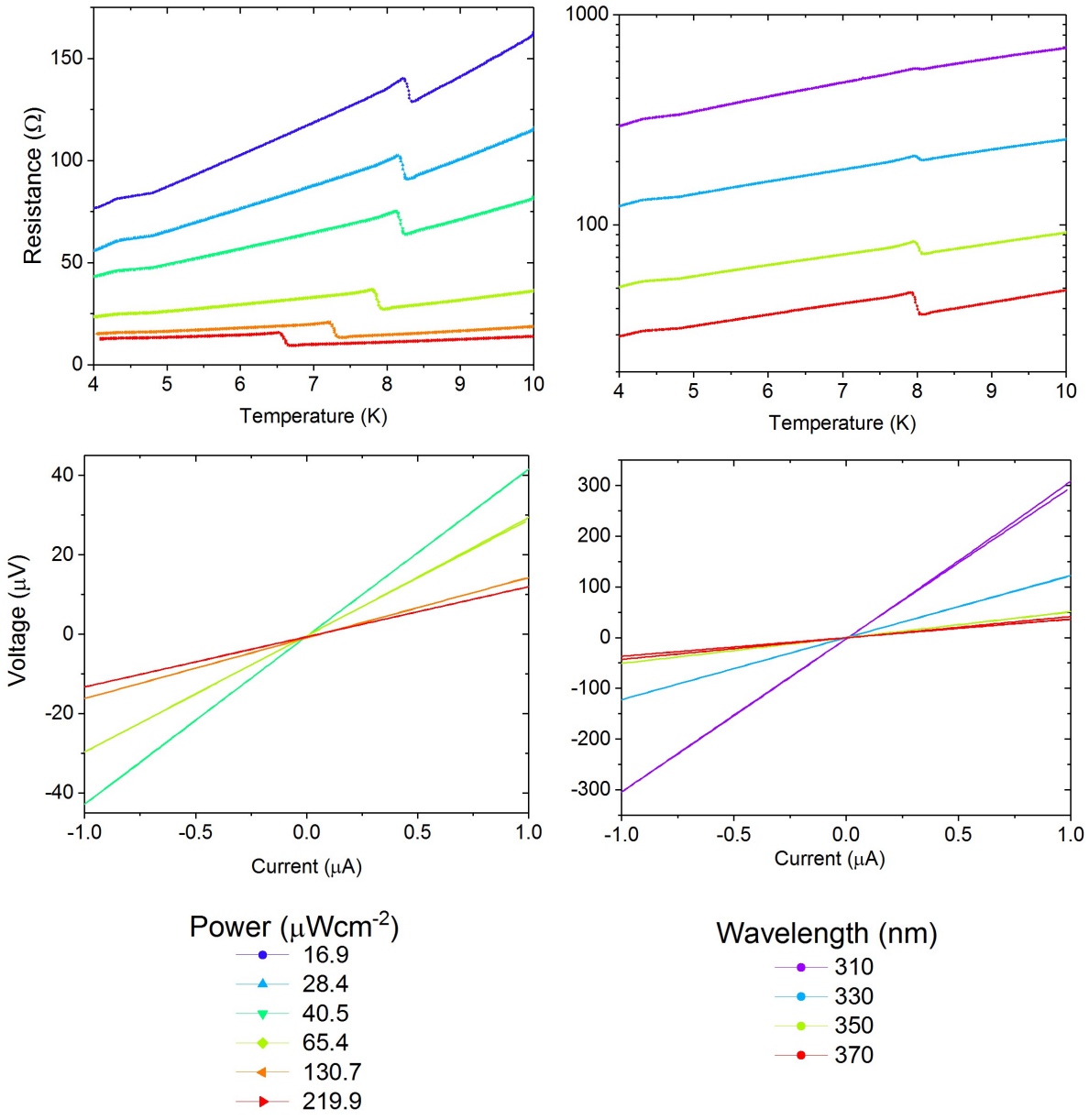

Figure 6.7: $R(T)$s as a function of power (top left) using 310 nm light and wavelength (top right) using a power of 50 μWcm^{-2}. IV characteristics for the device as a function of power using 310 nm light (bottom left) and wavelength using a power of 50 μWcm^{-2} (bottom right) at $T = 4$ K.

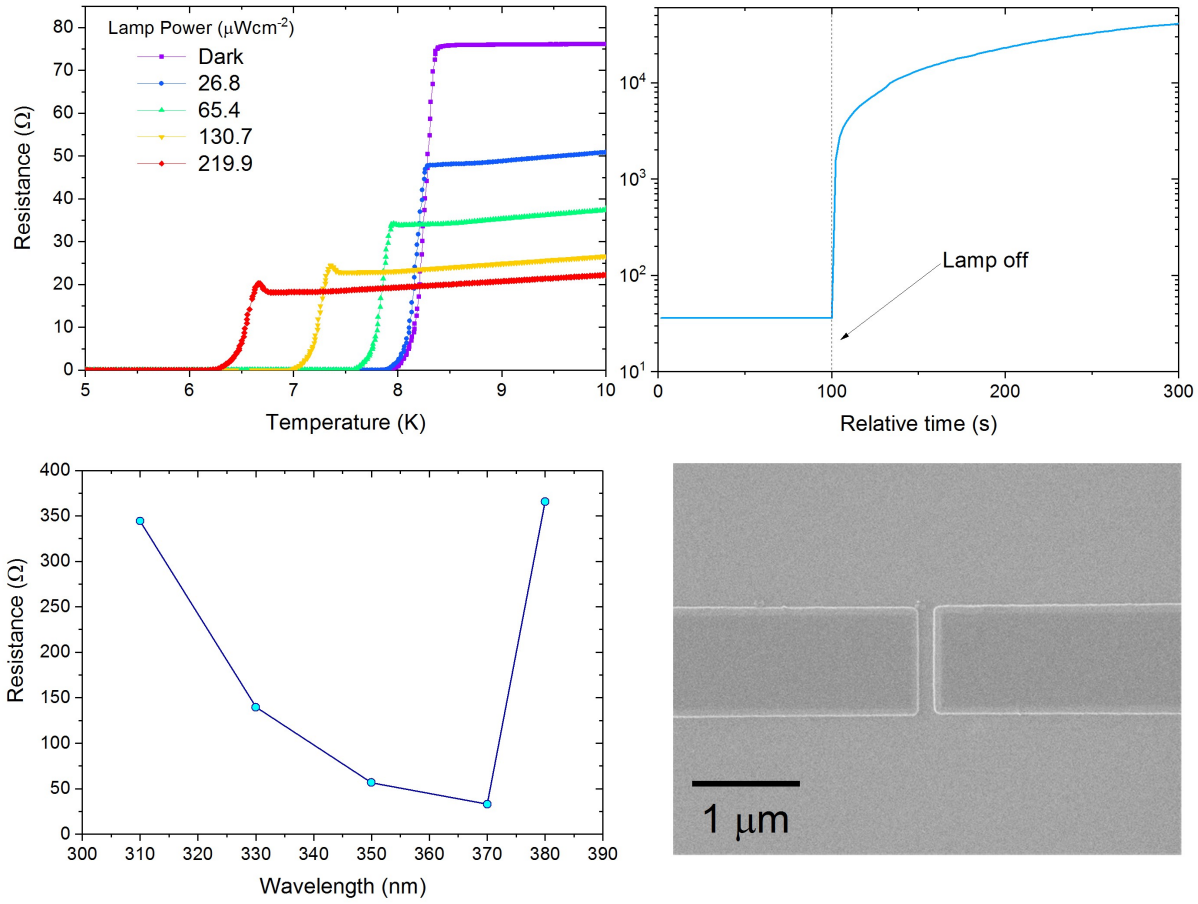

Figure 6.8: $R(T)$s as a function of lamp power using 370 nm light for a continuous wire of niobium on the same sample as the device (top left). The decay of photoconductivity of the device at $T = 5$ K using a power of 50 μWcm^{-2} and wavelength of 370 nm (top right). The spectral response of the device at 5 Kelvin using a power of 50 μWcm^{-2} (bottom left). An SEM image of the device (bottom right).

When fabrication tests were performed on the same bilayer film (75 nm niobium layer and 5 nm aluminum) but grown on silicon instead of STO, an SF_6 plasma was found to stop etching on the aluminum layer (consistent with previous reports [94, 95]) which was subsequently removed with a TMAH wet etch (see section 3.1.3.2). However when the same structures were patterned and etched on STO substrates, it was found that the SF_6 etched through both the Nb *and* Al layers. Depositing thin Al films on STO has recently been shown to remove oxygen from the surface of the STO and form AlO_x, even when grown at room temperature [225] [226]. This may explain both the anomalous etching of the Al layer and small persistent photoconductivity, however since no measurable dark conductivity was observed the density of any oxygen vacancies must be low.

6.3.2 Titanium interlayer

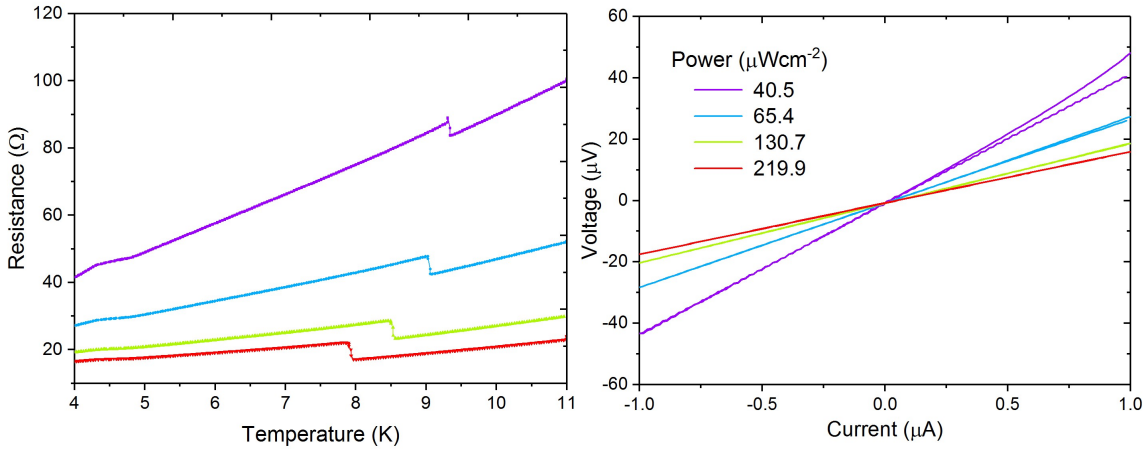

Figure 6.9: $R(T)$s (left) and IV's at $T = 4$ K (right) as a function of power using 370 nm light.

In this section data for devices fabricated from a Nb/Ti bilayer film on an STO substrate is presented. Ti does etch in SF_6 so can be completely etched in a single step, however the etch rate was found to be lower than that of Nb. Consequently and longer etch and therefore a thicker resist layer was required, as such the smallest Nb/Ti/STO/Ti/Nb device was $\approx$ 150 nm wide. Data for this device and a continuous 1 μm wide wire of Nb/Ti on STO are shown below.

$R(T)$s between 4 and 11 K and IV characteristic at 4 K as a function of power, using 370 nm light are shown in figure 6.9, left and right respectively. These $R(T)$s also show a peak in resistance at the T_c of the Nb electrodes, similar in magnitude to that seen in section 6.3.2, as both sets of devices have an identical configuration of contact pads. In contrast to the previous Nb/Al devices however the critical temperature is $\approx$ 9.1 K, close to the bulk value. This critical temperature is also suppressed only to around 8 K at a power of $\approx$ 220 μWcm^{-2}, 1.5 K higher than for Nb/Al devices. Both the Nb/Al and Nb/Ti bilayers were grown in the same chamber, on the same day and were patterned and measured within a week of each other, so this difference in T_c may indicate a increased proximity effect in the Nb/Al bilayer, which would suppress the T_c of the Nb layer. IVs were measured as a function of lamp power at 370 nm, shown in figure 6.9, however no supercurrent $I_c > 10$ nA was observed at $T = 4$ K.

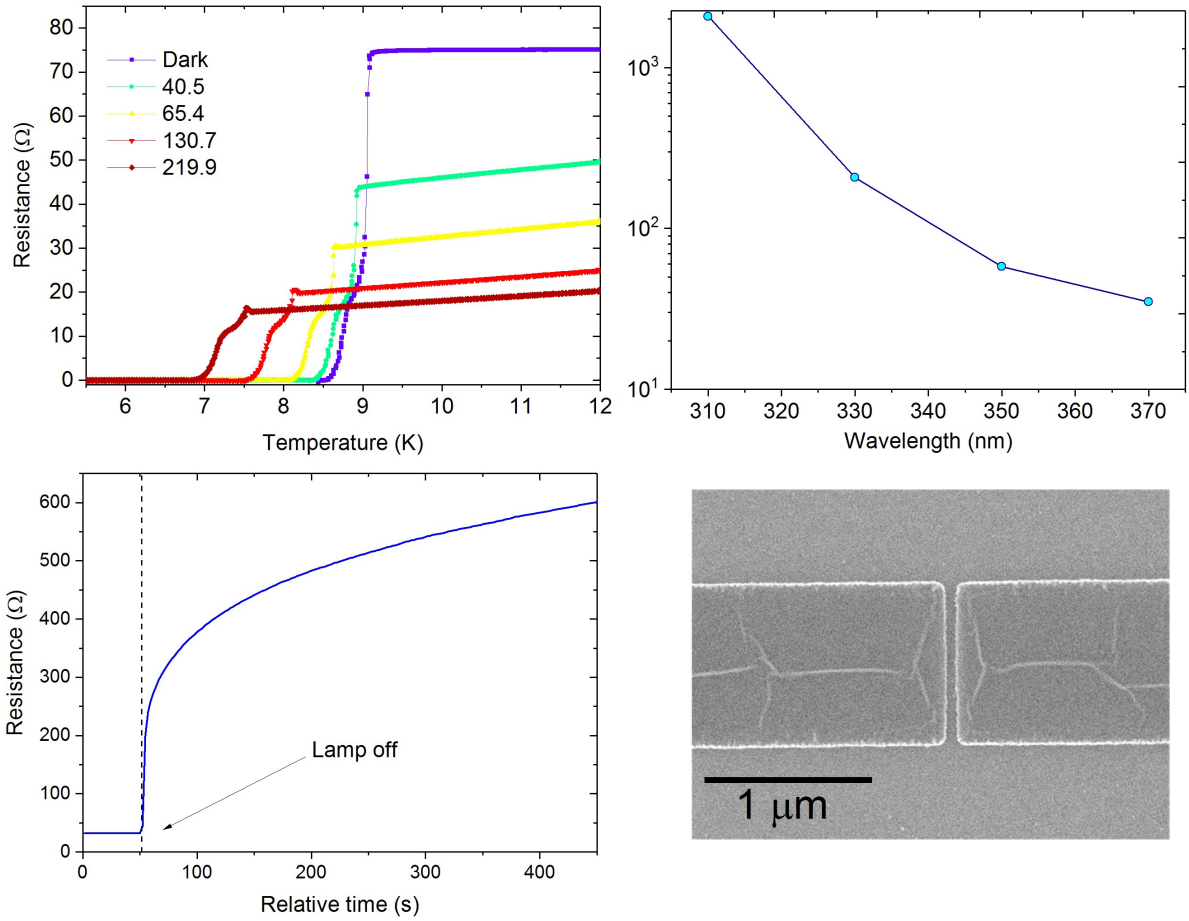

Figure 6.10: $R(T)$s as a function of lamp power using 370 nm light for a continuous wire of niobium on the same sample as the device (top left). The spectral response of the device at $T = 5$ K using a power of 50 μWcm^{-2} (top right). The decay of photoconductivity of the device at $T = 5$ K using a power of 50 μWcm^{-2} and wavelength of 370 nm (bottom left). An SEM image of the device (bottom right).

The spectral response of the device measured at 5 K is shown in figure 6.10 (top right). The value of the sheet resistance when illuminated with 370 nm light is $\approx$ 190 $\Omega\square^{-1}$ similar to that found in the Nb/Al device which is around twice as large as is found in stoichiometric STO or the device in section 6.2. Sheet resistances for 330 and 350 nm light were also close to those previously found in the Nb/Al device, however the value for 310 nm light is more than 10 times larger at $\approx$ 13 k$\Omega\square^{-1}$. This indicates an increase in surface localised efficient recombination centers which, given that the STO used here was from the same batch as the Nb/Al device, have likely been caused either by the deposition of the Ti or in the additional etching required.

An example of recombination at 5 K, using 370 nm, 50 μWcm^{-2} light is shown in figure 6.10 (bottom right). The decay in photoconductivity is found to be slow, reaching a sheet resistance of approximately 2.5 k$\Omega\square^{-1}$ in around 60 seconds. The decay can be fitted to a stretched exponential, with parameters of $\tau = 0.5$ s and $\beta = 0.13$. In contrast to previous measurements of persistent photoconductivity, there is no increase in photosensitivity. Similarly to Al, the deposition of Ti has also been shown to create oxygen vacancies at the surface of STO [227], these may be responsible for the increase in photocarrier lifetime.

6.4 Future work on realising optically tunable junctions

There are several possible reasons that the devices in this chapter do not show any observable supercurrent. One possibility is that the size of the junctions may simply be much larger that the normal coherence length of the STO. A simple estimate of this can be made by calculating the diffusion constant from Einsteins relation [228],

$$D = \sqrt{\frac{\mu k_b T}{e}}. \tag{6.1}$$

Using a value for the mobility of $\approx 10^4$ cm^{2}V^{-1}s^{-1} as previously measured by Kozuka in photodoped STO [23], a diffusion constant of 3.45 cms^{-1} is obtained for a temperature of 4 K. Substituting this value into equation 2.30 yields a normal state coherence length of ≈ 25 nm at 4 K, somewhat smaller than the minimum junction size measured in this work. Alternative, or indeed in addition to this problem, the transparency of the interface between the Nb and STO may be be too low, suppressing the probability of andreev reflection.

A potential route forward to solve these problems is to change the geometry of the devices from lateral to the more common sandwich type junctions, where a thin film of STO would be "sandwiched" between two superconducting layers. This would allow a dramatic reduction is the size of the junction as it is possible to grow STO with atomic layer precision, much smaller than can be defined and etched lithographically, although the growth of high quality STO is, of course, difficult. Furthermore the doping of the STO barrier could be adjusted, so that the carrier density or photocarrier lifetime could be tuned and the transparency of the interface controlled more careful with in situ deposition.

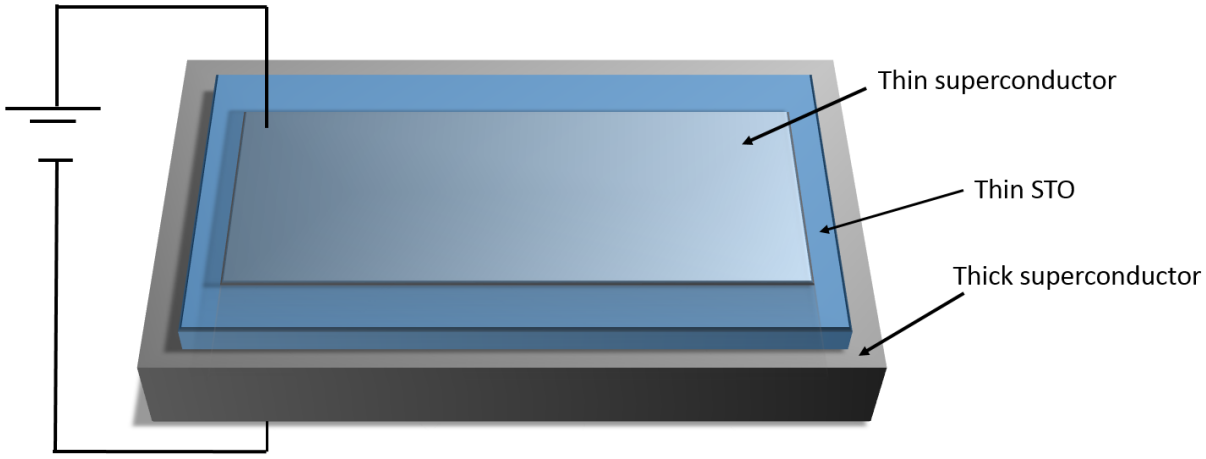

Figure 6.11: A schematic of a sandwich Josephson junction with a transparent Nb top electrode.

This is not, however without its drawbacks. Similarly to section 4.2.2 using chemically doped STO then photodoping on top of this existing carrier density may seem to be an attractive option, however again this would severely limit the degree to which the device could be tune. Furthermore whilst in situ deposition has previously been shown to improve the transparency of the semiconductor-superconductor interface, if oxygen is diffusing from the STO into the niobium, as has been observed between aluminum films grown on STO [229], then the resulting layer of insulating NbO_x may be the limiting factor in improving transparency. Ultimately a different superconducting material or suitable barrier layers may also be required for sandwich type junctions to be realised.

6.4.0.1 Transparent niobium films

A clear condition for creating tunable sandwich type junctions is the ability to efficiently tune through the top superconducting electrode, i.e. it must be sufficiently transparent to UV light that the STO underneath can be photo-doped and that the superconductivity in the Nb is not completely suppressed. To explore the feasibility of this idea 75 Å, visibly transparent films of Nb were grown on STO. Substrates of STO were first irradiated with Ar^+ using the same recipe as in section 4.3, to create a thin layer ($\approx$ 20 nm) of oxygen vacancies, so as to utilize the persistent photoconductivity observed in Ar^+ irradiated STO. Because optically induced carriers are longer lived, on the time scale of hours, excited single particle states in the Nb relax back into the superconducting condensate far quicker than the STO does to its dark, equilibrium, state, allowing photocarriers to be

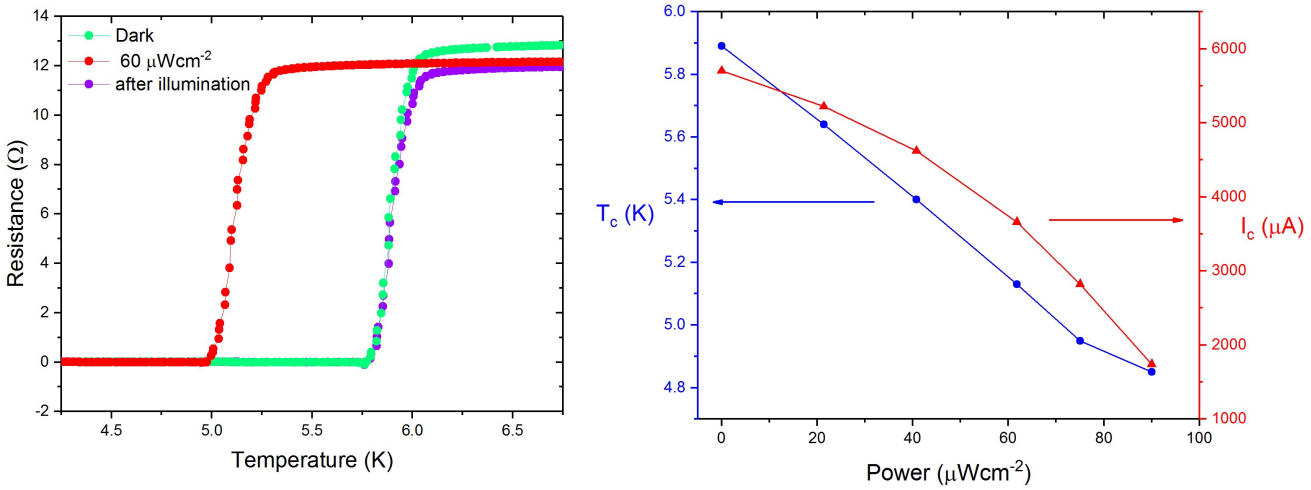

Figure 6.12: $R(T)$s of the transparent Nb film in the dark (green), with 50 μWcm^{-2} of 310 nm light (red), and an $R(T)$ taken immediately after the lamp has been switched off (purple). The critical temperature (blue) and critical current (red) of the films as a function of lamp power using 310 nm light, IV measurements were performed at $T = 4$ K.

added without a suppression in T_c.

The critical temperature and current as a function of lamp power for 310 nm light is shown in figure 6.11 (right). The dark T_c of the film is $\approx$ 5.9 Kelvin, close to previous measurements on Nb films of similar thickness, however the critical current density is found to be $\approx$ 100 times smaller than previous reports [230]. The critical temperature is further suppressed to $\approx$ 4.9 Kelvin at 90 μWcm^{-2} of illumination accompanied by a reduction in the critical current by a factor of $\approx$ 3. $R(T)$s for the thin Nb film in the dark, with 60 μWcm^{-2}, 310 nm light, and in the dark but taken immediately after the 60 μWcm^{-2} illumination ceased are shown in figure 6.11 (left). The $R(T)$ taken immediately after illumination has ceased shows a recovery to the dark T_c, but with the reduction in the normal state resistance still present. The resistance of the whole sample is reduced by about 10 %. Using a simple model of two parallel resistors and assuming the sheet resistance of the Ar$^+$ irradiated STO is $\approx$ 50 $\Omega\square^{-1}$ (see section 4.3), and that the resistance of the Nb is not changed by the light, then the resistance of the STO is reduced by around 20%, only slight less that was previously observed in section 4.3. This indicates that it is possible to efficiently create carriers in the STO through a 7.5 nm superconducting Nb

layer.

These initial tests indicate that it may be possible to create sandwich Josephson junction (shown schematically in figure 6.12), with a thin Nb top layer which is relatively transparent to UV light and retains a reasonably high critical temperature even under high intensity illumination.

6.5 Summary

In this chapter representative sets of data for STO based photo-tunable devices has been presented. 60 nm wide Nb/STO/Nb junctions were measured in section 6.2. An unusual feature of this data is the shape of the superconducting transition, which shows a peak in resistance at the T_c of the Nb electrodes and for some powers *negative* resistance when the Nb electrodes are in the normal state. This was due to the substrate contribution to conductivity being shorted out when the Nb became superconducting. The sheet resistance of this device was close to that of plain STO for wavelengths of illumination between 310 and 370 nm. Despite showing some dark conductivity, indicating the presence of defects, the build-up and decay of photoconductivity was rapid similarly to bulk STO samples. No combination of wavelength and power, however, lead to non-linear IV's. In section 6.3 data for devices with a Al and Ti interlayer was presented, as this was thought to potential improve the interface transparency. However these neither of these device showed an observable supercurrent $I_c > 10$ nA.

In section 6.4 a potential future route to realizing optically tunable Josephson junction in STO has been outlined. Data presented here indicates that it may be possible to make sandwich junctions with a transparent top electrode by utilizing the persistent photoconductivity in oxygen deficient STO films. The critical temperature of the superconducting film is found to recover to its dark value much more quickly than the underlying STO which could potentially be utilised to create a large carrier density in the STO without suppressing the superconductivity of the thin Nb film.

Chapter 7

Concluding remarks

In this thesis results have been presented for measurement of photoconductivity in strontium titanate. Four systems have been investigated, stoichiometric STO, $SrTiO_{3-\delta}$, UV irradiated STO, and niobium/STO superconducting devices.

Results for nominally stoichiometric STO have offered further evidence of a dramatic increase in photocarrier lifetime below ≈ 35 K, consistent with other recent works. Along with this linear photoconductivity ($\gamma = 0.94$) has been observed up to carrier densities of $\sim 10^{18}$ cm^{-3} suggesting monomolecular recombination is dominant. When the temperature is reduced further to < 1 K persistent photoconductivity is found to emerge. The onset of persistent photoconductivity coincides with a large increase in the capture cross section of a charged defect, indicating that this may be responsible. These data are supportive of the hypothesis that large photogenerated electron lifetimes are caused by a sensitizing level with a much larger capture cross section for holes than electrons. The most likely origin of the sensitizing level is strontium vacancies, however further work is required to confirm this definitively.

Persistent photoconductivity has also been observed in thin films of $SrTiO_{3-\delta}$, produced by Ar^+ irradiation, as well as the additional non-equilibrium effect of transient negative photoconductivity. Whilst persistent photoconductivity has previous been observed in bulk $SrTiO_{3-\delta}$, negative photoconductivity has not been found in any other studies. It is possible that this is simply due to the illumination intensity being too high in previous works, as negative photoconductivity is only found to emerge at low light powers. However other factors, intrinsic to Ar^+ irradiated STO (such as the amorphous top layer creating in-gap states) may also be essential to negative photoconductivity, explain why it has not previously been seen in bulk samples. Further studies of the relationship between negative photoconductivity and oxygen vacancies in STO are therefore required to fully understand this effect.

The work presented in this chapter 5 of this thesis has shown that broadband UV exposure can induce persistent photoconductivity in nominally stoichiometric STO, with photocarrier lifetimes which can be tuned by the exposure dose. The photoinduced state can be removed by thermally cycling to 150 K indicating that oxygen plays an important role in this effect. However if the sample is kept at low temperature and in vacuum the optically induced state appears to decay negligibly on the timescale of days. The origin of the photoinduced state is not yet clear, although the formation of oxygen vacancies at the surface seem to be the most plausible explanation. However the creation of other pos-

itively charged surface adsorbents, for example by photo-catalytic water splitting, cannot be ruled out and further experiments are required to clarify this. In previous ARPES studies intense UV exposure was shown to create oxygen vacancies by core hole Auger decay. If the origin of the persistent photoconductivity observed in this work is indeed oxygen vacancies then understanding the mechanism of there creation with lower energy photons is important question to answer. Furthermore establishing whether or not a similar photoinduced state can be created in other transition metal oxides is another key question. Indeed recent ARPES measurements have shown that UV induced oxygen vacancies can also be created in potassium tantalate, suggesting that a UV induced surface state may be more widely applicable. If this is the case then intense UV exposure could potentially be used as a tool for tuning oxide interfaces and heterostructures.

In the final experimental chapter of this thesis results for STO based photo-tunable devices were presented, in an attempt to create optically tunable Josephson junctions. Devices as small as 60 nm were fabricated but no observable supercurrent was found. However it was also shown that it is possible to tune the STO substrate through a 7.5 nm layer of superconducting niobium. This opens up a potential future direction for realising optically tunable sandwich type Josephson junctions, possibly also utilising the long live persistence photoconductivity which can be induced in $SrTiO_{3-\delta}$.

Bibliography

[1] C. Lee, J. Destry, and J. Brebner. 'Optical absorption and transport in semiconducting $SrTiO_3$.' *Phys. Rev. B*, **11** (6), 2299 (1975).

[2] J. A. Noland. 'Optical absorption of single-crystal strontium titanate.' *Phys. Rev.*, **94** (3), 724 (1954).

[3] L. F. Mattheiss. 'Energy bands for $KNiF_3$, $SrTiO_3$, $KMoO_3$, and $KTaO_3$.' *Phys. Rev. B*, **6** (12), 4718 (1972).

[4] A. H. Kahn and A. J. Leyendecker. 'Electronic energy bands in strontium titanate.' *Phys. Rev.*, **135**, A1321 (1964).

[5] D. Goldschmidt and H. L. Tuller. 'Fundamental absorption edge of $SrTiO_3$ at high temperatures.' *Phys. Rev. B*, **35**, 4360 (1987).

[6] G. Shirane and Y. Yamada. 'Lattice-dynamical study of the 110 °K phase transition in $SrTiO_3$.' *Phys. Rev.*, **177**, 858 (1969).

[7] L. Rimai and G. A. deMars. 'Electron paramagnetic resonance of trivalent gadolinium ions in strontium and barium titanates.' *Phys. Rev.*, **127**, 702 (1962).

[8] R. Loetzsch, A. Lübcke, I. Uschmann, E. Förster, V. Große, M. Thuerk, T. Koettig, F. Schmidl, and P. Seidel. 'The cubic to tetragonal phase transition in $SrTiO_3$ single crystals near its surface under internal and external strains.' *Appl. Phys. Lett.*, **96** (7), 071901 (2010).

[9] C. Koonce, M. L. Cohen, J. Schooley, W. Hosler, and E. Pfeiffer. 'Superconducting transition temperatures of semiconducting $SrTiO_3$.' *Phys. Rev.*, **163** (2), 380 (1967).

[10] X. Lin, Z. Zhu, B. Fauqué, and K. Behnia. 'Fermi surface of the most dilute superconductor.' *Phys. Rev. X*, **3** (2), 021002 (2013).

[11] O. Prakash, A. Kumar, A. Thamizhavel, and S. Ramakrishnan. 'Evidence for bulk superconductivity in pure bismuth single crystals at ambient pressure.' *Science*, **355** (6320), 52 (2017).

[12] J. Schooley, W. Hosler, and M. L. Cohen. 'Superconductivity in semiconducting $SrTiO_3$.' *Phys. Rev. Lett.*, **12** (17), 474 (1964).

[13] J. Hulm, M. Ashkin, D. Deis, and C. Jones. Chapter 5 Superconductivity in Semiconductors and Semi-Metals, volume 6 of *Progress in Low Temperature Physics* (Elsevier1970).

[14] J. Schooley, W. Hosler, E. Ambler, J. Becker, M. L. Cohen, and C. Koonce. 'Dependence of the superconducting transition temperature on carrier concentration in semiconducting $SrTiO_3$.' *Phys. Rev. Lett.*, **14** (9), 305 (1965).

[15] J. Ruhman and P. A. Lee. 'Superconductivity at very low density: the case of strontium titanate.' *Phys. Rev. B*, **94** (22), 224515 (2016).

[16] H. Noad, E. M. Spanton, K. C. Nowack, H. Inoue, M. Kim, T. A. Merz, C. Bell, Y. Hikita, R. Xu, W. Liu, *et al.* 'Variation in superconducting transition temperature due to tetragonal domains in two-dimensionally doped $SrTiO_3$.' *Phys. Rev. B*, **94** (17), 174516 (2016).

[17] A. G. Swartz, H. Inoue, T. A. Merz, Y. Hikita, S. Raghu, T. P. Devereaux, S. Johnston, and H. Y. Hwang. 'Polaronic behavior in a weak-coupling superconductor.' *Proc. Natl. Acad. Sci. U.S.A.*, **115** (7), 1475 (2018).

[18] D. Eagles. 'Possible pairing without superconductivity at low carrier concentrations in bulk and thin-film superconducting semiconductors.' *Phys. Rev.*, **186** (2), 456 (1969).

[19] G. Cheng, M. Tomczyk, S. Lu, J. P. Veazey, M. Huang, P. Irvin, S. Ryu, H. Lee, C.-B. Eom, C. S. Hellberg, *et al.* 'Electron pairing without superconductivity.' *Nature*, **521** (7551), 196 (2015).

[20] S. Kasahara, T. Watashige, T. Hanaguri, Y. Kohsaka, T. Yamashita, Y. Shimoyama, Y. Mizukami, R. Endo, H. Ikeda, K. Aoyama, *et al.* 'Field-induced superconducting phase of FeSe in the bcs-bec cross-over.' *Proc. Natl. Acad. Sci. U.S.A.*, **111** (46), 16309 (2014).

[21] K. X. Jin, B. C. Luo, Y. F. Li, C. L. Chen, and T. Wu. 'Photoinduced phase transition and relaxation in bare $SrTiO_3$ single crystals.' *J. Appl. Phys.*, **114** (3), 033509 (2013).

[22] Y. Kozuka. 'Transport properties of photocarrier-doped $SrTiO_3$.' Master's thesis, The University of Tokyo (2007).

[23] Y. Kozuka, M. Kim, C. Bell, B. G. Kim, Y. Hikita, and H. Hwang. 'Two-dimensional normal-state quantum oscillations in a superconducting heterostructure.' *Nature*, **462** (7272), 487 (2009).

[24] A. Spinelli, M. Torija, C. Liu, C. Jan, and C. Leighton. 'Electronic transport in doped $SrTiO_3$: Conduction mechanisms and potential applications.' *Phys. Rev. B*, **81** (15), 155110 (2010).

[25] H. Yasunaga. 'Photo-hall effect in strontium titanate.' *J. Phys. Soc. Jpn.*, **24** (5), 1035 (1968).

[26] C. E. Ekuma, M. Jarrell, J. Moreno, and D. Bagayoko. 'First principle electronic, structural, elastic, and optical properties of strontium titanate.' *AIP Adv.*, **2** (1), 012189 (2012).

[27] W. Smith. 'The action of light on selenium.' *Proc. Royal Soc. Lond.*, **25**, 113 (1876).

[28] K. Jin, W. Lin, B. Luo, and T. Wu. 'Photoinduced modulation and relaxation characteristics in $LaAlO_3/SrTiO_3$ heterointerface.' *Sci. Rep.*, **5**, 8778 (2015).

[29] P. Gorlich. Photoconductivity In Solids (Dover Publications1967).

[30] J. Singleton. Band Theory and Electronic Properties of Solids (Oxford University Press2001).

[31] R. H. Bube. Photoconductivity Of Solids (Wiley1960).

[32] R. H. Bube. Photoelectronic Properties of Semiconductors (Cambridge University Press1992).

[33] R. H. Bube. 'Imperfection ionization energies in CdS-type materials by photoelectronic techniques.' *Solid State Physics*, **11**, 223 (1960).

[34] G. A. Swartz. 'Negative photoconductivity in epitaxial GaAs grown on chrome-doped substrate.' *Jpn. J. Appl. Phys.*, **10** (9), 1285 (1971).

[35] F. Hasegawa. 'Comments on the negative photoconductivity in epitaxial GaAs grown on chrome-doped substrate.' *Jpn. J. Appl. Phys.*, **10** (9), 1286 (1971).

[36] V. A. Kulbachinskii, V. G. Kytin, A. V. Golikov, R. A. Lunin, R. T. F. van Schaijk, A. de Visser, A. P. Senichkin, and A. S. Bugaev. 'Wavelength dependent negative and positive persistent photoconductivity in Sn δ-doped GaAs structures.' *Semicond. Sci. Technol.*, **15** (9), 895 (2000).

[37] Q. Wan, T. H. Wang, and C. L. Lin. 'Third-order optical nonlinearity and negative photoconductivity of Ge nanocrystals in Al_2O_3 dielectric.' *Nanotechnology*, **14** (11), L15 (2003).

[38] C. Biswas, F. Günes, D. D. Loc, S. C. Lim, M. S. Jeong, D. Pribat, and Y. H. Lee. 'Negative and positive persistent photoconductance in graphene.' *Nano Lett.*, **11** (11), 4682 (2011).

[39] A. Cavalheiro, E. C. F. da Silva, A. A. Quivy, E. K. Takahashi, S. Martini, M. J. da Silva, E. A. Meneses, and J. R. Leite. 'Influence of illumination on the quantum mobility of a two-dimensional electron gas in Si δ-doped GaAs/$In_{0.15}Ga_{0.85}As$ quantum wells.' *J. Phys. Condens. Matter*, **15** (2), 121 (2003).

[40] Y.-C. Wu, C.-H. Liu, S.-Y. Chen, F.-Y. Shih, P.-H. Ho, C.-W. Chen, C.-T. Liang, and W.-H. Wang. 'Extrinsic origin of persistent photoconductivity in monolayer MoS_2 field effect transistors.' *Sci. Rep.*, **5**, 11472 (2015).

[41] P. Petersen. 'Photoeffects in potassium tantalate.' *J. Appl. Phys.*, **44** (3), 1240 (1973).

[42] J. Reemts and A. Kittel. 'Persistent photoconductivity in highly porous ZnO films.' *J. Appl. Phys.*, **101** (1), 013709 (2007).

[43] J. Li, J. Lin, H. Jiang, M. Asif Khan, and Q. Chen. 'Persistent photoconductivity in a two-dimensional electron gas system formed by an AlGaN/GaN heterostructure.' *J. Appl. Phys.*, **82** (3), 1227 (1997).

[44] B. Li, W. Ge, J. Wang, and K. Chen. 'Persistent photoconductivity and carrier transport in AlGaN/ GaN heterostructures treated by fluorine plasma.' *Appl. Phys. Lett.*, **92** (8), 082105 (2008).

[45] S. C. P. Rodrigues, G. M. Sipahi, L. M. R. Scolfaro, and J. R. Leite. 'Hole charge localization and band structures of p-doped GaN/InGaN and GaAs/InGaAs semiconductor heterostructures.' *J. Phys. Condens. Matter*, **14** (23), 5813 (2002).

[46] W. Kraak, N. Y. Minina, A. M. Savin, A. A. Ilievsky, I. V. Berman, and C. B. Sorensen. 'Persistent photoconductivity in p-type $Al_{0.5}Ga_{0.5}As/GaAs/Al_{0.5}Ga_{0.5}As$ heterostructures.' *Nanotechnology*, **12** (4), 577 (2001).

[47] E. S. Kannan, G.-H. Kim, I. Farrer, and D. A. Ritchie. 'Charge trapping in a double quantum well system.' *J. Phys. Condens. Matter*, **20** (45), 455206 (2008).

[48] Y. Liu, J. Yin, P. Wang, J. Zhu, M. Wanyun, Z. Dong, and J. Sun. 'Broadband photoresponse based on a synergetic effect of surface ions and plasmon polaritons.' *J. Mater. Chem. C*, **6** (5), 1199 (2018).

[49] H. J. Queisser. 'Nonexponential relaxation of conductance near semiconductor interfaces.' *Phys. Rev. Lett.*, **54**, 234 (1985).

[50] R. G. Palmer, D. L. Stein, E. Abrahams, and P. W. Anderson. 'Models of hierarchically constrained dynamics for glassy relaxation.' *Phys. Rev. Lett.*, **53**, 958 (1984).

[51] D. C. Johnston. 'Stretched exponential relaxation arising from a continuous sum of exponential decays.' *Phys. Rev. B*, **74**, 184430 (2006).

[52] H. J. Queisser and D. E. Theodorou. 'Hall-effect analysis of persistent photocurrents in n-GaAs layers.' *Phys. Rev. Lett.*, **43**, 401 (1979).

[53] D. E. Theodorou and H. J. Queisser. 'Optically enhanced mobility in a persistent photoconduction state.' *Phys. Rev. B*, **27**, 7786 (1983).

[54] D. E. Theodorou and H. J. Queisser. 'Illumination-dose dependence of persistent photoconductivity of n-GaAs epitaxial layers.' *Appl. Phys.*, **23**, 121 (1980).

[55] H. Kamerlingh Onnes. 'The resistance of pure mercury at helium temperatures.' *Commun. Phys. Lab. Univ. Leiden, b*, **120** (1911).

[56] Y. Kim, C. Hempstead, and A. Strnad. 'Critical persistent currents in hard superconductors.' *Phys. Rev. Lett.*, **9** (7), 306 (1962).

[57] W. Meissner and R. Ochsenfeld. 'Ein neuer effekt bei eintritt der supraleitfähigkeit.' *Naturwissenschaften*, **21** (44), 787 (1933).

[58] M. Tinkham. Introduction to Superconductivity (Dover Publications1996).

[59] A. Schilling, M. Cantoni, J. Guo, and H. Ott. 'Superconductivity above 130 K in the Hg–Ba–Ca–Cu–O system.' *Nature*, **363** (6424), 56 (1993).

[60] L. Gao, Y. Xue, F. Chen, Q. Xiong, R. Meng, D. Ramirez, C. Chu, J. Eggert, and H. Mao. 'Superconductivity up to 164 K in $HgBa_2Ca_{m-1}Cu_mO_{2m+2+\delta}$ (m= 1, 2, and 3) under quasihydrostatic pressures.' *Phys. Rev. B*, **50** (6), 4260 (1994).

[61] A. Drozdov, M. Eremets, I. Troyan, V. Ksenofontov, and S. Shylin. 'Conventional superconductivity at 203 kelvin at high pressures in the sulfur hydride system.' *Nature*, **525** (7567), 73 (2015).

[62] V. L. Ginzburg and L. Landau. 'On the theory of superconductivity.' In 'On Superconductivity and Superfluidity,' 113–137 (Springer2009).

[63] L. D. Landau. 'On the theory of phase transitions.' *Ukr. J. Phys.*, **11**, 19 (1937).

[64] J. F. Annett. Superconductivity, Superfluids and Condensates (Oxford University Press2004).

[65] J. van Wezel and J. van den Brink. 'Spontaneous symmetry breaking in quantum mechanics.' *Am. J. Phys.*, **75** (7), 635 (2007).

[66] J. van Wezel and J. van den Brink. 'Spontaneous symmetry breaking and decoherence in superconductors.' *Phys. Rev. B*, **77** (6), 064523 (2008).

[67] J. Bardeen, L. N. Cooper, and J. R. Schrieffer. 'Theory of superconductivity.' *Phys. Rev.*, **108** (5), 1175 (1957).

[68] L. N. Cooper. 'Bound electron pairs in a degenerate fermi gas.' *Phys. Rev.*, **104** (4), 1189 (1956).

[69] H. Fröhlich. 'Theory of the superconducting state. i. the ground state at the absolute zero of temperature.' *Phys. Rev.*, **79** (5), 845 (1950).

[70] H. Fröhlich. 'Interaction of electrons with lattice vibrations.' *Proc. R. Soc. Lond. A*, **215** (1122), 291 (1952).

[71] C. Reynolds, B. Serin, W. Wright, and L. Nesbitt. 'Superconductivity of isotopes of mercury.' *Phys. Rev.*, **78** (4), 487 (1950).

[72] E. Maxwell. 'Isotope effect in the superconductivity of mercury.' *Phys. Rev.*, **78** (4), 477 (1950).

[73] L. P. Gor'kov. 'Microscopic derivation of the ginzburg-landau equations in the theory of superconductivity.' *Sov. Phys. JETP*, **9** (6), 1364 (1959).

[74] I. Giaever. 'Electron tunneling between two superconductors.' *Phys. Rev. Lett.*, **5** (10), 464 (1960).

[75] I. Giaever. 'Energy gap in superconductors measured by electron tunneling.' *Phys. Rev. Lett.*, **5** (4), 147 (1960).

[76] T. M. Klapwijk. 'Proximity effect from an andreev perspective.' *Journal of Superconductivity*, **17**, 593 (2004).

[77] B. Pannetier and H. Courtois. 'Andreev Reflection and Proximity effect.' *J. Low Temp. Phys.*, **118**, 599 (2000).

[78] A. Andreev. 'Thermal conductivity of the intermediate state of superconductors.' *Sov. Phys. JETP*, **19**, 1228 (1964).

[79] H. Lüth. Solid Surfaces, Interfaces and Thin Films (Springer Berlin Heidelberg2010).

[80] G. E. Blonder, M. Tinkham, and T. M. Klapwijk. 'Transition from metallic to tunneling regimes in superconducting microconstrictions: Excess current, charge imbalance, and supercurrent conversion.' *Phys. Rev. B*, **25**, 4515 (1982).

[81] T. Klapwijk, G. Blonder, and M. Tinkham. 'Explanation of subharmonic energy gap structure in superconducting contacts.' *Physica B+C*, **109-110**, 1657 (1982).

[82] M. Octavio, M. Tinkham, G. E. Blonder, and T. M. Klapwijk. 'Subharmonic energy-gap structure in superconducting constrictions.' *Phys. Rev. B*, **27**, 6739 (1983).

[83] B. Josephson. 'Possible new effects in superconductive tunnelling.' *Phys. Lett.*, **1** (7), 251 (1962).

[84] B. Josephson. 'Coupled superconductors.' *Rev. Mod. Phys.*, **36**, 216 (1964).

[85] P. W. Anderson and J. M. Rowell. 'Probable observation of the josephson superconducting tunneling effect.' *Phys. Rev. Lett.*, **10** (6), 230 (1963).

[86] R. P. Feynman. Lectures on Physics (Addison-Wesley1966).

[87] S. Shapiro. 'Josephson currents in superconducting tunneling: The effect of microwaves and other observations.' *Phys. Rev. Lett.*, **11** (2), 80 (1963).

[88] J. Kohlmann, R. Behr, and T. Funck. 'Josephson voltage standards.' *Meas. Sci. Technol.*, **14** (8), 1216 (2003).

[89] J. Niemeyer and L. Grimm. 'Present status of josephson voltage metrology.' *Metrologia*, **25** (3), 135 (1988).

[90] K. K. Likharev. Dynamics of Josephson Junctions and Circuits (Gordon and Breach1986).

[91] M. A. Mohammad, M. Muhammad, S. K. Dew, and M. Stepanova. 'Fundamentals of electron beam exposure and development.' In 'Nanofabrication,' 11–41 (Springer2012).

[92] L. Ocola and A. Stein. 'Effect of cold development on improvement in electron-beam nanopatterning resolution and line roughness.' *J. Vac. Sci. Technol. B*, **24** (6), 3061 (2006).

[93] B. Cord, J. Lutkenhaus, and K. K. Berggren. 'Optimal temperature for development of poly (methylmethacrylate).' *J. Vac. Sci. Technol. B*, **25** (6), 2013 (2007).

[94] V. Bliznetsov, H. M. Lin, Y. J. Zhang, and D. Johnson. 'Deep SiO_2 etching with Al and AlN masks for mems devices.' *J. Micromechanics Microengineering*, **25** (8), 087002 (2015).

[95] K. Kolari, V. Saarela, and S. Franssila. 'Deep plasma etching of glass for fluidic devices with different mask materials.' *J. Micromechanics Microengineering*, **18** (6), 064010 (2008).

[96] D. Kan, T. Terashima, R. Kanda, A. Masuno, K. Tanaka, S. Chu, H. Kan, A. Ishizumi, Y. Kanemitsu, Y. Shimakawa, *et al.* 'Blue-light emission at room temperature from Ar^+-irradiated $SrTiO_3$ 3.' *Nat. Mater.*, **4** (11), 816 (2005).

[97] S. M. Lindsay. Introduction to Nanoscience (Oxford University Press2010).

[98] M. Cohen and R. Blunt. 'Optical properties of $SrTiO_3$ in the region of the absorption edge.' *Phys. Rev.*, **168** (3), 929 (1968).

[99] M. Capizzi and A. Frova. 'Optical gap of strontium titanate (deviation from urbach tail behavior).' *Phys. Rev. Lett.*, **25** (18), 1298 (1970).

[100] F. Pobell. Matter and Methods at Low Temperatures (Springer2007).

[101] T. Feng. 'Anomalous photoelectronic processes in $SrTiO_3$.' *Phys. Rev. B*, **25**, 627 (1982).

[102] Y. Kozuka, T. Susaki, and H. Y. Hwang. 'Vanishing hall coefficient in the extreme quantum limit in photocarrier-doped $SrTiO_3$.' *Phys. Rev. Lett.*, **101**, 096601 (2008).

[103] H. Katsu, H. Tanaka, and T. Kawai. 'Anomalous photoconductivity in $SrTiO_3$.' *Jpn. J. Appl. Phys.*, **39** (5R), 2657 (2000).

[104] T. Ishikawa, M. Kurita, H. Shimoda, Y. Sakano, S. ya Koshihara, M. Itoh, and M. Takesada. 'Isotope effect on photoconductivity in quantum paraelectric $SrTiO_3$.' *J. Phys. Soc. Jpn.*, **73** (7), 1635 (2004).

[105] N. Osawa, R. Takahashi, and M. Lippmaa. 'Hole trap state analysis in $SrTiO_3$.' *Appl. Phys. Lett.*, **110** (26), 263902 (2017).

[106] A. Stoneham, J. Gavartin, A. Shluger, A. Kimmel, D. M. Ramo, H. Rønnow, G. Aeppli, and C. Renner. 'Trapping, self-trapping and the polaron family.' *J. Phys. Condens. Matter*, **19** (25), 255208 (2007).

[107] L. Grabner. 'Photoluminescence in $SrTiO_3$.' *Phys. Rev.*, **177** (3), 1315 (1969).

[108] R. Leonelli and J. Brebner. 'Time-resolved spectroscopy of the visible emission band in strontium titanate.' *Phys. Rev. B*, **33** (12), 8649 (1986).

[109] Y. Yamada and Y. Kanemitsu. 'Photoluminescence spectra of perovskite oxide semiconductors.' *J. Lumin.*, **133**, 30 (2013).

[110] Y. Yamada, H. K. Sato, Y. Hikita, H. Y. Hwang, and Y. Kanemitsu. 'Measurement of the femtosecond optical absorption of $LaAlO_3/SrTiO_3$ heterostructures: evidence for an extremely slow electron relaxation at the interface.' *Phys. Rev. Lett.*, **111** (4), 047403 (2013).

[111] T. Hasegawa and K. Tanaka. 'Photo-induced polaron states in strontium titanate.' *J. Lumin.*, **94**, 15 (2001).

[112] T. Kohmoto, Y. Koyama, T. Moriyasu, H. Okamura, Y. Yamada, and K. Tanaka. 'Photoinduced dynamics in pure and ca-doped $SrTiO_3$ studied by transient birefringence and absorption measurements.' *J. Phys. Soc. Jpn.*, **80** (10), 104605 (2011).

[113] T. Kohmoto, D. Ikeda, X. Liang, and T. Moriyasu. 'Diffusion dynamics of the relaxed excited state in $SrTiO_3$.' *Phys. Status Solidi C*, **9** (12), 2582 (2012).

[114] T. Kohmoto, D. Ikeda, X. Liang, and T. Moriyasu. 'Direct observation of the spatial and temporal dynamics of polaron diffusion in $SrTiO_3$.' *Phys. Rev. B*, **87** (21), 214301 (2013).

[115] H. Okamura, M. Matsubara, K. Tanaka, K. Fukui, M. Terakami, H. Nakagawa, Y. Ikemoto, T. Moriwaki, H. Kimura, and T. Nanba. 'Photogenerated carriers in $SrTiO_3$ probed by mid-infrared absorption.' *J. Phys. Soc. Jpn.*, **75** (2), 023703 (2006).

[116] T. Mizokawa, N. Takaiwa, Y. Fujiwara, T. Iida, K. Takubo, J.-Y. Son, T. Ishikawa, M. Itoh, and M. Takesada. 'Photo-induced in-gap states in $SrTiO_3$ probed by photoemission spectroscopy under ultraviolet illumination.' *J. Phys. Soc. Jpn.*, **79** (4), 044703 (2010).

[117] M. C. Tarun, F. A. Selim, and M. D. McCluskey. 'Persistent photoconductivity in strontium titanate.' *Phys. Rev. Lett.*, **111** (18), 187403 (2013).

[118] M. D. McCluskey and M. C. Tarun. 'Defects and persistent conductivity in $SrTiO_3$.' *AIP Conference Proceedings*, **1583** (1), 319 (2014).

[119] V. M. Poole, J. Huso, and M. D. McCluskey. 'The role of hydrogen and oxygen in the persistent photoconductivity of strontium titanate.' *J. Appl. Phys.*, **123** (16), 161545 (2018).

[120] G. Bridoux, M. Villafuerte, J. Ferreyra, N. Bachi, C. Figueroa, and S. Heluani. 'Light-induced metal-insulator transition in $SrTiO_3$ by photoresistance spectroscopy.' *Phys. Rev. B*, **92** (15), 155202 (2015).

[121] P. C. Snijders, C. Şen, M. P. McConnell, Y.-Z. Ma, A. F. May, A. Herklotz, A. T. Wong, and T. Z. Ward. 'Dynamic defect correlations dominate activated electronic transport in $SrTiO_3$.' *Sci. Rep.*, **6**, 30141 (2016).

[122] E. Yablonovitch, D. Allara, C. Chang, T. Gmitter, and T. Bright. 'Unusually low surface-recombination velocity on silicon and germanium surfaces.' *Phys. Rev. Lett.*, **57** (2), 249 (1986).

[123] R. Moos and K. H. Hardtl. 'Defect chemistry of donor-doped and undoped strontium titanate ceramics between 1000 °C and 1400 °C.' *J. Am. Ceram. Soc.*, **80** (10), 2549 (1997).

[124] X. Hao, Z. Wang, M. Schmid, U. Diebold, and C. Franchini. 'Coexistence of trapped and free excess electrons in $SrTiO_3$.' *Phys. Rev. B*, **91** (8), 085204 (2015).

[125] A. Janotti, J. B. Varley, M. Choi, and C. G. Van de Walle. 'Vacancies and small polarons in $SrTiO_3$.' *Phys. Rev. B*, **90** (8), 085202 (2014).

[126] D. D. Cuong, B. Lee, K. M. Choi, H.-S. Ahn, S. Han, and J. Lee. 'Oxygen vacancy clustering and electron localization in oxygen-deficient $SrTiO_3$: LDA + U study.' *Phys. Rev. Lett.*, **98**, 115503 (2007).

[127] K. Szot, W. Speier, R. Carius, U. Zastrow, and W. Beyer. 'Localized metallic conductivity and self-healing during thermal reduction of $SrTiO_3$.' *Phys. Rev. Lett.*, **88**, 075508 (2002).

[128] K. A. Müller and H. Burkard. '$SrTiO_3$: An intrinsic quantum paraelectric below 4 K.' *Phys. Rev. B*, **19** (7), 3593 (1979).

[129] J. H. Ngai, Y. Segal, D. Su, Y. Zhu, F. J. Walker, S. Ismail-Beigi, K. Le Hur, and C. H. Ahn. 'Electric field tuned crossover from classical to weakly localized quantum transport in electron doped $SrTiO_3$.' *Phys. Rev. B*, **81**, 241307 (2010).

[130] M. Schultz and L. Klein. 'Relaxation of transport properties in electron-doped $SrTiO_3$.' *Appl. Phys. Lett.*, **91** (15), 151104 (2007).

[131] H. Gross, N. Bansal, Y.-S. Kim, and S. Oh. 'In situ study of emerging metallicity on ion-bombarded $SrTiO_3$ surface.' *J. Appl. Phys.*, **110** (7), 073704 (2011).

[132] V. Y. Butko, H. Wang, and D. Reagor. 'A magnetic field sensitive interfacial metallic state in a crystalline insulator.' *Nanotechnology*, **19** (30), 305401 (2008).

[133] D. W. Reagor and V. Y. Butko. 'Highly conductive nanolayers on strontium titanate produced by preferential ion-beam etching.' *Nat. Mater.*, **4** (8), 593 (2005).

[134] L. G. Quagliano and H. Nather. 'Up conversion of luminescence via deep centers in high purity GaAs and GaAlAs epitaxial layers.' *Appl. Phys. Lett.*, **45** (5), 555 (1984).

[135] S. Mochizuki, F. Fujishiro, and S. Minami. 'Photoluminescence and reversible photo-induced spectral change of $SrTiO_3$.' *J. Phys. Condens. Matter*, **17** (6), 923 (2005).

[136] M. C. Heiber, C. Baumbach, V. Dyakonov, and C. Deibel. 'Encounter-limited charge-carrier recombination in phase-separated organic semiconductor blends.' *Phys. Rev. Lett.*, **114** (13), 136602 (2015).

[137] M. C. Heiber, T.-Q. Nguyen, and C. Deibel. 'Charge carrier concentration dependence of encounter-limited bimolecular recombination in phase-separated organic semiconductor blends.' *Phys. Rev. B*, **93** (20), 205204 (2016).

[138] P. Langevin. 'Recombinaison et mobilites des ions dans les gaz.' *Ann. Chim. Phys*, **28** (433), 122 (1903).

[139] H. Y. Hwang, Y. Iwasa, M. Kawasaki, B. Keimer, N. Nagaosa, and Y. Tokura. 'Emergent phenomena at oxide interfaces.' *Nat. Mater.*, **11** (2), 103 (2012).

[140] Y.-Y. Pai, A. Tylan-Tyler, P. Irvin, and J. Levy. 'Physics of $SrTiO_3$-based heterostructures and nanostructures: a review.' *Rep. Prog. Phys.*, **81** (3), 036503 (2018).

[141] A. Ohtomo and H. Hwang. 'A high-mobility electron gas at the $LaAlO_3/SrTiO_3$ heterointerface.' *Nature*, **427** (6973), 423 (2004).

[142] L. Li, C. Richter, J. Mannhart, and R. Ashoori. 'Coexistence of magnetic order and two-dimensional superconductivity at $LaAlO_3/SrTiO_3$ interfaces.' *Nat. Phys.*, **7** (10), 762 (2011).

[143] N. Reyren, S. Thiel, A. Caviglia, L. F. Kourkoutis, G. Hammerl, C. Richter, C. Schneider, T. Kopp, A.-S. Rüetschi, D. Jaccard, *et al.* 'Superconducting interfaces between insulating oxides.' *Science*, **317** (5842), 1196 (2007).

[144] J. Mannhart, D. H. Blank, H. Hwang, A. Millis, and J.-M. Triscone. 'Two-dimensional electron gases at oxide interfaces.' *MRS bulletin*, **33** (11), 1027 (2008).

[145] K. Ueno, S. Nakamura, H. Shimotani, A. Ohtomo, N. Kimura, T. Nojima, H. Aoki, Y. Iwasa, and M. Kawasaki. 'Electric-field-induced superconductivity in an insulator.' *Nat. Mater.*, **7** (11), 855 (2008).

[146] A. Santander-Syro, O. Copie, T. Kondo, F. Fortuna, S. Pailhes, R. Weht, X. Qiu, F. Bertran, A. Nicolaou, A. Taleb-Ibrahimi, *et al.* 'Two-dimensional electron gas with universal subbands at the surface of $SrTiO_3$.' *Nature*, **469** (7329), 189 (2011).

[147] W. Meevasana, P. D. C. King, R. H. He, S.-K. Mo, M. Hashimoto, A. Tamai, P. Songsiriritthigul, F. Baumberger, and Z.-X. Shen. 'Creation and control of a two-dimensional electron liquid at the bare $SrTiO_3$ surface.' *Nat. Mater.*, **10**, 114 (2011).

[148] S. McKeown Walker, A. de la Torre, F. Y. Bruno, A. Tamai, T. K. Kim, M. Hoesch, M. Shi, M. S. Bahramy, P. D. C. King, and F. Baumberger. 'Control of a two-dimensional electron gas on $SrTiO_3$ (111) by atomic oxygen.' *Phys. Rev. Lett.*, **113**, 177601 (2014).

[149] S. M. Walker, F. Y. Bruno, Z. Wang, A. de la Torre, S. Ricco, A. Tamai, T. K. Kim, M. Hoesch, M. Shi, M. S. Bahramy, P. D. C. King, and F. Baumberger. 'Carrier density control of the $SrTiO_3$ (001) surface 2d electron gas studied by arpes.' *Adv. Mater.*, **27** (26), 3894.

[150] M. L. Knotek and P. J. Feibelman. 'Ion desorption by core-hole auger decay.' *Phys. Rev. Lett.*, **40**, 964 (1978).

[151] V. Ageev. 'Desorption induced by electronic transitions.' *Progr. Surf. Sci.*, **47** (1-2), 55 (1994).

[152] J. I. Gersten, R. Janow, and N. Tzoar. 'Theory of photodesorption.' *Phys. Rev. B*, **11** (4), 1267 (1975).

[153] S. Suwanwong, T. Eknapakul, Y. Rattanachai, C. Masingboon, S. Rattanasuporn, R. Phatthanakun, H. Nakajima, P. King, S. Hodak, and W. Meevasana. 'The dynamics of ultraviolet-induced oxygen vacancy at the surface of insulating $SrTiO_3$(001).' *Appl Surf Sci.*, **355**, 210 (2015).

[154] P. D. C. King, R. H. He, T. Eknapakul, P. Buaphet, S.-K. Mo, Y. Kaneko, S. Harashima, Y. Hikita, M. S. Bahramy, C. Bell, Z. Hussain, Y. Tokura, Z.-X. Shen, H. Y. Hwang, F. Baumberger, and W. Meevasana. 'Subband structure of a two-dimensional electron gas formed at the polar surface of the strong spin-orbit perovskite $KTaO_3$.' *Phys. Rev. Lett.*, **108**, 117602 (2012).

[155] A. Tebano, E. Fabbri, D. Pergolesi, G. Balestrino, and E. Traversa. 'Room-temperature giant persistent photoconductivity in $SrTiO_3/LaAlO_3$ heterostructures.' *Acs Nano*, **6** (2), 1278 (2012).

[156] M. Kim, C. Bell, Y. Hikita, Y. Kozuka, B. Kim, and H. Hwang. 'Photoconductivity and non-exponential relaxation at insulating $LaAlO_3/SrTiO_3$ interfaces.' *Unpublished* (2012).

[157] H.-L. Lu, Z.-M. Liao, L. Zhang, W.-T. Yuan, Y. Wang, X.-M. Ma, and D.-P. Yu. 'Reversible insulator-metal transition of $LaAlO_3/SrTiO_3$ interface for nonvolatile memory.' *Sci. Rep.*, **3**, 2870 (2013).

[158] E. Di Gennaro, U. S. di Uccio, C. Aruta, C. Cantoni, A. Gadaleta, A. R. Lupini, D. Maccariello, D. Marré, I. Pallecchi, D. Paparo, *et al.* 'Persistent photoconductivity in 2d electron gases at different oxide interfaces.' *Adv. Opt. Mater.*, **1** (11), 834 (2013).

[159] P. Irvin, Y. Ma, D. F. Bogorin, C. Cen, C. W. Bark, C. M. Folkman, C.-B. Eom, and J. Levy. 'Rewritable nanoscale oxide photodetector.' *Nat. Photonics*, **4** (12), 849 (2010).

[160] A. Rastogi, J. J. Pulikkotil, S. Auluck, Z. Hossain, and R. C. Budhani. 'Photoconducting state and its perturbation by electrostatic fields in oxide-based two-dimensional electron gas.' *Phys. Rev. B*, **86**, 075127 (2012).

[161] N. Y. Chan, M. Zhao, N. Wang, K. Au, J. Wang, L. W. H. Chan, and J. Dai. 'Palladium nanoparticle enhanced giant photoresponse at $LaAlO_3/SrTiO_3$ two-dimensional electron gas heterostructures.' *ACS nano*, **7** (10), 8673 (2013).

[162] O. Edholm and C. Blomberg. 'Stretched exponentials and barrier distributions.' *Chem. Phys.*, **252** (1-2), 221 (2000).

[163] D. Roy, Y. Frenkel, S. Davidovitch, E. Persky, N. Haham, M. Gabay, B. Kalisky, and L. Klein. 'Current-induced nonuniform enhancement of sheet resistance in Ar^+-irradiated $SrTiO_3$.' *Phys. Rev. B*, **95**, 245303 (2017).

[164] N. J. Goble, R. Akrobetu, H. Zaid, S. Sucharitakul, M.-H. Berger, A. Sehirlioglu, and X. P. Gao. 'Anisotropic electrical resistance in mesoscopic $LaAlO_3/SrTiO_3$ devices with individual domain walls.' *Sci. Rep.*, **7**, 44361 (2017).

[165] B. Kalisky, E. M. Spanton, H. Noad, J. R. Kirtley, K. C. Nowack, C. Bell, H. K. Sato, M. Hosoda, Y. Xie, Y. Hikita, *et al.* 'Locally enhanced conductivity due to the tetragonal domain structure in $LaAlO_3/SrTiO_3$ heterointerfaces.' *Nat. Mater.*, **12** (12), 1091 (2013).

[166] J. Bao, I. Shalish, Z. Su, R. Gurwitz, F. Capasso, X. Wang, and Z. Ren. 'Photoinduced oxygen release and persistent photoconductivity in ZnO nanowires.' *Nanoscale Res. Lett.*, **6** (1), 404 (2011).

[167] R. J. Collins and D. G. Thomas. 'Photoconduction and surface effects with zinc oxide crystals.' *Phys. Rev.*, **112**, 388 (1958).

[168] R. Gurwitz, R. Cohen, and I. Shalish. 'Interaction of light with the ZnO surface: Photon induced oxygen breathing, oxygen vacancies, persistent photoconductivity, and persistent photovoltage.' *J. Appl. Phys.*, **115** (3), 033701 (2014).

[169] A. N. Shultz, W. Jang, W. M. Hetherington III, D. R. Baer, L.-Q. Wang, and M. H. Engelhard. 'Comparative second harmonic generation and x-ray photoelectron spectroscopy studies of the uv creation and O_2 healing of Ti^{3+} defects on (110) rutile TiO_2 surfaces.' *Surf. Sci.*, **339** (1-2), 114 (1995).

[170] C. Soci, A. Zhang, B. Xiang, S. A. Dayeh, D. Aplin, J. Park, X. Bao, Y.-H. Lo, and D. Wang. 'ZnO nanowire UV photodetectors with high internal gain.' *Nano Lett.*, **7** (4), 1003 (2007).

[171] Y. Fujita and T. Kwan. 'Photoresponses for the oxygen adsorbed on zinc oxide powder.' *Journal of the Research institute for Catalysis Hokkaido University*, **7** (1), 24 (1959).

[172] T. L. Thompson and J. T. Yates. 'TiO_2-based photocatalysis: surface defects, oxygen and charge transfer.' *Top. Catal.*, **35** (3-4), 197 (2005).

[173] L. Kornblum, D. Fenning, J. Faucher, J. Hwang, A. Boni, M. Han, M. Morales-Acosta, Y. Zhu, E. Altman, M. Lee, *et al.* 'Solar hydrogen production using epitaxial $SrTiO_3$ on a GaAs photovoltaic.' *Energy Environ. Sci.*, **10** (1), 377 (2017).

[174] H. Tan, Z. Zhao, W.-b. Zhu, E. N. Coker, B. Li, M. Zheng, W. Yu, H. Fan, and Z. Sun. 'Oxygen vacancy enhanced photocatalytic activity of pervoskite $SrTiO_3$.' *ACS Appl. Mater. Interfaces*, **6** (21), 19184 (2014).

[175] K. Takeyasu, K. Fukada, S. Ogura, M. Matsumoto, and K. Fukutani. 'Two charged states of hydrogen on the $SrTiO_3$ (001) surface.' *J. Chem. Phys.*, **140** (8), 084703 (2014).

[176] F. Bi, D. F. Bogorin, C. Cen, C. W. Bark, J.-W. Park, C.-B. Eom, and J. Levy. 'Water-cycle mechanism for writing and erasing nanostructures at the $LaAlO_3/SrTiO_3$ interface.' *Appl. Phys. Lett.*, **97** (17), 173110 (2010).

[177] C. Cen, S. Thiel, J. Mannhart, and J. Levy. 'Oxide nanoelectronics on demand.' *Science*, **323** (5917), 1026 (2009).

[178] A. Y. Kitaev. 'Fault-tolerant quantum computation by anyons.' *Ann. Physics*, **303** (1), 2 (2003).

[179] S. Bouscher, D. Panna, and A. Hayat. 'Semiconductor–superconductor optoelectronic devices.' *J. Opt.*, **19** (10), 103003 (2017).

[180] J. Xiang, A. Vidan, M. Tinkham, R. M. Westervelt, and C. M. Lieber. 'Ge/Si nanowire mesoscopic josephson junctions.' *Nat. Nanotechnol.*, **1** (3), 208 (2006).

[181] J. Gao, J. Heida, B. Van Wees, T. Klapwijk, G. Borghs, and C. Foxon. 'Superconductors coupled with a two-dimensional electron gas in GaAs/AlGaAs and InAs/AlGaSb heterostructures.' *Surf. Sci.*, **305** (1-3), 470 (1994).

[182] A. Jellinggaard, K. Grove-Rasmussen, M. H. Madsen, and J. Nygård. 'Tuning yu-shiba-rusinov states in a quantum dot.' *Phys. Rev. B*, **94** (6), 064520 (2016).

[183] W. Chang, V. Manucharyan, T. S. Jespersen, J. Nygård, and C. M. Marcus. 'Tunneling spectroscopy of quasiparticle bound states in a spinful josephson junction.' *Phys. Rev. Lett.*, **110** (21), 217005 (2013).

[184] A. Bubis, A. Denisov, S. Piatrusha, I. Batov, V. Khrapai, J. Becker, J. Treu, D. Ruhstorfer, and G. Koblmüller. 'Proximity effect and interface transparency in Al/InAs-nanowire/Al diffusive junctions.' *Semicond. Sci. Technol.*, **32** (9), 094007 (2017).

[185] M. Kjærgaard, H. J. Suominen, M. Nowak, A. Akhmerov, J. Shabani, C. Palmstrøm, F. Nichele, and C. M. Marcus. 'Transparent semiconductor-superconductor interface and induced gap in an epitaxial heterostructure josephson junction.' *Phys. Rev. Appl.*, **7** (3), 034029 (2017).

[186] T. Akazaki, H. Takayanagi, J. Nitta, and T. Enoki. 'A josephson field effect transistor using an InAs-inserted-channel $In_{0.52}Al_{0.48}As/In_{0.53}Ga_{0.47}As$ inverted modulation-doped structure.' *Appl. Phys. Lett.*, **68** (3), 418 (1996).

[187] M. Amado, A. Fornieri, F. Carillo, G. Biasiol, L. Sorba, V. Pellegrini, and F. Giazotto. 'Electrostatic tailoring of magnetic interference in quantum point contact ballistic josephson junctions.' *Phys. Rev. B*, **87** (13), 134506 (2013).

[188] J. Tiira, E. Strambini, M. Amado, S. Roddaro, P. San-Jose, R. Aguado, F. Bergeret, D. Ercolani, L. Sorba, and F. Giazotto. 'Magnetically-driven colossal supercurrent enhancement in InAs nanowire josephson junctions.' *Nat. Commun.*, **8**, 14984 (2017).

[189] J. Alicea. 'New directions in the pursuit of majorana fermions in solid state systems.' *Rep. Prog. Phys.*, **75** (7), 076501 (2012).

[190] C. Beenakker. 'Search for majorana fermions in superconductors.' *Annu. Rev. Condens. Matter Phys.*, **4** (1), 113 (2013).

[191] J. Linder and A. Sudbø. 'Majorana fermions manifested as interface states in semiconductor hybrid structures.' *Phys. Rev. B*, **82** (8), 085314 (2010).

[192] V. Mourik, K. Zuo, S. M. Frolov, S. Plissard, E. P. Bakkers, and L. P. Kouwenhoven. 'Signatures of majorana fermions in hybrid superconductor-semiconductor nanowire devices.' *Science*, **336** (6084), 1003 (2012).

[193] M. Deng, C. Yu, G. Huang, M. Larsson, P. Caroff, and H. Xu. 'Anomalous zero-bias conductance peak in a Nb–InSb nanowire–Nb hybrid device.' *Nano Lett.*, **12** (12), 6414 (2012).

[194] M. Deng, C. Yu, G. Huang, M. Larsson, P. Caroff, and H. Xu. 'Parity independence of the zero-bias conductance peak in a nanowire based topological superconductor-quantum dot hybrid device.' *Sci. Rep.*, **4**, 7261 (2014).

[195] A. Das, Y. Ronen, Y. Most, Y. Oreg, M. Heiblum, and H. Shtrikman. 'Zero-bias peaks and splitting in an Al-InAs nanowire topological superconductor as a signature of majorana fermions.' *Nat. Phys.*, **8** (12), 887 (2012).

[196] R. M. Lutchyn, J. D. Sau, and S. Das Sarma. 'Majorana fermions and a topological phase transition in semiconductor-superconductor heterostructures.' *Phys. Rev. Lett.*, **105**, 077001 (2010).

[197] L. P. Rokhinson, X. Liu, and J. K. Furdyna. 'The fractional ac josephson effect in a semiconductor–superconductor nanowire as a signature of majorana particles.' *Nat. Phys.*, **8** (11), 795 (2012).

[198] J. R. Williams and D. Goldhaber-Gordon. 'Majorana fermions: doubling down on majorana.' *Nat. Phys.*, **8** (11), 778 (2012).

[199] T. Klapwijk. 'Mesoscopic superconductor-semiconductor heterostructures.' *Physica B*, **197** (1-4), 481 (1994).

[200] C. Ojeda-Aristizabal, M. Ferrier, S. Guéron, and H. Bouchiat. 'Tuning the proximity effect in a superconductor-graphene-superconductor junction.' *Phys. Rev. B*, **79** (16), 165436 (2009).

[201] I. Giaever. 'Photosensitive tunneling and superconductivity.' *Phys. Rev. Lett.*, **20** (23), 1286 (1968).

[202] F. Andreozzi, A. Barone, M. Russo, G. Paterno, and R. Vaglio. 'Measurements of the dc josephson current in light-sensitive junctions.' *Phys. Rev. B*, **18** (11), 6035 (1978).

[203] S. Takaoka, Y. Nakao, T. Kousai, K. Haruta, K. Oto, K. Murase, and K. Gamo. 'Investigation of photoresponse in photoconducting semiconductor-superconductor microstructure.' *Jpn. J. Appl. Phys.*, **34** (10R), 5585 (1995).

[204] T. Schäpers, R. Müller, A. Kaluza, H. Hardtdegen, and H. Lüth. 'Adjustment of the critical current in a Nb–$In_xGa_{1-x}As$/InP josephson contact by light exposure.' *Appl. Phys. Lett.*, **75** (3), 391 (1999).

[205] T. Akazaki, H. Hashiba, M. Yamaguchi, K. aa, S. Nomura, and H. Takayanagi. 'Interplay between negative photoconductivity and enhanced andreev reflection in InGaAs-based s-sm-s junctions when exposed to infrared light.' *J. Phys. Conf. Ser.*, **150** (5), 052004 (2009).

[206] K. Tsumura, S. Nomura, T. Akazaki, and H. Takayanagi. 'Optical imaging of the transport properties of s-sm-s junctions.' *J. Phys. Conf. Ser.*, **150** (5), 052273 (2009).

[207] K. Tsumura, S. Nomura, T. Akazaki, and H. Takayanagi. 'Position dependent optical effect on the transport properties of s-sm-s junctions.' *Physics Procedia*, **3** (2), 1177 (2010).

[208] K. Tsumura, N. Furukawa, H. Ito, E. Watanabe, D. Tsuya, and H. Takayanagi. 'Non-equilibrium photoexcited carrier effects in a graphene-based josephson junction.' *Appl. Phys. Lett.*, **108** (3), 033109 (2016).

[209] S. Eley, S. Gopalakrishnan, P. M. Goldbart, and N. Mason. 'Approaching zero-temperature metallic states in mesoscopic superconductor–normal–superconductor arrays.' *Nat. Phys.*, **8** (1), 59 (2012).

[210] J. F. Annett. '2d electron systems: Metals in flatland.' *Nat. Phys.*, **8** (1), 8 (2012).

[211] S. Eley, S. Gopalakrishnan, P. M. Goldbart, and N. Mason. 'Dependence of global superconductivity on inter-island coupling in arrays of long sns junctions.' *J. Phys. Condens. Matter*, **25** (44), 445701 (2013).

[212] D. W. Abraham, C. Lobb, M. Tinkham, and T. Klapwijk. 'Resistive transition in two-dimensional arrays of superconducting weak links.' *Phys. Rev. B*, **26** (9), 5268 (1982).

[213] C. Lobb, D. W. Abraham, and M. Tinkham. 'Theoretical interpretation of resistive transition data from arrays of superconducting weak links.' *Phys. Rev. B*, **27** (1), 150 (1983).

[214] P. Gallagher, M. Lee, J. R. Williams, and D. Goldhaber-Gordon. 'Gate-tunable superconducting weak link and quantum point contact spectroscopy on a strontium titanate surface.' *Nat. Phys.*, **10** (10), 748 (2014).

[215] N. Saowadee, K. Agersted, and J. R. Bowen. 'Effects of focused ion beam milling on electron backscatter diffraction patterns in strontium titanate and stabilized zirconia.' *J. Microsc.*, **246** (3), 279 (2012).

[216] N. Saowadee, K. Agersted, H. Ubhi, and J. R. Bowen. 'Ion beam polishing for three-dimensional electron backscattered diffraction.' *J. Microsc.*, **249** (1), 36 (2013).

[217] F. Giazotto, K. Grove-Rasmussen, R. Fazio, F. Beltram, E. Linfield, and D. Ritchie. 'Josephson current in Nb/InAs/Nb highly transmissive ballistic junctions.' *Journal of superconductivity*, **17** (2), 317 (2004).

[218] A. Chrestin, T. Matsuyama, and U. Merkt. 'Evidence for a proximity-induced energy gap in Nb/InAs/Nb junctions.' *Phys. Rev. B*, **55** (13), 8457 (1997).

[219] M. Kjaergaard, H. J. Suominen, M. P. Nowak, A. R. Akhmerov, J. Shabani, C. J. Palmstrøm, F. Nichele, and C. M. Marcus. 'Transparent semiconductor-superconductor interface and induced gap in an epitaxial heterostructure josephson junction.' *Phys. Rev. Applied*, **7**, 034029 (2017).

[220] W. Yu, Y. Jiang, C. Huan, X. Chen, Z. Jiang, S. D. Hawkins, J. F. Klem, and W. Pan. 'Superconducting proximity effect in inverted InAs/GaSb quantum well structures with ta electrodes.' *Appl. Phys. Lett.*, **105** (19), 192107 (2014).

[221] P. Krogstrup, N. Ziino, W. Chang, S. Albrecht, M. Madsen, E. Johnson, J. Nygård, C. Marcus, and T. Jespersen. 'Epitaxy of semiconductor–superconductor nanowires.' *Nat. Mater.*, **14** (4), 400 (2015).

[222] J. Shabani, M. Kjaergaard, H. Suominen, Y. Kim, F. Nichele, K. Pakrouski, T. Stankevic, R. M. Lutchyn, P. Krogstrup, R. Feidenhans, *et al.* 'Two-dimensional epitaxial superconductor-semiconductor heterostructures: A platform for topological superconducting networks.' *Phys. Rev. B*, **93** (15), 155402 (2016).

[223] K. Gharavi, G. W. Holloway, R. R. LaPierre, and J. Baugh. 'Nb/InAs nanowire proximity junctions from josephson to quantum dot regimes.' *Nanotechnology*, **28** (8), 085202 (2017).

[224] E. Pallecchi, M. Gaaß, D. Ryndyk, and C. Strunk. 'Carbon nanotube josephson junctions with nb contacts.' *Appl. Phys. Lett.*, **93** (7), 072501 (2008).

[225] T. C. Rödel, F. Fortuna, S. Sengupta, E. Frantzeskakis, P. L. Fèvre, F. Bertran, B. Mercey, S. Matzen, G. Agnus, T. Maroutian, *et al.* 'Universal fabrication of 2d electron systems in functional oxides.' *Adv. Mater.*, **28** (10), 1976 (2016).

[226] J. Delahaye and T. Grenet. 'Metallicity of the $SrTiO_3$ surface induced by room temperature evaporation of alumina.' *J. Phys. D*, **45** (31), 315301 (2012).

[227] A. B. Posadas, K. J. Kormondy, W. Guo, P. Ponath, J. Geler-Kremer, T. Hadamek, and A. A. Demkov. 'Scavenging of oxygen from $SrTiO_3$ during oxide thin film deposition and the formation of interfacial 2degs.' *J. Appl. Phys.*, **121** (10), 105302 (2017).

[228] X. Lin, C. W. Rischau, L. Buchauer, A. Jaoui, B. Fauqué, and K. Behnia. 'Metallicity without quasi-particles in room-temperature strontium titanate.' *npj Quantum Mat.*, **2** (1), 41 (2017).

[229] T. Rodel. 'Two-dimensional electron systems in functional oxides studied by photoemission spectroscopy.' Ph.D. thesis, Université Paris-Saclay (2016).

[230] Z. Lu, J. Yi-Rong, L. Jie, D. Hui, and Z. Dong-Ning. 'Fabrication and properties of the meander nanowires based on ultra-thin Nb films.' *Chin. Phys. B*, **23** (8), 087402 (2014).